SYNAPTIC TRANSMISSION AND ELECTRICAL RESONANCE IN EARLY AUDITORY PROCESSING

By
Lucille A. Moore

A DISSERTATION

Presented to the Neuroscience Graduate Program, the Vollum Institute, and
Oregon Hearing Research Center
Oregon Health and Science University
School of Medicine

Doctor of Philosophy

January 2019

TABLE OF CONTENTS

ACKNOWLEDGEMENTS

This work is a culmination of years of work and would not have been possible without the support of mentors, family, and friends. I thank Dr. Larry Trussel, my mentor, for supporting, training, and guiding me in all aspects of academia, including rigorous experimentation, effective writing and presentation, and more. I also thank my committee members for supporting my research and providing critical insight throughout my graduate career. My committee members include Drs. Gary L. Westbrook, Christine V. Portfors, and John T. Williams.

I thank my current and previous lab members for providing a positive and supportive environment, helping to train me in various techniques, and providing feedback on my research. Former lab members include Drs. Carolina Borges-Merjane, Hsin-Wei Lu, and Daniel D. Yaeger. I also thank former lab member and collaborator Dr. Pierre F. Apostolides. My current lab members include Gabriel E. Romero, Tavita R. Garrett, Douglas M. Zeppenfeld and Drs. Timothy S. Balmer, and Zheng-Quan Tang.

Finally, I thank my family and friends for their support and encouragement. I thank the Alliance for Visible Diversity in Science (AVDS) for providing a mechanism for me to engage in vital social equity issues in science during my graduate career. I also thank my ARCS donors Julie Branford, Dianne Rodway, and John Becker for their support.

ABSTRACT

This dissertation investigates two unique phenomena, neurotransmitter co-release and neural oscillations, in early auditory regions where they have not been observed before. Co-release and oscillations are common processes in other brain regions, where they are thought to expand the computational capacity of local circuits. Co-release is the release of two neurotransmitter types packaged into the same presynaptic vesicles within a neuron and oscillations are rhythmic electrical fluctuations observed in single neurons, brain regions, and even spanning brain regions (Vaaga et al., 2014). How they contribute to early auditory processing, however, is not understood. We investigated co-release of two inhibitory neurotransmitters in the inferior colliculus, the midbrain hub for auditory processing. We also established the presence of slow oscillations in the principal neurons of the dorsal cochlear nucleus (DCN), a key brainstem nucleus that integrates auditory input from the ear with multisensory information. Both lines of research utilized patch-clamp electrophysiological recordings from *in vitro* slices of mouse brainstem and midbrain. This dissertation reveals new mechanisms for how auditory information is processed by local brainstem and midbrain circuits.

In Chapter 1, I explored the co-release of two inhibitory neurotransmitters, GABA and glycine, in the auditory midbrain of mouse. Co-release is common throughout the auditory brainstem, but our work was the first evidence for its existence in the inferior colliculus of the auditory midbrain. The inferior colliculus is one of the least well-understood areas of the brain in terms of its anatomical and functional organization. In order to better understand this structure, I characterized co-release of GABA and

glycine from ascending afferents and probed for its sfunctional roles in the IC. Surprisingly, GABAergic and glycinergic postsynaptic currents were similar in time course, short-term synaptic plasticity dynamics, and metabotropic regulation. These results suggest that co-release may allow for redundancy and homeostatic stability in cases where one transmitter system is compromised.

In Chapter 2, I investigated slow spontaneous oscillations in the membrane potential of DCN output neurons, or fusiform cells. Fusiform cells receive both auditory and multisensory input and make direct projections to the midbrain. The entire DCN circuit is built around the principal neuron's ability to encode sound and integrate multisensory information, thus making it vital to understand the intrinsic properties that mediate these functions. The oscillations are 1-2 Hz, rely on HCN and persistent Na^+ conductances, and are similar in frequency to the intrinsic resonant frequency of the fusiform cells. The oscillations are also regulated by external Ca^{2+} concentration, which impacts Na^+ channel activation. Finally, the electrical coupling between fusiform cells enables oscillation synchrony. Our results indicate that oscillatory activity, which has previously received the most attention in thalamocortical circuits, may play an important computational role at the first stage of auditory processing.

INTRODUCTION

The ability of the brain to extract meaningful information from the auditory environment relies on neural circuits specialized to process sensory information. Each sensory system has evolved to transform fundamentally different sensory information into a neural representation of the world. The auditory system in particular has evolved to transmit high-frequency signals with remarkable fidelity. Each region of the auditory brainstem encodes some aspect of sound relating to frequency, amplitude, and/or location of sound in space.

This dissertation was directed at two physiological phenomena, neurotransmitter co-release and oscillatory activity. Although previously thought to be reserved to very specific brain regions, co-release and oscillations are gaining recognition as more widespread and computationally important processes. Co-release is the release of two neurotransmitter types from overlapping vesicular pools within a single neuron (Vaaga et al., 2014). For a long time it was thought that neurons only released one type of neurotransmitter, known as the “one neuron, one neurotransmitter,” or Dale’s, principle (Tritsch et al., 2016). However, recent research has shown that co-release of more than one neurotransmitter from the same neuron, particularly of the neurotransmitter GABA with other types, occurs in several brain regions (Vaaga et al., 2014). Co-release is an interesting phenomenon as it introduces another degree of variance, thus expanding the computational power of single synapses. In our study, we looked at the co-release of inhibitory neurotransmitters GABA and glycine. The co-release of these fast-acting inhibitory neurotransmitters is particularly paradoxical as it is not immediately obvious why these neurotransmitters would have differential functions. Furthermore, though

GABA/glycine co-release is common in auditory brainstem regions, it was previously unknown that co-release extended to the midbrain.

The second phenomenon we studied was neural oscillations. Oscillations are rhythmic electrical fluctuations observed in single neurons, brain regions, and spanning brain regions. They have received the most attention in cortical regions, where different frequencies in the surface electroencephalogram are associated with different states of arousal, stages of sleep, and sensory perception (Buzsáki 2006). However, we observed oscillations in brain slices in the dorsal cochlear nucleus (DCN), which receives direct input from the auditory nerve and is thus one of the first brain regions to process auditory information. The oscillations were present in fusiform cells, the output neuron of DCN. In Chapter 2, we examined the biophysical origins of these oscillations and how they may impact the circuit via oscillation synchrony between electrically coupled neurons. The presence of oscillations in the first stage of auditory processing suggests that oscillatory activity and resonance may be a common mechanism in the brain, at both higher and lower levels, whereby neuronal populations within a given region can work cohesively.

1. Co-release of inhibitory neurotransmitters in the inferior colliculus

The inferior colliculus

The inferior colliculus (IC) is the major subcortical integrator of the auditory system. Its central nucleus (the ICC) is a near-obligatory relay for ascending auditory information from the brainstem (Malmierca et al. 2002, Cant 2005, Schofield 2005). Ascending inputs impinge upon diverse cell types within the local circuitry, producing fascinating emergent properties such as convergence of auditory signals from both

ears, spatial localization, and vocalization selectivity (Yin & May 2005, Holmstrom et al. 2010). The IC also receives multisensory information, which is integrated with auditory streams to subserve sound-induced flight behavior and the startle response (Xiong et al., 2015, 2017).

To support the density of inputs, the ICC has a complex internal circuitry composed of diverse cell types. Interestingly, the cellular identities and connective structure remain largely unknown. Surrounding the ICC, the lateral nucleus (LN) and dorsal cortex (DC) primarily receive multisensory (Aitkin et al., 1978) and descending (Druga et al., 1997; Winer et al., 1998) cortical input, respectively. These regions have different functions and microcircuit structure from the central nucleus. Ascending inputs to the ICC are organized into frequency-specific laminae, creating a tonotopic map with high frequency processing in the ventromedial pole and low frequency processing in the dorsolateral pole (Stiebler and Ehret, 1985). Laminae are thought to contain basic functional units of cells that interconnect to support differential input (Ito and Oliver, 2012). Within laminae, there is a heterogeneous population of excitatory and inhibitory cells, the biophysical diversity of which presumably underlies the coding power and efficiency of the ICC (Shamir and Sompolinsky, 2006; Holmstrom et al., 2010; Padmanabhan and Urban, 2010).

The convergence of temporal, spectral and spatial information in the IC makes it a unique integrative hub. Auditory information is processed in parallel in upstream brainstem regions and coalesce in the IC, although to what degree the information is combined or processed separately is unknown (Joris et al., 2004). Major excitatory inputs to the IC include the cochlear nucleus (CN), medial superior olive (MSO), and

contralateral lateral superior olive (LSO). Major inhibitory sources include the dorsal and ventral nuclei of the lateral lemniscus (NLL) and ipsilateral LSO (Figure 1).

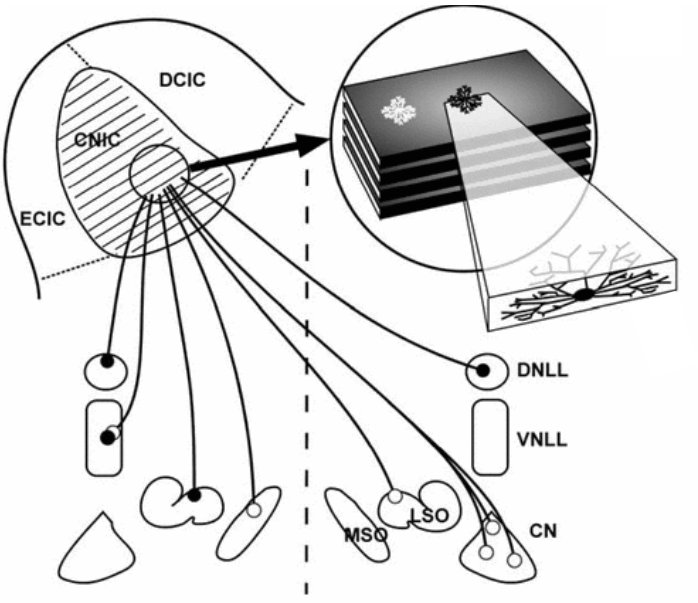

Figure 1. Figure reprinted with permission from Brunso-Bechtold & Henkel (2005) displaying sources of ascending input to ICC. Sources of excitatory and inhibitory input are displayed in white and black, respectively. *D/VNLL:* dorsal/ventral nucleus of the lateral lemniscus, *M/LSO*: medial/lateral superior olive, *CN*: cochlear nuclei.

Studies of termination patterns in ICC as well as response properties have defined different "synaptic domains." Loftus et al. (2010) combined single unit recordings in cat with iontophoretic injections of fluorogold. They identified monaural neurons that received input from CN and VNLL only; ITD- and low frequency-sensitive neurons (<500 Hz) with input from ipsilateral MSO and LSO; and ITD- and high frequency-sensitive neurons with input from contralateral LSO and DNLL. In gerbils, afferent termination patterns in lateral and rostral areas received inputs primarily from CN, LSO, MSO and NLL, whereas medial and caudal areas receive inputs primarily from CN and NLL, but not MSO and LSO (Cant and Benson, 2006). It therefore appears that the ICC has another dimension of organization beyond tonotopy that relies on the

unique combination of afferent input to each region. It is therefore of vital importance to understand more about the nature of these inputs.

Ascending inhibitory input to IC

The auditory system is unique in the brain in that it contains many long-range inhibitory afferents, including the ICC (Figure 2). Sources of ascending inhibition to the ICC include ipsi- and contralateral DNLL, ipsilateral VNLL, and ipsilateral LSO (Saint Marie and Baker, 1990). The contralateral lobe of the IC is also a major source of inhibitory input, with 50% of the contralaterally-projecting IC neurons staining positively for GABA (González-Hernández et al., 1996; Zhang et al., 1998). Sources of glycinergic inhibition to ICC include the VNLL and LSO to a lesser extent (Saint Marie and Baker, 1990).

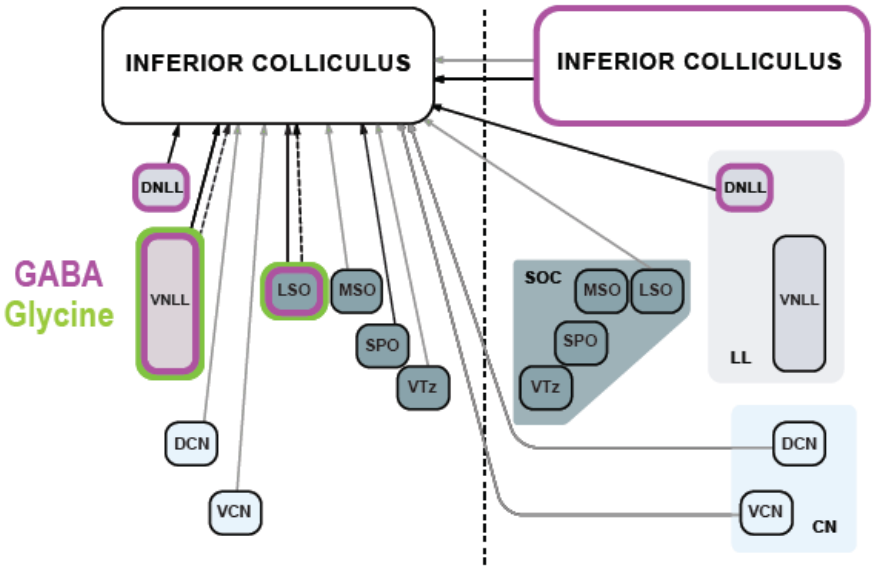

Figure 2. Ascending inputs to the ICC with sources of GABAergic input highlighted in purple and glycinergic input highlighted in green (adapted from Ayala et al. 2015).

Interestingly, histological evidence from multiple adult species shows that cells within VNLL and LSO label for both glycine and GABA. For example, Saint Marie et al. (1997) showed that ~80% of neurons in VNLL of cat are glycinergic and half of these

are also immunoreactive for GABA. Riquelme et al. (2001) used *in situ* hybridization to show that the majority of neurons in rat VNLL co-localize GABA and glycine. Finally, Tanaka & Ezure (2004) showed that the ratio of double-labeled neurons in VNLL and LSO is particularly high compared to other brainstem regions. The histological evidence therefore collectively suggests that glycinergic afferents terminating in the ICC also release GABA. However, this question has never been probed directly in the ICC.

VNLL and LSO

The VNLL is thought to be the single largest source of inhibition to the IC because it consistently shows the highest counts of labeled cells after injection of retrograde tracers into the IC across species (Cant 2005). VNLL receives the majority of its input from contralateral VCN (including T-stellate, bushy, and octopus cells) and a smaller input from ipsilateral VCN and MNTB (Adams, 1997; Schofield and Cant, 1997). Cells of the VNLL show combination sensitivity and tuning to amplitude modulation and relay auditory information with exceptional temporal precision, particularly at the onset of sound (Portfors and Wenstrup, 2001; Recio-Spinoso and Joris, 2014). This major inhibitory projection to ICC is therefore thought to provide precisely timed feed-forward inhibition. Furthermore, as a monaural structure, the VNLL is thought to be more generally important for recognition of temporal patterns and meaning in sound, as opposed to areas that function primarily in sound location (Covey and Casseday, 1991; Oertel & Wickesberg 2002).

In the LSO, nearly half of the neurons are glycinergic and project to the ipsilateral IC (Saint Marie et al., 1989a; Glendenning et al., 1992; Ostapoff et al., 1997). Excitatory LSO projections terminate in contralateral IC. The LSO receives glutamatergic input

from ipsilateral VCN and glycinergic input from contralateral MNTB (Glendenning et al., 1991). As such, it is known to encode sound localization based on the comparison of sound intensity between the two ears. It is speculated that the inhibitory projections to IC play a role in binaural inhibition in parallel with pure GABAergic projections from contralateral DNLL (Kelly & Caspary 2005).

Role of GABA versus glycine in IC

Generally, *in vivo* studies show that GABAergic inhibition in isolation shapes frequency tuning curves, tuning to amplitude modulation, binaural inhibition, duration tuning, and vocalization selectivity (Watanabe and Simada, 1973; Faingold et al., 1989; Xie et al., 2005). The role of glycinergic inhibition in isolation is generally similar, but the frequency and strength of effects are more variable (Faingold et al., 1989; Vater et al., 1992; Klug et al., 1995; LeBeau et al., 2001; Wenstrup et al., 2012).

Though GABAergic and glycinergic inputs may generally play similar functional roles in the IC, there is some evidence for unique functions. Some studies have claimed that GABA may uniquely subserve binaural inhibition: severing the commissure of Probst or pharmacological block of DNLL, a major sources of pure GABAergic input, blocks binaural inhibition in rat (Kelly and Caspary 2005). Faingold et al. (1989) similarly observed block of binaural inhibition with iontophoresis of GABA receptor antagonist bicuculline, but rarely with the glycine receptor antagonist strychnine. One unique role for glycinergic input may be combination sensitive facilitation, which is thought to be an emergent property of the ICC (see review Wenstrup et al., 2012). Combination sensitivity describes the phenomenon where the response of a neuron to a combination

of frequencies is greater than the sum of responses to each frequency presented in isolation.

Co-release

Co-release describes the release of two neurotransmitter types packaged into the same presynaptic vesicles. Co-release is distinct from co-transmission, which is the release of multiple transmitter types from non-overlapping vesicular pools. Co-transmission may result from spatial segregation, where the vesicular pools that carry each neurotransmitter type are located at separate presynaptic terminals. It may also result from vesicular segregation, where each vesicle within a terminal expresses only one vesicular transporter type, causing each vesicle to carry either one or the other neurotransmitter, but not both (Vaaga et al., 2014).

Co-release is particularly common with GABAergic neurons (Tritsch et al., 2016). GABA is co-released with a variety of neurotransmitters, including glutamate, acetylcholine (e.g. Starburst amacrine cells onto direction-selectived ganglion cells in retina and globus pallidus to cortical interneurons), histamine, and dopamine (e.g. VTA and SNc projections to spiny projection neurons of the striatum) (Lee et al., 2010, Stensrud et al. 2014). Unlike other co-released neurotransmitters, GABA and glycine actually share the same vesicular transporter, the vesicular GABA transporter (VGAT), so neurotransmitter loading depends on the concentration of the respective neurotransmitters in the terminal (Wojcik et al., 2006; Apostolides and Trussell, 2013a).

Along with spinal cord and cerebellum, co-release of GABA and glycine is well documented in the auditory brainstem. At some synapses, such as from MNTB to LSO, a developmental switch from GABAergic to glycinergic signaling is driven by a shift in

transmitter type release as opposed to changes in postsynaptic receptor expression (Nabekura et al., 2004; Muller et al., 2006). However, even in adult, synaptic currents mediated by both neurotransmitters can be recorded in LSO, MNTB, and DCN (Nabekura et al., 2004; Rubio, 2004; Awatramani et al., 2005; Roberts et al., 2008).

The function of GABA/glycine co-release in the auditory brainstem is not well understood, but seems to be specific to the synapse at which it occurs. For instance, in MNTB, GABA acts as a partial agonist for GlyRs, resulting in very fast synaptic decay times of 1-2 ms (Lu et al., 2008). These decay kinetics are faster than those reported at other glycinergic synapses and is likely uniquely tuned to the needs of MNTB (Chéry and De Koninck, 1999a; Singer and Berger, 1999; Dugue et al., 2005). GABAergic IPSCs are typically much slower than glycinergic IPSCs, leading many to suggest that they may subserve tonic versus phasic inhibition, respectively (Jonas et al., 1998; Dumoulin et al., 2001; Kuo et al., 2009). Co-release in the auditory brainstem may also serve as compensation during periods of high activity. In the avian auditory system, stimulation at high rates evokes a slowly emerging glycinergic component (Fischl et al., 2014). Further, inhibition onto spherical bushy cells in gerbil AVCN shifts from predominantly glycinergic to GABAergic in an activity-dependent manner such that the IPSC decay is slowed with increased input rates (Nerlich et al., 2014).

Summary

Chapter 1 investigates the nature of co-release from ascending inhibitory fibers to the ICC. We used miniature postsynaptic current analysis to first establish the existence of co-release. Miniature IPSCs, or “minis,” are the result of the presynaptic release of a single synaptic vesicle (Fatt and Katz, 1952; del Castillo and Katz, 1954).

Using zolpidem and pentobarbital to slow the GABAergic component, we were able to kinetically distinguish between glycinergic and GABAergic components contained within single minis, thus establishing for the first time the presence of GABA/glycine co-release in the ICC. We used optogenetics and intracranial injections to test the impacts of GABA/glycine co-release on local ICC circuitry. A number of theories have been put forward to explain the possible functional implications of glycine/GABA co-release in auditory brainstem regions. We rigorously tested these theories using genetic tools to precisely stimulate a genetically defined cell type. Our results indicate that co-release in the auditory midbrain may be a redundant system that allows for homeostasis in situations where one neurotransmitter is compromised. In summary, our work provides new insights both to auditory neuroscience and the expanding studies of co-release in the brain.

2. Electrical resonance and slow oscillations in cochlear nucleus

Dorsal cochlear nucleus

The dorsal cochlear nucleus (DCN) is one of the first brainstem regions to receive auditory input. It is organized in a laminar fashion oriented parallel to the surface of the nucleus, with three layers known as the deep, fusiform cell, and molecular layers (Figure 3) (Oertel and Young, 2004). Auditory nerve fibers carrying information about different sound frequencies project to the DCN in a tonotopic fashion, forming a gradient of tonotopic domains in the DCN where higher frequencies are encoded dorsally and lower frequencies are encoded ventrally (Fettiplace and Fuchs, 1999; Muniak et al., 2013).

In terms of cytoarchitecture, auditory nerve fibers synapse onto the basal dendrites of the output neurons of the DCN, called fusiform cells, which send direct projections to the inferior colliculus. Auditory nerve fibers also contact inhibitory vertical cells, which provide feed-forward inhibition to fusiform cells. Along with encoding sound frequency, fusiform cells receive multisensory information via parallel fiber input to their apical dendrites. Parallel fibers terminate on inhibitory cartwheel and superficial stellate cells, which both provide feed-forward inhibition to fusiform cells. Parallel fibers are the axons of granule cells in the deep layer, which receive multisensory inputs via mossy fiber inputs. Inhibitory Golgi cells and excitatory unipolar brush cells are deep layer interneurons that also receive mossy fiber input and provide feed-forward input to granule cells. Of note, fusiform cells are electrically connected with each other as well as superficial stellate cells, which is a highly unique arrangement for excitatory projection neurons and their companion interneurons (Apostolides and Trussell, 2013b, 2014). The multisensory integration in fusiform cells is thought to enable the DCN to encode location of sound in the vertical plane and cancel self-generated noise and vocalizations (May, 2000; Oertel and Young, 2004; Shore, 2005; Singla et al., 2017).

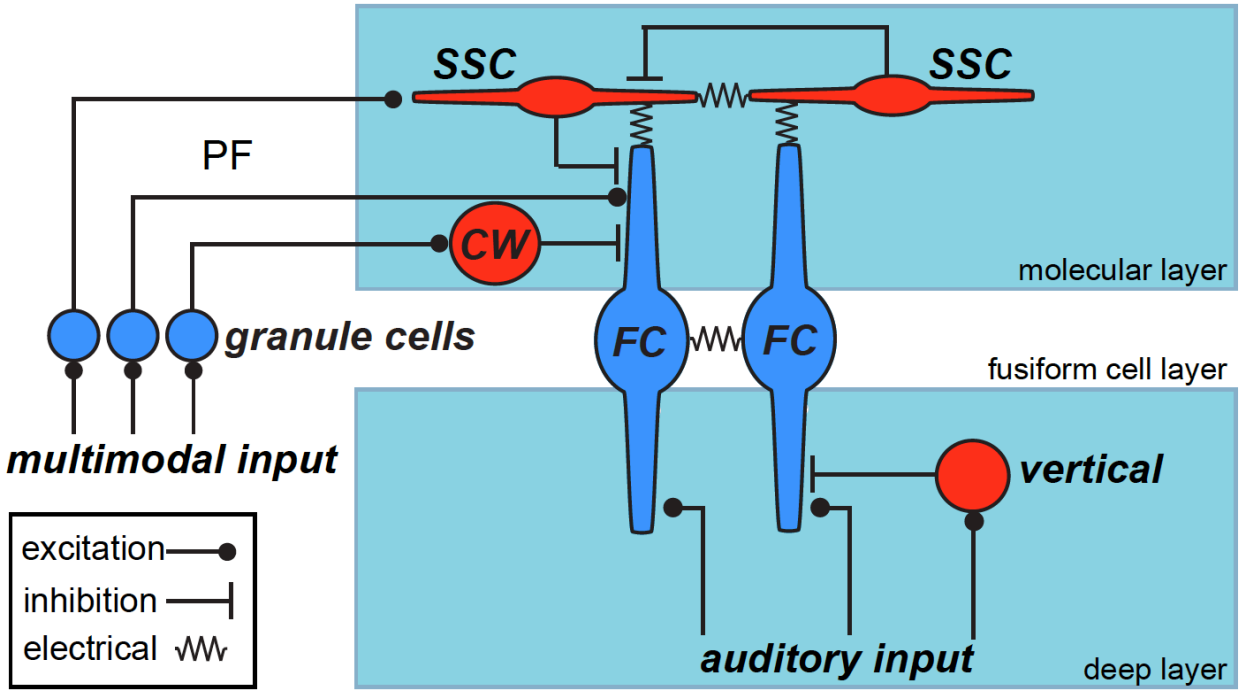

Figure 3. Simplified local circuit diagram of DCN. Fusiform cells receive auditory nerve fiber input onto their basal dendrites in the deep layer and multisensory input via parallel fibers onto their apical dendrites in the molecular layer. Fusiform cells also receive feed-forward inhibition from vertical and cartwheel cells, which are contacted by auditory and parallel fibers (PF) respectively. Parallel fibers originate from granule cells in the deep layer of DCN, which receive multimodal input from a variety of multisensory regions.

Resonance

Resonance is a biophysical property of neurons that describes the frequency-dependence of their input-output curves. Resonance is created by active and passive properties that filter low and high frequency voltage fluctuations, creating a bandpass hump in the impedance curve for a neuron (Hutcheon & Yarom 2000). The passive membrane properties of neurons typically filter out high-frequency voltage fluctuations while low-frequency fluctuations are filtered by the slow kinetics of currents such as Ih, INap, and It. Impedance can be thought of as the frequency-dependent input resistance

of a neuron. Impedance is maximal at the resonant frequency of a neuron, resulting in the maximal voltage response to current injected at that frequency.

The same intrinsic electrical properties that create resonance can also result in the occurrence of spontaneous subthreshold membrane potential oscillations, the frequency of which is determined by passive and active membrane properties. Thus, resonance and neural oscillations are two sides of the same coin and highly interrelated. Indeed, intrinsic resonance sets the frequency of oscillating networks such as in the hippocampus and in the thalamocortical network (Mccormick and Pape, 1990; Chen et al., 2016; Neske, 2016).

Neural oscillations

Neural oscillations were first studied in 1924 by Hans Berger in the form of electroencephalographic (EEG) recordings, which revealed that different frequency bands were associated with sensory perception, arousal, and sleep (Melloni et al., 2007; Zijlmans et al., 2009; Wang, 2010). EEG measurements are made at the scalp and therefore reflect the summed electrical activity of neuronal populations near the cortical surface. However, oscillatory activity also occurs regionally throughout the brain. As such, oscillations can be observed in local field potentials and individual neuronal membrane potential both *in vivo* and *in vitro* (Sanchez-Vives and McCormick, 2000; Lagier et al., 2004; Okun et al., 2010; Neske, 2016). Indeed, the first spontaneous membrane oscillations were observed in the strongly oscillatory inferior olivary neurons in 1986 (Llinás and Yarom, 1986). These more regionalized oscillations are generally thought to facilitate synchrony and coherent neural activity, allowing for functional outputs unique to different brain regions (Buzsáki 2006). Gamma (30-100 Hz) and theta

(4-7 Hz) oscillations are compromised in a number of neurological and psychiatric disorders, including epilepsy and schizophrenia (Dugladze et al., 2007; Bettus et al., 2008; Gröticke et al., 2008; Gonzalez-Burgos et al., 2015; Lega et al., 2015; Mathalon and Sohal, 2015; Shuman et al., 2017).

Slow oscillations of 1-5 Hz in cortex and thalamus are associated with deep sleep, quiet wakefulness, and stimulus familiarity (Poulet and Petersen, 2008; Gentet et al., 2010; Neske, 2016; Kissinger et al., 2018). In more recent years, a number of labs have studied slow oscillations using whole-cell recordings in cortex from awake and behaving animals. Quiet wakefulness, where the animal is at rest, is associated with slow membrane potential oscillations in a number of cortical areas. In barrel cortex of mice, both excitatory and inhibitory neurons display slow oscillations that are reduced with sensory input from whisking (Crochet and Petersen, 2006; Gentet et al., 2010). These oscillations are also highly correlated between nearby neurons, resulting in correlated LFPs and EEGs as well (Poulet and Petersen, 2008). Similar observations have been made in V1 of cat, where neurons with the same as well as different orientation preferences show decreased slow oscillation synchrony in response to visual stimulation while increasing or maintaining high frequency (20-80 Hz) synchrony (Yu and Ferster, 2010).

As with other cortical areas, slow oscillations are present in auditory cortex of possible functional significance. Lakatos et al. (2005) showed that slow oscillations in primary auditory cortex of primate may modulate circuit excitability because the phase of low-frequency oscillations modulates the amplitude of sound-evoked oscillations of higher frequency. This group also found that somatosensory input to A1 resets the

phase of ongoing oscillations, causing a period of heightened excitability that amplified auditory input. They suggested that this type of multisensory integration could allow animals to hear better (Lakatos et al., 2007). A recent study in humans also showed that slow oscillations entrain to subthreshold rhythmic sounds to enable faster detection, therefore serving a predictive function (ten Oever et al., 2017).

Despite the mounting evidence for the computational significance of oscillatory activity in cortex, the topic has received much less attention in lower brainstem areas other than the so-called chopper neurons that are thought to be important for processing pitch (Bahmer and Gupta, 2018). Chopper neurons respond to both tones and current injection with regularly spaced action potentials. Slow oscillations have been observed subcortical regions, where they have been proposed to coordinate output amongst inputs occurring at a broad range of times and gate the timing of neural output (Schoppa and Westbrook, 2001; Lefler et al., 2013). In DCN, oscillations have been observed in the form of modulated spike frequency. In cat, the oscillation frequency is close to the best envelope frequency of the neuron, ranging for example from 100-200 Hz (Kim et al., 1990). In gerbil, the majority of units exhibit intrinsic oscillations of 50-500 Hz in the sustained discharge rate in response to a tone burst and this oscillation frequency also correlates with best envelope frequency (Gdowski and Voigt, 1998). Fusiform cells of DCN have also shown to produce 40-100 Hz oscillations in their membrane potential that facilitate temporally precise spike generation (Manis et al., 2003). Despite these few studies of oscillatory activity, slow oscillations on the order of 1-5 Hz have not been observed or investigated.

Gap junctions

Electrical coupling between neurons plays an essential part in both the generation of oscillations as well as their synchrony (Draguhn et al., 1998; Gibson et al., 1999; Whittington and Traub, 2003). One remarkable feature of DCN circuitry is that different cell types are electrically coupled by connexin36-containing gap junctions (Figure 3) (Oertel and Young, 2004; Apostolides and Trussell, 2013b; Yaeger and Trussell, 2016). For example, superficial stellate cells and fusiform cells are all electrically coupled in both a hetero- and homologous fashion (Apostolides and Trussell, 2014). The functional impact of these electrical connections has yet to be explored. Fine-scale spike synchrony between fusiform cells of similar best frequencies is observed *in vivo*, so it is possible that electrical connections could mediate this synchrony (Voigt and Young, 1988; Gochin et al., 1989; Stefanescu and Shore, 2015, 2017). However, the coupling strength is rather weak, so it is more likely that this synchrony is driven by shared inputs.

Do animals have hearing loss when gap junctions are compromised? Cx36 KO mice experience impairments in hippocampal gamma oscillations, memory, neural synchrony, and vision (Frisch et al., 2005). Blakley et al. (2015) is the only study that has performed hearing tests in Cx36 KO mice. They found elevated auditory brainstem response (ABR) thresholds, but no effect on DPOAEs (distortion product otoacoustic emissions). DPOAEs test whether the biomechanics of the cochlea are intact, suggesting that the shift in ABR threshold results from brainstem rather than cochlea or inner ear deficits. These authros did not probe more complicated hearing tasks such as sound localization or frequency discrimination, where other hearing deficits may be

apparent. However, the shift in ABR threshold suggests that functioning electrical connections are required for proper hearing.

Summary

Chapter 2 of this dissertation explores the slow 1-2 Hz oscillations in the resting membrane potential in fusiform cells, the principal neuron of the DCN. We measured the intrinsic resonant frequency of fusiform cells and determined which conductances underlie the oscillations in order to understand the biophysical mechanisms by which they occur. We found that external Ca^{2+} concentration is a critical factor in regulating oscillations such that they can only be observed when concentrations are closer to physiological levels. Finally, we studied how electrical coupling of fusiform cells enables the synchronization of slow oscillations. Only fusiform cells that were located close together were coupled, suggesting that cells within the same tonotopic domains couple and oscillate together.

CHAPTER 1. CO-RELEASE OF INHIBITORY NEUROTRANSMITTERS IN THE MOUSE AUDITORY MIDBRAIN

Lucille A. Moore[1,2] & Laurence O. Trussell[2]

[1]Neuroscience Graduate Program

[2]Oregon Hearing Research Center and Vollum Institute, Oregon Health and Science University, Portland, Oregon 97239

Abstract

The central nucleus of the inferior colliculus (ICC) of the auditory midbrain integrates the majority of ascending auditory information from lower brainstem regions. It receives prominent long-range inhibitory input from the ventral nucleus of the lateral lemniscus (VNLL), a region thought to be important for temporal pattern discrimination. Histological evidence suggests that neurons in the VNLL release both glycine and GABA in the ICC, but functional evidence for their co-release is lacking. We took advantage of the GlyT2-Cre mouse line (both male and female) to target expression of ChR2 to glycinergic afferents in the ICC and made whole-cell recordings *in vitro* while exciting glycinergic fibers with light. Using this approach it was clear that a significant fraction of glycinergic boutons co-release GABA in ICC. Viral injections were used to target ChR2 expression specifically to glycinergic fibers ascending from the VNLL, allowing for activation of fibers from a single source of ascending input in a way that has not been previously possible in ICC. We then investigated aspects of the glycinergic versus GABAergic current components to probe functional consequences of co-release. Surprisingly, the time course and short-term plasticity of synaptic signaling were nearly identical for the two transmitters. We therefore conclude that the two neurotransmitters may be functionally interchangeable and that multiple receptor subtypes subserving inhibition may offer diverse mechanisms whereby inhibitory homeostasis is maintained.

Introduction

GABA is co-released with a variety of other neurotransmitters throughout the brain (Tritsch et al., 2016). One of the most paradoxical partners of GABA co-release is glycine as they are both fast inhibitory neurotransmitters. In the central auditory system, GABA/glycine co-release is particularly common during development (Kotak et al., 1998; Nabekura et al., 2004; Muller et al., 2006). However, co-release persists in adulthood in a variety of regions, including the lateral superior olive (LSO), medial nucleus of the trapezoid body, and dorsal cochlear nucleus (Helfert et al. 1992; Rubio 2004; Awatramani et al. 2005; Roberts et al. 2008; Weisz et al. 2016). Many functions of co-release have been proposed, including subserving tonic versus phasic inhibition via different time courses of glycinergic and GABAergic synaptic currents (Russier et al., 2002; Kuo et al., 2009; Xie and Manis, 2013), extra-fast inhibition (Lu et al., 2008), and compensation by one neurotransmitter during periods of sustained activity (Ishibashi et al., 2013; Fischl et al., 2014; Nerlich et al., 2014). Despite the common presence of and functional implications for GABA/glycine co-release in auditory brainstem regions, it has yet to be explored in the auditory midbrain.

The central nucleus of the inferior colliculus (ICC) is a nearly obligatory relay station for ascending streams of auditory information from the brainstem (Oliver 2005). Different types of auditory information coalesce in the ICC to create unique tuning properties that are then conveyed to the thalamus and cortex (Haplea et al., 1994; Joris et al., 2004; Loftus et al., 2010b). Multiple brainstem nuclei send glutamatergic, GABAergic, and glycinergic fibers to the ICC. Glycinergic input in particular originates largely from the ventral nucleus of the lateral lemniscus (VNLL) and lateral superior

olive (LSO), regions hypothesized to be important for temporal pattern discrimination and location of sound in space, respectively (Saint Marie et al. 1989; Covey & Casseday 1991; Glendenning et al. 1992, Oertel & Wickesberg 2002). The VNLL is a particularly unique structure because it is largely composed of inhibitory cell types and is one of the largest sources of input to ICC (Brunso-Bechtold et al. 1981; Saint Marie & Baker 1990; Winer et al. 1995, Saint Marie et al. 1997, reviewed by Cant 2005). A large fraction of cells in the VNLL across species express both glycine and GABA (Saint Marie et al. 1997; Riquelme et al. 2001; Tanaka & Ezure 2004), raising the possibility that projections from VNLL to ICC co-release these inhibitory neurotransmitters. However, functional evidence for co-release is difficult to demonstrate experimentally because of the anatomy of ascending projections. Ascending fibers from all lower brainstem regions enter the ICC through the same lemniscal fiber tract and there are multiple sources of pure GABAergic input that would be stimulated with electrical stimulation, making it unfeasible to activate glycinergic fibers in isolation in order to assay co-release.

Here we used a GlyT2-Cre mouse line (Ishihara et al., 2010) to express ChR2 in glycinergic cells and activate glycinergic fibers with photostimulation. ChR2 was targeted to glycinergic neurons either globally (by crossing the Cre line with a reporter line that expresses ChR2 in a Cre-dependent manner) or specifically within VNLL (via intracranial injection of AAV that induces Cre-dependent ChR2 expression). In this way we asked whether glycinergic afferents in the ICC co-release glycine and GABA and studied the possible functional consequences of this co-release. We found that GABA was consistently co-released with glycine from individual terminals in the auditory

midbrain, but the postsynaptic effects of the two transmitters were almost identical. Targeted expression of ChR2 to glycinergic fibers ascending from VNLL yielded similar results to global glycinergic stimulation. Indeed, our data suggest that putative roles for GABA/glycine co-release in lower brain regions are not recapitulated in the auditory midbrain, leaving the possibility open that the two neurotransmitters are functionally interchangeable.

Materials and Methods

Animals

All procedures involving animals were approved by OHSU's Institutional Animal Care and Use Committee. Optogenetic experiments were performed using heterozygous GlyT2-Cre;ChR2 mice generated by crossing GlyT2-Cre mice (Tg(Slc6a5-cre)KF109Gsat/Mmucd, RRID:MMRRC_030730-UCD) with the floxed ChR2(H134R)-EYFP Cre Ai32 reporter line (B6.Cg-Gt(ROSA)26Sor$^{tm32(CAG-COP4*H134R/EYFP)Hze}$/J, RRID:IMSR_JAX:024109). This cross resulted in the expression of ChR2 targeted to glycinergic neurons (Lu and Trussell, 2016). Miniature inhibitory postsynaptic current (mIPSC) recordings were made from wild-type C57BL/6 mice against which all transgenic lines were bred. Male and female mice postnatal days 19 to 35 were used for experiments. Specifically, an age range of 19 to 35 was used for experiments utilizing wild type or GlyT2-Cre;ChR2 mice and an age range of 29 to 35 was used for experiments in which GlyT2-Cre mice were injected with virus to induce region-specific ChR2 expression (see "Stereotactic injections" below). This wide age range apparently did not introduce variability in our dataset as there was no significant relationship between age and the percentage of the postsynaptic current attributed to

GABA release in either the GlyT2-Cre;ChR2 dataset (n=28 cells, R^2=0.028, p=0.39, linear regression) or the viral injection dataset (n=15 cells, R^2=0.006, p=0.78, linear regression). Age also did not correlate with IPSC decay in either the GlyT2-Cre;ChR2 dataset (n=26 cells, R^2=0.008, p=0.67, linear regression) or the viral injection dataset (n=13 cells, R^2=0.005, p=0.82, linear regression).

To control for Cre expression in the GlyT2-Cre line outside of glycinergic neurons, we crossed the GlyT2-Cre line with the floxed Ai9 tdTomato Cre reporter line (B6.Cg-*Gt(ROSA)26Sor*$^{tm9(CAG\text{-}tdTomato)Hze}$/J, RRID:IMSR_JAX:007909) and subsequently crossed Cre-positive offspring with a well-characterized GlyT2-EGFP mouse line (FVB.Cg-Tg(Slc6a5-EGFP)13Uze/UzeBsiRbrc, RRID:IMSR_RBRC04708; Zeilhofer et al. 2005). At one month of age, three of the resulting GlyT2-Cre/tdTomato: GlyT2-EGFP offspring were transcardially perfused with 4% paraformaldehyde (PFA). The brains were dissected out, postfixed overnight in 4% PFA, and sectioned on a vibratome at 50 µm thickness. Sections containing VNLL were counterstained with Hoechst 34580 (Thermo Fisher Scientific). Because the intensity of tdTomato and GFP varied between cells, we formulated a way to remove bias in determining whether cells were counted as positive for one, both, or neither. Using Adobe Illustrator CS6 (RRID:SCR_014198), we first used dots to mark tdTomato and GFP+ cell bodies when viewing these in separate channels. We used the Hoechst DNA counterstain to locate and label cells that were clearly negative for either. These templates were then merged to create a single template that marked cell bodies throughout the VNLL. This single template was overlaid on red and green channels separately and points were deleted if they labeled a soma that was negative for the respective fluorophore. Finally, the two maps of

tdTomato- and EGFP-positive cell bodies were overlaid and compared to identify the percentage of Cre/tdTomato-expressing neurons that were EGFP-negative and therefore unlikely to be glycinergic.

Brain slice preparation

Mice were anesthetized with isofluorane, decapitated, and coronal slices containing ICC (220 μm thick) were cut in warm (35°C) ACSF on a vibratome (Leica VT1200S). ASCF contained (in mM) 130 NaCl, 2.1 KCl, 1.2 KH_2PO_4, 1.7 $CaCl_2$, 1 $MgSO_4$, 20 $NaHCO_3$, 3 Na-HEPES, 10–12 glucose, 0.4 ascorbate, and 2 Na pyruvate and bubbled with 5% CO_2/95% O_2 (300 – 310 mOsm). Slices recovered at 34° C ACSF for 30 minutes and were then kept at room temperature until use.

Electrophysiology

Brain slices were contained in a chamber that was perfused with ACSF (~3 ml/min) heated to 31-33° C by an inline heater. Neurons in the ICC were visualized with Dodt contrast optics using a 40X objective on an upright microscope (Zeiss Axioskop2). The ICC was identified as the central area of the inferior colliculus in coronal slices where the tissue was harder to visualize due to the abundance of myelinated lemniscal fibers. The VNLL was identified by anatomical location as well as a concentration of EYFP-expressing cells in slices obtained from the GlyT2-Cre:ChR2(H134R)-EYFP reporter cross. Whole-cell patch-clamp recordings from ICC and VNLL neurons were made with a Multiclamp 700B amplifier. Data were filtered at 10 kHz, digitized at 20 kHz by Digidata 1322A, and acquired by pClamp 10.4 software (Molecular Devices, RRID:SCR_011323).

Intrinsic ChR2 currents were measured in neurons of the VNLL by blocking synaptic transmission with 5 μM NBQX, 10 μM MK-801, 10 μM SR95531, and 500 nM strychnine. In voltage clamp, exposing cells to a 50-ms light pulse would necessarily result in a long inward current. In the ICC, inhibitory postsynaptic currents were measured in response to either ChR2 stimulation or stimulation of fibers with a bipolar electrode made from borosilicate theta glass (Sutter Instrument #BT-150-10; henceforth "theta stimulation"). Wide-field photostimulation was achieved by coupling a 470 nm LED to the epifluorescence port of the microscope and delivering brief (1-2 ms) pulses of light with pClamp. Fibers were stimulated electrically by 0.1-0.2 ms square wave pulses (2-20 V) produced by pClamp and delivered through an isolation unit (AMPI ISO-Flex). Recording electrodes (4-6 MOhm) were pulled from borosilicate glass (WPI 1B150F-4) by a vertical puller (Narishige P-10). The internal pipette solution used for recording mIPSCs contained (in mM) 115 CsCl, 10 HEPES, 4.5 $MgCl_2$, 10 EGTA, 4 Na_2-ATP, and 0.5 Tris-GTP with pH adjusted to 7.25 with CsOH and osmolality adjusted to 290 mOsm with sucrose. The calculated chloride reversal potential (E_{Cl}) was -2.3 mV. The internal solution used for all other experiments contained (in mM) 113 K gluconate, 2.75 $MgCl_2$ hexahydrate, 1.75 $MgSO_4$, 0.1 EGTA, 9 HEPES, 14 Tris-phosphocreatine, 4 NA_2-ATP, and 0.3 tris-GTP with pH adjusted to 7.25 with KOH and osmolality adjusted to 290 mOsm with sucrose (E_{Cl} = -84.8 mV). For this internal solution, holding potentials cited in the text are corrected for a -13 mV junction potential. Series resistance (<20 MOhm) was compensated by 60-80% 'correction,' 90% 'prediction' (bandwidth=3 kHz). Data were excluded from analysis if series resistance changed by more than 25% over the course of the experiment.

Firing patterns were studied by holding cells in current clamp, delivering a bias current as needed to stabilize the resting potential at -65 mV (unbiased resting potentials typically ranged from -60 to -65 mV), and delivering a 500-ms current step ranging from -500 pA to +500 pA in 50-pA increments. Neurons recorded in VNLL displayed firing properties characteristic of VNLL neurons in mouse and gerbil (Caspari et al. 2015; Franzen et al. 2015). The cells recorded from ICC were organized into five different categories based on differences in firing pattern. *Sustained* neurons fired action potentials over the duration of positive current steps with varying levels of adaptation. *Sustained, Ih* neurons were similar except they showed prominent depolarizing sag at the onset of a hyperpolarizing current step. Cells categorized as *transient* fired multiple spikes only at the beginning of positive current steps while *onset* cells fired only one or two spikes at most at the beginning of a positive step. Finally, *pauser* cells displayed either a buildup in depolarization that preceded spiking or a long interspike interval after the first action potential. This was sometimes accompanied by acceleration in firing frequency over the length of the train.

All reagents were purchased from Sigma-Aldrich with the exception of SR-95531, which was purchased from Tocris Bioscience.

mIPSC analysis

mIPSCs were recorded in 1 μM tetrodotoxin (TTX) to block spontaneous spike-driven events, 10 μM zolpidem and 30 μM pentobarbital to slow the GABAergic component, and 5 μM NBQX/5 μM MK-801 to block AMPA/NMDA receptors. Glycinergic and GABAergic mIPSCs were recorded in isolation using 5 μM SR95531 and 500 nM strychnine respectively. Individual events were first detected in AxoGraph X

1.5.4 (RRID:SCR_014284) using a synaptic template with variable amplitude and then checked by eye to remove spurious events (Clements and Bekkers, 1997). To calculate that portion of the total amplitude contributed by glycine or $GABA_A$ receptors (Jonas et al., 1998; Awatramani et al., 2005), individual mIPSCs were force-fit with the dual exponential equation below:

$$Amplitude = A_{FAST} * exp^{(-t/\tau FAST)} + A_{SLOW} * exp^{(-t/\tau SLOW)}$$

A and *τ* represent amplitude and decay time constant values associated with fast glycinergic and slow GABAergic currents. The average decay time constants measured for glycinergic and GABAergic mIPSCs were measured individually for each cell recorded in 5 μM SR95531 and 500 nM strychnine, respectively. These average values were used for *τFAST* and *τSLOW*.

Stereotactic injections

GlyT2-Cre mice of both sexes (P16-19) were injected with AAVrh10.CAGGS.flex.ChR2.tdTomato.-WPRE.SV40 (UPENN AV-10-18917P) to induce the expression of ChR2 in cells of the VNLL in a Cre-dependent manner. The AAV (serotype 2/1) expresses ChR2 and tdTomato under the control of a FLEX switch that makes expression dependent on the presence of Cre. The transgenes were driven by the CAG promoter and included a WPRE element and SV40 polyadenylation signal to enhance expression (Atasoy et al., 2008). Recordings were made in ICC starting 14 days after injections. Mice were anesthetized with 1% isoflurane and stabilized in a stereotaxic instrument (David Kopf). An unilateral craniotomy was made using a dental

drill (Foredom K.1070) and a beveled glass capillary micropipette (inner diameter of 20-30 μm) attached to a hydraulic injector (Narishige) was used to deliver 30 nl AAV at a speed of 5 nl/sec. The micropipette was advanced into and out of the brain tissue at a speed of ~5 μm/sec, with a 5-minute wait time at the injection site before and after injection. The coordinates we used for VNLL were (in mm from Bregma): -3.2 posterior, 1.3 lateral, and 5.2 deep from the pia.

Experimental Design & Statistical Analyses

Electrophysiological traces were analyzed with pClamp 10.4 software or custom-written procedures in IGOR Pro 6.3. Statistics (RRID:SCR_000325) were performed and graphs created using GraphPad Prism 7 (RRID:SCR_002798). Averages are represented as mean ± SEM. Data was tested for assumptions of equal variances (Bartlett's test) between groups and normality (Shapiro-Wilk test) before using parametric tests. One-way ANOVA with repeated measures was used for comparisons across treatments within single cells followed by Tukey *post hoc* comparisons (P values for *post hoc* comparisons are reported only when the p-value associated with the main effect is significant). Alternatively, for paired and unpaired data respectively, the Friedman test and Kruskal-Wallis with Dunn's *post hoc* tests were used if the data were not normally distributed. Multiple comparisons were controlled for by selecting the "multiplicity adjusted P value" option in Prism 7. Sphericity and effective matching were also tested for when using ANOVAs. Two-way ANOVA with repeated measures on one or both factors (for data collected within single cells across conditions) was used to compare short-term synaptic depression in Figure 1.7. P, F, and df values reported for two-way ANOVAs are those associated with the main effect and P values associated

with the interaction term are reported only if significant. Data are displayed as box-and-whisker plots with the median value marked within the "box" extending from the 25th to 75th percentiles. The Tukey method was used to create the "whiskers" in which the interquartile distance is multiplied by 1.5 and extended from the edges of the box. Data outside of this calculated range are plotted as points. Conversely, if these calculated values were outside of the minimum or maximum values of the dataset, the whiskers were instead set to the respective minimum and maximum values.

Results

Ascending afferents in the inferior colliculus co-release glycine and GABA

One of the largest ascending sources of inhibition to the ICC is the VNLL, an auditory region putatively important for temporal pattern discrimination (Brunso-Bechtold et al. 1981; Saint Marie & Baker 1990; Winer et al. 1995, Saint Marie et al. 1997, Oertel & Wickesberg 2002). Curiously, histological evidence shows that a large fraction of cells in the VNLL of multiple species express both GABA and glycine (Saint Marie et al. 1997; Riquelme et al. 2001; Tanaka & Ezure 2004). We therefore asked whether glycinergic afferents entering the ICC co-release glycine and GABA.

Glycine and GABA are packaged into presynaptic vesicles by the same vesicular transporter VGAT (Wojcik et al., 2006). To verify the co-release of both inhibitory neurotransmitters from the same synapse, we recorded miniature IPSCs (mIPSCs), the postsynaptic consequence of a single vesicle released presynaptically. Spontaneous vesicular release was blocked by the inclusion of 1 μM tetrodotoxin in the bath. Miniature events were recorded with pipettes containing a high chloride internal solution to increase the amplitude of the currents. The inhibitory currents are inward under these

conditions. mIPSCs had uniformly rapid kinetics that were well fit with a single exponential, giving an average decay of 3.3 ± 0.1 ms (n=618 mIPSCs for control cell displayed in Figure 1.1A). The homogenous kinetics made the differentiation of glycinergic and GABAergic components problematic. To address this confound, we added 10 μM zolpidem and 30 μM pentobarbital to the bath to slow $GABA_A$ receptor kinetics (Figure 1.1A) (Zhang et al., 2008; Apostolides and Trussell, 2013a). This revealed slower GABAergic currents, some of which appeared to be combined with fast glycinergic currents within a single vesicular release event (Figure 1.1A: see starred events).

Glycinergic and GABAergic components were therefore distinguished based on their differing kinetics, allowing us to detect single mIPSCs with dual components following the analysis technique of Jonas *et al.* (1998). When isolated pharmacologically (see Methods), the average decay time constants for glycinergic (Figure 1.1B "+SR95531") and GABAergic (Figure 1.1B "+strychnine") mIPSCs were 2.8 ± 0.2 and 25.7 ± 1.2 ms respectively (n=6 cells, average 730 ± 102 glycinergic and 723 ± 85 GABAergic mIPSCs analyzed per cell; Figure 1.1C). Following Jonas et al. 1998, these values were used in a double exponential equation where the two time constants are fixed and the amplitude values associated with each time constant are free-floating (see Methods). Force-fitting this equation to individual events yields amplitude values associated with each time constant that together account for the full amplitude of the current. For example, the total amplitude of a purely glycinergic mIPSC should be fully accounted for by the amplitude associated with the fast decay time constant. In Figure 1.1D, each point represents a single mIPSC recorded from a cell using the slow

GABAergic and fast glycinergic amplitude values resulting from force-fitting the double exponential equation. The plot to the right shows the results of force-fitting events recorded from the same cell in the presence of either GABA or glycine receptor blockers. In the presence of GABA receptor blockers (green points), it appears that the majority of the full amplitude of each event can be explained by glycine receptor kinetics, while the opposite holds in the presence of glycine receptor kinetics (purple points). The dotted gray lines mark two standard deviations from the mean. Points that fall above these lines are regarded as containing both glycinergic and GABAergic components and appear in abundance in control conditions (blue points, Figure 1.1D). The percentage of mIPSCs that were regarded as containing dual components in baseline conditions was 22.9 ± 2.8 % (n=6 cells, Figure 1.1E). Using this method, the percentage of events classified as having dual components after the addition of strychnine or SR95531 was only 1.8 ± 0.2% (n=6 cells). Furthermore, 53.0 ± 10.3 % (n=6 cells) of the mIPSCs identified as containing a significant glycine receptor component also contained a significant GABA receptor component. These results indicate that GABA and glycine can be released from the same synaptic vesicle in terminals in ICC.

Spike-triggered co-release of glycine and GABA

The previous analysis shows that vesicles containing both transmitters may fuse spontaneously, but does not indicate whether such co-release occurs during normal spike-triggered exocytosis. However, analysis of evoked release is not straightforward because electrical stimulation of fibers within the ICC would inevitably activate purely GABAergic interneurons as well as the glycinergic input fibers. While it is feasible to

electrically stimulate ascending axons as they enter the ICC ventrally, this lemniscal fiber bundle also contains fibers from purely GABAergic regions, such as the dorsal nucleus of the lateral lemniscus (DNLL). Therefore, to further study co-release in the ICC, we used the GlyT2-Cre mouse line to achieve targeted optical activation of ascending glycinergic input to the ICC (Figure 1.2). The GlyT2-Cre mouse line effectively drives Cre expression in greater than 80% of glycine-immunoreactive cells in the brainstem and spinal cord (Ishihara et al., 2010). Therefore, when crossed with a Cre-dependent reporter line to induce expression of tdTomato in Cre-expressing cells, tdTomato-positive somata are present throughout auditory brainstem areas known to contain glycinergic cell bodies, including the VNLL (Figure 1.2Ai-iii) and LSO (Figure 2Bi-ii). Notably, cell bodies are absent from regions that are known to contain many GABAergic neurons but not glycinergic cells, such as the ICC (Figure 1.2Bi) and DNLL (not shown). To verify that Cre expression is limited to glycinergic neurons in the auditory brainstem, we crossed the GlyT2-Cre line with a floxed tdTomato reporter line (Ai9) and subsequently crossed the offspring to the GlyT2-EGFP line that labels greater than 90% of glycinergic neurons in the cerebellum and throughout the brainstem (Zeilhofer et al., 2005). We analyzed the VNLL (Figure 1.2Aii-iii) for co-label of tdTomato and EGFP within cell bodies. Across three animals, an average of 3.0 ± 0.7% of the Cre-expressing cells in the VNLL were GFP-negative and may therefore release only GABA or glutamate in the ICC with light stimulation (somas counted per animal = 222, 423, 194). We believe this small percentage is unlikely to change the interpretation of our results.

Global expression of ChR2 in glycinergic neurons allowed us to stimulate fibers from all ascending sources of glycinergic input to the ICC. Previous studies showed that the GlyT2-Cre;ChR2 cross effectively allows for light-evoked activation of glycinergic neurons (Lu and Trussell, 2016). We confirmed that photostimulation was effective in our preparation by making whole-cell recordings from the VNLL, the largest source of glycinergic input to the ICC. With synaptic transmission blocked, cells in the VNLL displayed an intrinsic ChR2 current in response to blue light, and spiked reliably in response to 1-2 ms light stimulation (Figure 1.3A). We made whole-cell recordings from cells in the ICC and stimulated IPSCs from ascending glycinergic afferents with blue-wavelength light (Figure 1.3B). Voltage clamping cells at -60 mV, the average light-evoked IPSC was 362.2 ± 46.98 pA (n=29 cells). The currents were large enough that low internal chloride solution was sufficient, so the inhibitory postsynaptic currents henceforth are outward. The theoretical chloride reversal potential was -84.5 mV while the measured reversal potential was -84.3 ± 1.2 mV (n=4 cells). The addition of GABA receptor antagonist SR95531 (5 μM) or glycine receptor antagonist strychnine (500 nM) revealed an average GABAergic component of 31 ± 4% of the evoked currents (n=29 cells; Figure 1.3B-E). This concentration was sufficient to block the entire slow-decaying mIPSC component in the presence of $GABA_A$ modulators (Fig. 1.1D). Together, the percentage of the IPSC that was GABAergic ranged quite widely, from 7.1 to 71.9% (Figure 1.3E).

We compared the kinetics of glycinergic and GABAergic components within single postsynaptic cells to probe for possible functional differences in the signaling of these co-released neurotransmitters. For each cell, one component was

pharmacologically isolated while the other component was digitally isolated by subtracting the pharmacologically isolated current from the control trace. Half of the experiments in Figure 1.3 were performed by adding SR95531 first and digitally recreating the GABAergic current while the other half were performed by adding strychnine first and digitally recreating the glycinergic current. This approach should remove systematic bias in kinetic measurements resulting from the noise added to a digitally subtracted current. IPSCs were well fit with a monoexponential decay (Figure 1.4A). The decay time constant of the isolated GABAergic component, 3.73 ± 0.24 ms, was similar but significantly slower than the isolated glycinergic component, 3.02 ± 0.23 ms (Figure 1.4B; control 3.34 ± 0.21 ms, n=22 cells, F=11.00, p=0.0041, Friedman test; *post hoc* glycinergic *vs.* GABAergic p=0.0027). The fast time course of the GABAergic component was expected given the kinetics observed in our miniature IPSC recordings in control solutions. Glycinergic decays measured from evoked events were not different from mIPSC events (mIPSC n=6 cells, eIPSC n=22 cells, t(26)=0.42, p=0.67, two-tailed t-test). Rise time (20-80%) was also significantly slower for the GABAergic component (0.93 ± 0.08 ms) compared to the glycinergic component (0.79 ± 0.05 ms, control 0.80 ± 0.04 ms; Figure 1.4B; n=24 cells, F(2,23)=4.79, p= 0.027, repeated measures one-way ANOVA; *post hoc* GABAergic *vs.* glycinergic p=0.039). The paired-pulse ratio collected with an inter-stimulus interval of 100 ms was similar between groups (control 0.70 ± 0.04, glycinergic 0.61 ± 0.05, GABAergic 0.71 ± 0.06; n=11 cells, F(2,10)=1.45, p=0.26, repeated measures one-way ANOVA).

To control for unforeseen effects of light stimulation on decay times, we compared the kinetics of isolated glycinergic IPSCs evoked by light versus theta

electrode stimulation measured from the same cells in GlyT-Cre/ChR2(H134R) Cre reporter tissue (Figure 1.4C). Light-evoked IPSCs (200.2 ± 52.4 pA) were about two times larger than theta-evoked (95.5 ± 24 pA), suggesting that the theta electrode effectively stimulated around half of the total portion of glycinergic inputs, assuming light can trigger spikes in all glycinergic fibers (Figure 1.4D; n=7 cells, t(6)=2.89, p=0.028, paired two-tailed t-test). However, light-evoked (2.24 ± 0.30 ms) versus theta-electrode-evoked (2.20 ± 0.34 ms) IPSCs had similar decay time constants (n=7 cells, t(6)=0.11, p=919, paired two-tailed t-test) and rise times (0.63 ± 0.06 ms *vs.* 0.91 ± 0.21 ms; n=7 cells, t(6)=1.26, p=0.25, paired two-tailed t-test). Kinetic measures therefore appear to be unaffected by light stimulation. Isolated GABAergic IPSCs were also recorded with theta stimulation to determine whether slower IPSCs could be observed. This would presumably activate either co-releasing and/or pure sources of GABAergic input, including local GABAergic input. However, slower IPSCs were not observed.

Targeted stimulation of afferents from VNLL reveals co-releasing fibers

A prominent source of glycinergic input to the ICC comes from the VNLL. We therefore targeted expression of ChR2 to glycinergic neurons of the VNLL (see Methods), allowing for greater specificity in the source of stimulated fibers compared to global expression of ChR2 in glycinergic neurons. Intracranial viral injections resulted in infected cell bodies clearly localized to the VNLL (Figure 1.5A left) and heavy fiber labeling in the ipsilateral ICC (Figure 1.5A right). The average IPSC amplitude evoked from virally injected animals (156.5 ± 32.2 pA, n=15 cells) was about one third the size of IPSCs recorded in transgenic mice with global ChR2 expression in glycinergic fibers (368.0 ± 45.8 pA, n=29 cells, Figure 1.5B-C). This difference in amplitude could not be

accounted for by the relatively older age range for virally injected animals as there was no correlation between age and IPSC amplitude in either the GlyT2-Cre;ChR2 dataset (n=30 cells, R^2=0.010, p=0.60, linear regression) or the viral injection dataset (n=15 cells, R^2=0.007, p=0.77, linear regression). Compared to IPSCs measured with global stimulation of glycinergic input (31 ± 4%, n=29 cells), IPSCs resulting from light stimulation of glycinergic fibers from the VNLL were 42 ± 5% GABAergic (n=15 cells, Figure 1.5D; these values are not statistically different: t(42)=1.77, p=0.11, two-tailed t-test).

We compared kinetic parameters between isolated glycinergic and GABAergic components and the findings were similar to what was seen with global stimulation. Decay times were similar but significantly slower for GABAergic (3.94 ± 0.33 ms) versus glycinergic (2.97 ± 0.19 ms) currents (Figure 1.5E; control 3.53 ± 0.17 ms, n=13 cells, F(2,12)=8.09, p=0.0021, repeated measures one-way ANOVA; *post hoc* GABAergic *vs.* glycinergic p=0.0015). Unlike with global stimulation, the GABAergic rise time (1.09 ± 0.15 ms) was slightly but significantly slower than the average rise time measured in control conditions (0.91 ± 0.13 ms) or from the isolated glycinergic IPSC (0.92 ± 0.11 ms) (Figure 1.5F; n=13 cells, F=9.39, p=0.0092, Friedman test; *post hoc* GABAergic *vs.* control p=0.0324, GABAergic *vs.* glycinergic p=0.0181).

All biophysical subtypes of ICC neurons received co-released input

Given the wide variation in the fraction of the IPSC contributed by GABA, we asked if this might vary with cell type in the ICC. Classification schemes of cell types in the ICC based on morphology, neurotransmitter content, and biophysical properties have not yet correlated in such a way to define agreed-upon subsets of neurons (Reetz

and Ehret, 1999; Peruzzi et al., 2000; Bal et al., 2002; Wallace et al., 2012). We therefore categorized the firing properties of cells from which we recorded into five groups (Figure 1.6) and compared these to the profile of inhibition. All five subtypes displayed light-evoked IPSCs as well as evidence for dual components based on the addition of either glycine- or GABA-receptor antagonists to the bath. The average percentage GABAergic component present in the IPSCs of each cell type are as follows (followed by the number of cells in which % GABAergic component was determined out of the total number of the cell type recorded from that received input from photostimulation of glycinergic fibers): *sustained, Ih* 32 ± 6% (n=12 out of 54 cells), *sustained* 31 ± 6% (n=6 out of 14 cells), *pauser* 44 ± 8% (n=5 out of 8 cells), *strongly adapting* 37 ± 9% (n=5 out of 18 cells), and *onset* 7.1% (n=1 out of 4 cells). Excluding the onset subtype, there was no difference in the percentage GABAergic component between cell types (n=28 cells, $F(3,24)=0.65$, $p=0.590$, one-way ANOVA). Furthermore, general features of the IPSCs were similar between cell types, including amplitude (n=29 cells across subtypes, $F(3,25)=1.74$, $p=0.184$, one-way ANOVA) and decay time (n=26 cells across subtypes, $F=3.09$, $p=0.377$, Kruskal-Wallis).

High-frequency stimulation of co-releasing fibers does not support unique roles for GABA and glycine in short-term synaptic depression

Co-released glycine and GABA at some auditory brainstem synapses differ in their short-term synaptic plasticity, particularly under periods of high activity. This may endow the neurotransmitters with unique roles in maintaining inhibition (Ishibashi et al., 2013; Fischl et al., 2014; Nerlich et al., 2014). Besides enabling a glycine-source specific comparison of amplitudes and kinetics, injections in the VNLL of the viral

construct allowed us to study short-term synaptic plasticity in greater detail. This advantage became clear when, using the transgenic cross described above, we observed that light stimulation resulted in greater short-term synaptic depression compared to theta electrode stimulation (data not shown). We reasoned that this difference in plasticity may result from ChR2 desensitization if the expression levels of ChR2 are just sufficient to drive spikes for a limited number of stimuli. Virally-induced ChR2 expression results in higher expression levels of ChR2 that may compensate for this desensitization. Indeed, we found that during trains of stimuli, relative amplitudes of IPSCs evoked by light stimulation matched those of theta electrode stimulation for up to 50 Hz in virally-injected animals (Figure 1.7A-B; light $n_{10,20,50\ Hz}$=24, 18, 21 cells; theta $n_{10,20,50\ Hz}$=5, 6, 6 cells; $F_{10,20,\ 50\ Hz}$=2.48, 1.48, 0.25; $df_{10,20,50\ Hz}$=(1,27), (1,22), (1,25); $p_{10,20,50\ Hz}$=0.1267, 0.2375, 0.6208, two-way ANOVAs with repeated measures; 10 Hz data showed a significant interaction (p=0.0083), but *post hoc* comparisons were NS).

Given the reliability of the measurements with virally expressed ChR2, we next used this preparation to test whether the relative contribution of glycine and GABA to the postsynaptic current is dependent on the length and frequency of stimulation, which might suggest selective depletion of one transmitter *vs*. the other. However, no difference in synaptic depression was observed between control conditions and in the presence of strychnine when stimulating a train of ten spikes at 10 Hz (Figure 1.7C; n=9 cells, F(1,8)=0.682, p=0.4328, two-way ANOVA with repeated measures on both factors). There was also no difference in depression when stimulating at a higher frequency for a longer time period, specifically driven at 50 Hz for 1 second (n=10 cells, F(1,9)=3.5, p=0.0942, two-way ANOVA with repeated measures on both factors). These

results indicate that the relative contributions of GABA and glycine to the total IPSC remains constant even during long trains of stimuli.

$GABA_B$ receptors are located on glutamatergic (Sun et al., 2006) and GABAergic (Ma et al., 2002b) terminals in the ICC. We confirmed that glycinergic terminals likely express $GABA_B$ receptors as well: the addition of $GABA_BR$ agonist 10 μM baclofen decreased the amplitude of light-evoked IPSCs by an average of 39±8% (Figure 1.8Ai-ii; ACSF 286.6 ± 91.5 pA, baclofen 167.6 ± 53.2 pA, wash 258.6 ± 87.1 pA; n=10 cells, F=11.14, p=0.0012, Friedman test; *post hoc* ACSF *vs.* baclofen p=0.004, baclofen *vs.* wash p=0.005; n=10 cells, F(2,9)=1.23, p=0.3157, repeated-measures one-way ANOVA). While activation of pre-synaptic $GABA_BRs$ is also expected to change paired-pulse depression, no change was observed (Figure 1.8Aiii; ACSF 0.76 ± 0.05, baclofen 0.75 ± 0.05, wash 0.75 ± 0.05; n=10 cells, F(2,9)=1.23, p=0.3157, repeated-measures one-way ANOVA). However, baclofen did not affect the input resistance or bias current of the cells recorded from, and we conclude that paired pulse ratio may not be robust indicator of the expected presynaptic change (input resistance averages 494.6 ± 115.7 MΩ in ACSF, 432.5 ± 85.2 MΩ in baclofen; n=9 cells, t(8)=1.35, p=0.214, paired t-test: bias current averages -25.3 ± 24.3 pA in ACSF, -10.6 ± 31.1 pA in baclofen; n=10 cells, t(9)=1.45, p=0.1819, paired t-test).

In vivo, iontophoresis of $GABA_B$ receptor blockers alters response to tones (Vaughn et al., 1997), but the source of the GABA that reaches these receptors is unknown. We therefore tested whether the GABA co-released from glycinergic terminals could act on presynaptic $GABA_B$ receptors to affect the release probability of the synapse. However, there was no difference in depression in trains of 10 (Figure

1.8Bi) and 50 Hz (Figure 1.8Bii) stimuli before and after application of the $GABA_B$ receptor antagonist CGP55845 (2 μM) (n=5 cells, $F(1,4)_{10,50Hz}$=0.007, 2.147, $p_{10,50Hz}$=0.94, 0.22, two-way ANOVA with repeated measures on both factors). We also tested whether co-released GABA could inhibit glutamate release in ICC via activation of $GABA_B$ receptors located on glutamatergic terminals. We evoked EPSCs with theta stimulation (paired pulses, 100 ms interval) before and after intense photostimulation of glycinergic fibers (50 Hz 1 ms light pulses delivered for 5 seconds; Figure 1.8Ci). If the co-released GABA reaches $GABA_B$ receptors on glutamatergic terminals, this should depress release from these terminals, resulting in decreased EPSC amplitude and a larger ratio of the second to the first EPSC amplitude. However, similar to glycinergic fibers, there was no difference in either the amplitude of the first EPSC after intense photostimulation of glycinergic fibers (Figure 1.8Cii; average 156.2 ± 30.7 pA pre- *vs.* 157.6 ± 30.65 pA post-light train; n=10 cells, t(9)=0.59, p=0.57, paired t-test) or paired-pulse depression (Figure 1.8Ciii; average 0.85 ± 0.02 pre- *vs.* 0.87 ± 0.03 post-light train; n=10 cells, t(9)=1.12, p=0.29, paired t-test).

Discussion

We found that glycinergic fibers ascending to the ICC co-release glycine and GABA. We proceeded to probe the currents for differences that have been shown at other synapses to endow the neurotransmitters with unique functions. Surprisingly, co-released glycinergic and GABAergic currents in the ICC had strikingly similar features, including kinetics, contact with cell types in the ICC, short-term depression dynamics, and effect on pre-synaptic release. Therefore, despite the likely presence of co-release

in the auditory midbrain into adulthood, our data do not support popular hypotheses for the functions of co-release.

Glycinergic neurons are found only as far up the neuraxis as the lemniscal nuclei, and their collicular inputs are probably the highest density of glycinergic synapses in the brain. From the midbrain on, GABA is the primary inhibitory transmitter of projection and interneurons. Yet even in the ICC, glycinergic afferents, largely ascending from VNLL, co-release GABA with glycine, suggesting that co-release is a highly conserved feature of glycinergic terminals. One line of evidence supporting co-release in the ICC is the presence of dual decay components observed in mIPSCs, which are the result of the release of a single synaptic vesicle. Glycine and GABA use the same vesicular transporter and are therefore packaged together into the same vesicle if both present at the synaptic terminal (Wojcik et al., 2006). Mixed components within mIPSCs can be distinguished via differing receptor pharmacology and kinetics. Using allosteric modulators of the $GABA_A$ receptor to slow its decay, we found that 22.9 ± 2.8% of the mIPSCs were mixed. This percentage is an underestimation of the fraction of glycinergic terminals releasing GABA because the estimate also includes mIPSCs from GABAergic cells within the ICC. Co-release is further supported by the fact that GABAR-mediated currents are recorded from cells in the ICC with targeted light stimulation of glycinergic fibers. Co-release has been described as characteristic of neonatal cells (< 10 days old, Nabekura et al. 2004; Muller et al. 2006). However, we find prominent co-release in mature animals, which is consistent with immunohistochemical studies performed in adult animals and suggests functional

importance of co-release in the mature ICC (Saint Marie et al. 1997; Riquelme et al. 2001; Tanaka & Ezure 2004).

One way in which co-released GABA and glycine could serve different functions is through differing postsynaptic kinetics, given that GABAergic currents typically decay more slowly (Russier et al., 2002). However, we found that in ICC, GABAergic currents were nearly as fast as glycinergic currents (3.7 ms *vs.* 3.0 ms respectively). This observation is likely accounted for by the fact that the α1 subunit that endows GABA receptors with fast kinetics is more common in the ICC compared to α2 (Milbrandt et al., 1997; Wässle et al., 2009; Dixon et al., 2014). Another possibility is that GABA co-release in the IC shapes the kinetics of the glycinergic component of the IPSC. In trapezoid body neurons, GABA binds to glycine receptors as a co-agonist to accelerate IPSC decay times, yielding IPSCs with sub-millisecond kinetics (Lu et al., 2008). It is possible that GABA co-release is similarly required to very precisely fine-tune the time course of inhibitory input to optimally balance excitatory input (Kim and Fiorillo, 2017).

Our viral injections demonstrate that at least some portion of co-releasing fibers in the ICC ascend from the VNLL. The VNLL is largely a monaural region and is therefore thought to be important for recognition of temporal patterns (Oertel & Wickesberg 2002). A large population of cells in the VNLL show an onset pattern in response to sound stimuli with a stable first-spike latency across intensities (Zhang and Kelly, 2006; Liu et al., 2014). These cells likely receive their primary input from octopus cells of the cochlear nucleus (Adams, 1997; Pollak et al., 2011). The large inhibitory input from the VNLL to the ICC is therefore generally thought to provide precisely timed feed-forward inhibition that would sculpt the tuning properties of cells in the ICC,

particularly at the onset of sound (Covey & Casseday 1991; Nayagam et al. 2005; Xie et al. 2007). The IPSC amplitude evoked from virally injected animals was smaller than in transgenic mice, suggesting that neurons in the ICC receive glycinergic input from multiple cells. The kinetic features and percentage of GABAergic input from glycinergic fibers ascending from VNLL were similar to what we observed when stimulating global glycinergic input, suggesting that glycinergic inputs from LSO may have similar properties.

Viral injections into VNLL enabled us to examine dynamics of short-term synaptic depression for currents mediated by co-released GABA *versus* glycine. There was no difference in synaptic depression exhibited in the presence of GlyR blockers compared to control even with high-frequency stimulation, arguing against an activity-dependent shift in the GABA/glycine ratio observed at other co-releasing synapses (Ishibashi et al., 2013; Fischl et al., 2014; Nerlich et al., 2014). We also tested whether co-released GABA could act on pre-synaptic $GABA_B$ receptors to affect synaptic release as reported in AVCN and spinal cord (Chéry and De Koninck, 1999b; Lim et al., 2000). In the ICC, $GABA_B$ receptors are located on glutamatergic and GABAergic terminals (Ma et al., 2002b; Sun et al., 2006), with little evidence for postsynaptic $GABA_B$ receptors outside of the dorsal cortex (Sun et al., 2006; Sun and Wu, 2009). In this study, $GABA_B$ receptor agonist depressed the amplitude of light-evoked IPSCs by 39±8%. Though the paired-pulse depression was unaffected, it is likely that the $GABA_B$ receptors are largely pre-synaptic as $GABA_B$ receptor agonist shows no effect on the cells recorded from either in this or previous studies in ICC. We asked whether the co-released GABA could act on $GABA_B$ receptors to modify the release probability of either glycinergic or neighboring

glutamatergic fibers. However, intense photostimulation to maximize GABA release from glycinergic terminals did not change the release properties of either glycinergic or glutamatergic terminals. We therefore did not observe any evidence for a unique role for co-released GABA in $GABA_B$ receptor activation.

The balance of glycinergic and GABAergic transmission from co-releasing afferents not only relies on presynaptic loading of glycine and GABA into single vesicles, but also postsynaptic receptor expression. We therefore compared response properties to photostimulation across cell types in ICC categorized according to firing properties in response to current injection. We observed firing patterns similar to those described by Ono et al. (2005), except that we did not attempt to further categorize subtypes based on neurotransmitter content, levels of spike adaptation during the train, and firing rate. The *pauser* firing pattern is mediated by a fast inactivating K conductance known as A-type current (Sivaramakrishnan and Oliver, 2001). The sag and rebound displayed by all but *sustained* subtypes are likely mediated by Ih, a hyperpolarization-activated cation current (Koch and Grothe, 2003). The rebound hump present in *sustained* neurons lacking Ih could be accounted for by activation of calcium channels (Sivaramakrishnan and Oliver, 2001). All of these subtypes showed light-evoked IPSCs with similar GABA/glycine ratios and kinetic features (with the possible exception of *onset* cells). However, some types may be found to express a unique complement of inhibitory receptors as cell type definitions in the ICC are refined.

Given the strikingly similar features of glycinergic and GABAergic currents in ICC, it is possible that co-release provides a mechanism for finer inhibitory tuning via independent receptor modulation. Glycine transmission in this study made up the

majority of the IPSC amplitudes. Glycine receptors may therefore be relatively more important for setting strength of inhibition whereas GABA receptors, with their smaller unitary conductance and more complex subunit diversity, could allow for inhibitory refinement. Differential modulation of GABA and glycine receptors, by neurosteroids and zinc for instance, could also aid in tuning inhibition (Hosie et al., 2003; Belelli & Lambert 2005; Trombley et al., 2011). Independent receptor modulation coupled with the highly similar features of co-released GABA and glycine observed in this study may further permit the neurotransmitters to compensate for one another under conditions where one system is compromised (Takazawa et al., 2017). Aging, acoustic trauma, and tinnitus have all been associated with hyperactivity and decreased GABAergic activity in the IC (Caspary et al., 2008; Robertson and Mulders, 2012; Auerbach et al., 2014; Ropp et al., 2014). Interestingly, unilateral acoustic trauma or cochlear ablation results in decreased GABA release and $GABA_AR$ expression in IC without any persistent change in levels of glycine receptor mRNA or [^{3}H]strychnine binding (Suneja et al., 1998; Yan et al., 2007; Dong et al., 2010a, 2010b). Co-release may therefore provide a necessary redundancy that maintains the homeostasis of inhibition in the ICC.

In summary, current models about the functional impact of glycine and GABA co-release in the auditory brainstem are not supported in the auditory midbrain despite the fact that co-release likely persists into adulthood. However, the resulting diversity in postsynaptic receptors could serve to maintain homeostasis of inhibitory networks integrated by the ICC, including under conditions such as aging or acoustic trauma where one neurotransmitter system may be preferentially affected.

Acknowledgements

This work was supported by National Institutes of Health Grants DC004450 to L.O.T. and DC015187-01 to L.A.M. We thank members of the L.O.T. laboratory for helpful discussions and Ruby Larisch and Michael Bateschell for assistance with mouse colony management.

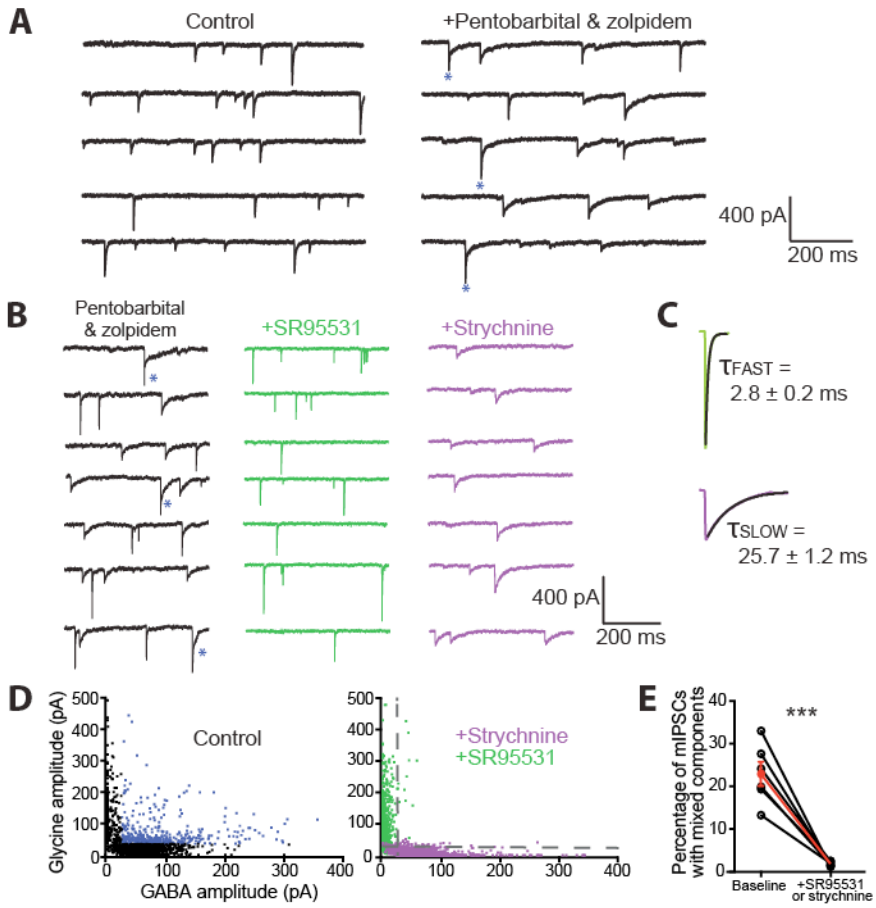

Figure 1.1. Co-release revealed through analysis of mIPSCs. **A:** Miniature IPSCs recorded from a neuron in the ICC in control conditions (left trace) appear homogeneous in the speed of their decay (recorded in 1 μM TTX with excitatory transmission blocked). However, when 10 μM zolpidem and 30 μM pentobarbital are added to the bath to increase the open probability of the $GABA_A$ receptor and effectively slow the current (right trace), dual-component mIPSCs are revealed (starred events). **B:** With zolpidem and pentobarbital in the bath, glycinergic and GABAergic mIPSCs have distinctly fast and slow kinetics, respectively. Displayed are miniature IPSCs recorded from the same neuron in control (left trace), 5 μM SR95531 to isolate glycinergic mIPSCs (middle trace), and 500 nM strychnine to isolate GABAergic mIPSCs (right

trace). **C:** Normalized and averaged glycinergic (green) and GABAergic (purple) mIPSCs. The average decays were 2.8 ± 0.2 and 25.8 ± 1.2 ms respectively. **D:** Scatter plots of amplitude values associated with fast and slow mIPSC components. In control conditions, individual events were force-fit with a dual exponential equation where the tau values were fixed using these averages and the associated amplitude values were left free-floating and plotted (left scatter plot represents the results from a single neuron). The pharmacologically isolated glycinergic (green points) and GABAergic (purple points) mIPSCs from the same neuron were force-fit with the same dual exponential equation and plotted (right scatter plot). The vertical dotted line represents 2*SD of the average amplitude associated with the slow decay time constant for glycinergic mIPSCs while the horizontal dotted line represents the same for the amplitude associated with the fast decay time constant for GABAergic mIPSCs. Points beyond these cutoff amplitudes are considered mixed events. In control conditions (left scatter plot), mixed events are labeled in blue and largely disappear in the presence of either blocker (right scatter plot). **E:** The percentage of mIPSCs that are mixed in control (average 22.9 ± 2.8%) is significantly higher compared to the fraction that is mixed with the addition of SR95531 or strychnine (average 1.9 ± 0.2%; n=6 cells, $t(5)=7.08$, $p=0.0009$, two-tailed t-test). ***$p<0.001$.

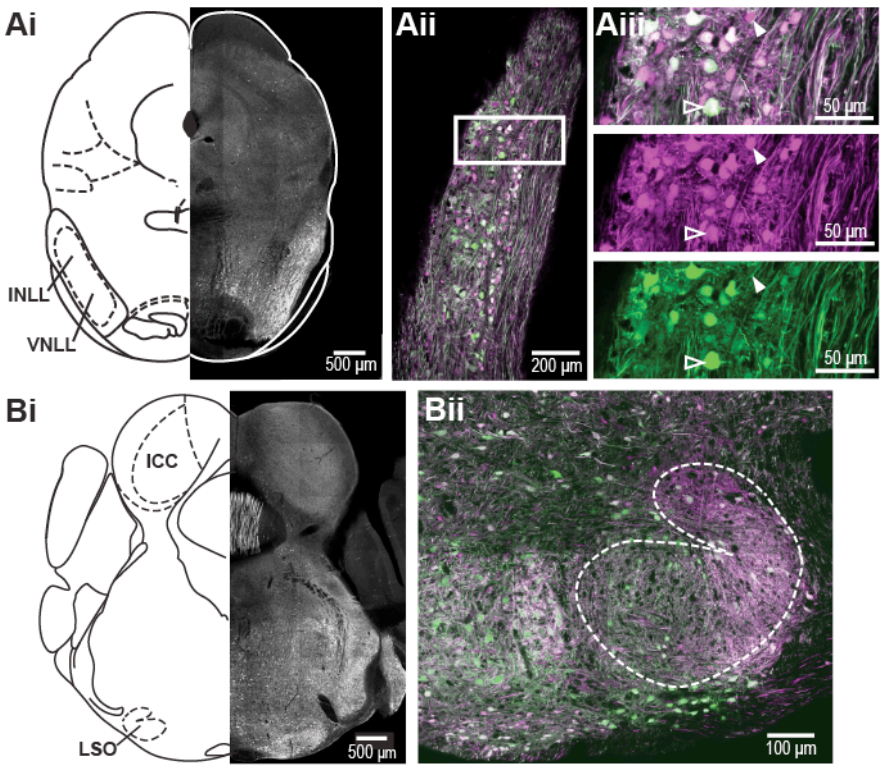

Figure 1.2. Cre expression is limited to GlyT2-expressing neurons in a GlyT2-Cre mouse line. **Ai:** Confocal image (10X tiled image) of a coronal section taken from GlyT2-Cre;tdTomato mouse in which tdTomato is expressed in a Cre-dependent manner. Note that the VNLL has a large number of tdTomato-positive cell bodies (white). Atlas illustration adapted from Paxinos & Franklin 2001. **Aii:** The GlyT2-Cre;tdTomato line was crossed with the GlyT2-EGFP mouse line to confirm the targeted expression of Cre to glycinergic neurons. Displayed is a confocal image (20X tiled image) of a coronal section of VNLL from this cross. **Aiii:** Enlarged section from the VNLL with the red and green channels displayed separately in the bottom two panels. The neuron marked by the solid arrowhead is an example of a Cre/tdTomato-expressing cell that does not express EGFP and therefore may not be glycinergic. The

neuron marked by the arrowhead outline expresses both Cre/tdTomato and EGFP. **Bi:** Confocal image (10X tiled image) of a coronal section containing LSO taken from GlyT2-Cre;tdTomato mouse. Note that the LSO contains a large number of tdTomato-positive cell bodies (white), while the ICC contains only tdTomato-positive fibers. Atlas illustration adapted from Paxinos & Franklin 2001. **Bii:** Enlarged image of the LSO in the GlyT2-Cre;tdTomato line crossed with the GlyT2-EGFP mouse line.

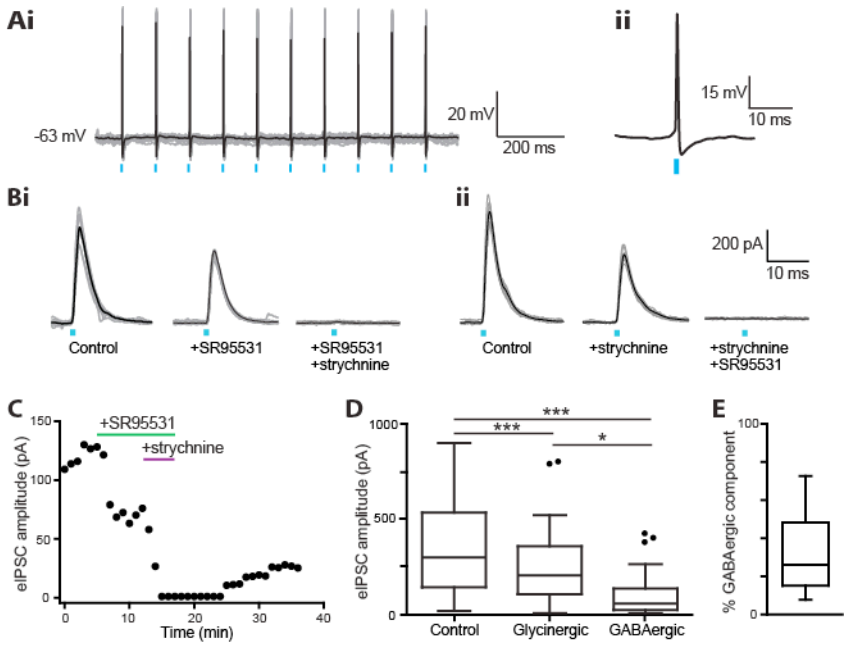

Figure 1.3. Photostimulation of ascending glycinergic fibers to the ICC results in IPSCs with both glycinergic and GABAergic components. **Ai:** Example 10 Hz train of spikes evoked by light in a neuron in VNLL that expresses ChR2. In all figures, gray traces represent individual sweeps while black traces represent the average. **Aii:** Enlarged individual spike. **B:** Example light-evoked IPSCs recorded from two separate neurons in the ICC with bath application of glycine and GABA receptor blockers, strychnine and SR95331. **Bi** shows an example where SR95531 was added first followed by strychnine (n=14 cells) and **Bii** shows the reverse (n=15 cells). This was done to eliminate systematic bias in measuring kinetics of one component solely from subtracted currents. **C:** Light-evoked IPSC amplitude over time from an example cell following bath application of GABAR antagonist SR95531 (5 μM) followed by GlyR antagonist strychnine (500 nM). Due to the fact that strychnine does not easily wash out, the amplitude only shows partially recovery when these drugs are removed. **D:** Summary

data plotting the amplitude of light-evoked IPSCs in control, SR95531, and strychnine. The GABAergic component was significantly smaller than the glycinergic component of the total current (n=29 cells, F=49.72, p<0.0001, Friedman test; *post hoc* control *vs.* glycinergic p<0.0001, control *vs.* GABAergic p<0.0001, glycinergic *vs.* GABAergic p=0.038). *p<0.05, ***p<0.001. **E:** The addition of GABA receptor antagonist SR95531 (5 μM) or glycine receptor antagonist strychnine (500 nM) revealed an average GABAergic component of 31 ± 4% of the evoked currents (n=29 cells).

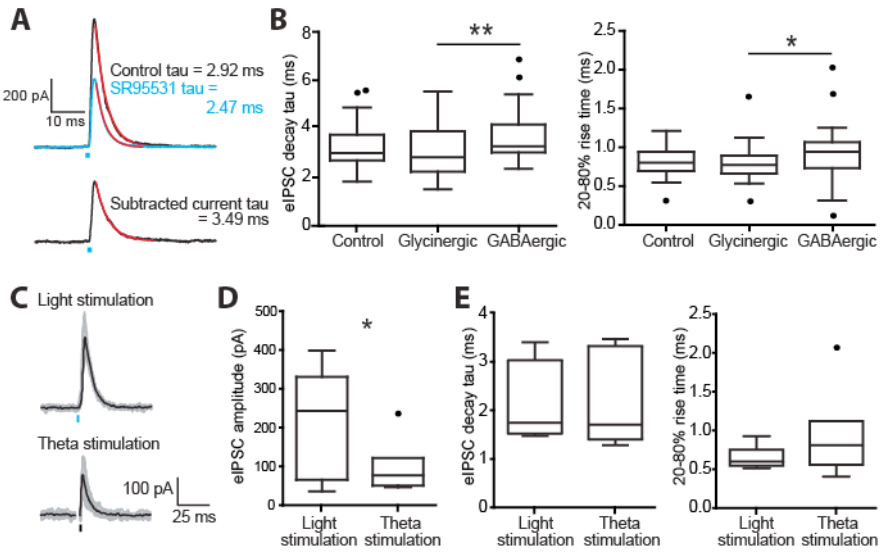

Figure 1.4. Glycinergic and GABAergic components to light-evoked currents had similar kinetics. **A:** Example light-evoked IPSC shown in control conditions (black trace) and in the presence of GABAR antagonist SR95531 (5 μM) to isolate the glycinergic component (blue trace). The lower trace is the GABAergic component generated by subtracting the two currents above. Each of these traces was fitted with a single exponential (red lines) to describe the decay kinetics. **B:** Summary data of measured IPSC decays (upper plot) and rise times (lower plot) for total currents and their glycinergic and GABAergic components. The glycinergic and GABAergic components had strikingly similar kinetics, but the GABAergic decay was significantly slower (n=22 cells, F=11.00, p=0.0041, Friedman test; *post hoc* control *vs.* glycinergic p=0.4074, control *vs.* GABAergic p=0.1752, glycinergic *vs.* GABAergic p=0.0027). Rise time (20-80%) was also significantly slower for the GABAergic component (n=24 cells, F(2,23)=4.79, p= 0.027, repeated measures one-way ANOVA; *post hoc* GABAergic *vs.* glycinergic p=0.039). **C:** Example IPSCs evoked by light (top trace) and theta electrode (bottom trace, stimulus artifacts removed). **D:** Light-evoked IPSCs were about two times

larger in amplitude than theta-evoked IPSCs, indicating that theta-electrode stimulation only activated a portion of the total glycinergic input (n=7 cells, t(6)=2.89, p=0.028, paired two-tailed t-test). **E:** Decay time constants (left plot) and 20-80% rise times (right plot) were not different between light- and theta electrode-evoked IPSCs (time constant: n=7 cells, t(6)=0.11, p=919, paired two-tailed t-test; rise time: n=7 cells, t(6)=1.26, p=0.25, paired two-tailed t-test).

*p<0.05, **p<0.01.

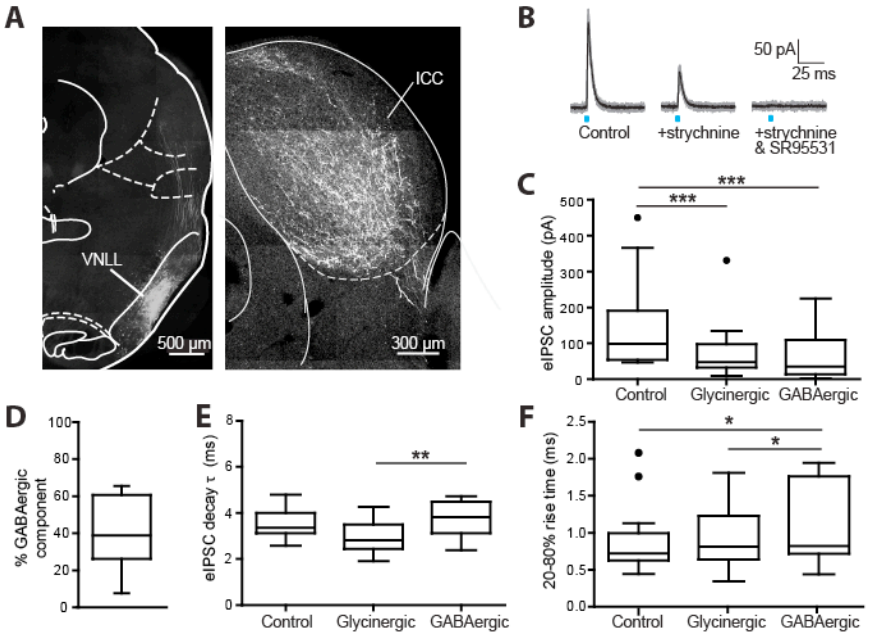

Figure 1.5. Light stimulation of glycinergic fibers ascending from the VNLL. **A:** Confocal images (10X tile) of coronal sections taken from a GlyT2-Cre mouse injected into the VNLL with an AAV (serotype 2/1) to drive expression of ChR2 in a Cre-dependent manner. Left: the injection is well-targeted to the VNLL. Right: Ascending fibers from the VNLL permeate the central nucleus of the IC. Atlas illustrations adapted from Paxinos & Franklin (2001). **B:** Light-evoked IPSCs recorded from a mouse with ChR2 targeted to glycinergic fibers ascending from the VNLL. Similar to photostimulation of global glycinergic input, bath application of GlyR antagonist strychnine results in only partial block of the current, with the remainder blocked by GABAR antagonist SR95531. **C:** Summary data of current amplitudes measured from control conditions, in strychnine (revealing the GABAergic component), and from the subtraction of these two currents (revealing the glycinergic component). The glycinergic (87.2 ± 20.3 pA) and GABAergic (69.5 ± 16.8 pA) components were significantly smaller in amplitude compared to the

IPSCs measured in control conditions (156.5 ± 32.1 pA) (n=15 cells, F=23.3, p<0.001, Friedman test; *post hoc* control vs. glycinergic p<0.001 and control *vs.* GABAergic p<0.001). **D:** The average percentage component of GABA resulting from stimulation of glycinergic afferents from the VNLL was 41.6 ± 4.5% (n=15 cells). **E:** Similar to global stimulation of glycinergic inputs to the IC, the decay of the GABAergic component was slightly but significantly slower than that of the glycinergic component of the IPSC (n=13 cells, F(2,12)=8.09, p=0.0021, repeated measures one-way ANOVA; *post hoc* GABAergic *vs.* glycinergic p=0.0015). **F:** Summary data of 20-80% rise times measured from components of the IPSC. Isolated GABAergic IPSC rise times were slightly but significantly slower (n=13 cells, F=9.39, p=0.0092, Friedman test; *post hoc* GABAergic *vs.* control p=0.0324, GABAergic *vs.* glycinergic p=0.0181).

*p<0.05, **p<0.01, ***p<0.001.

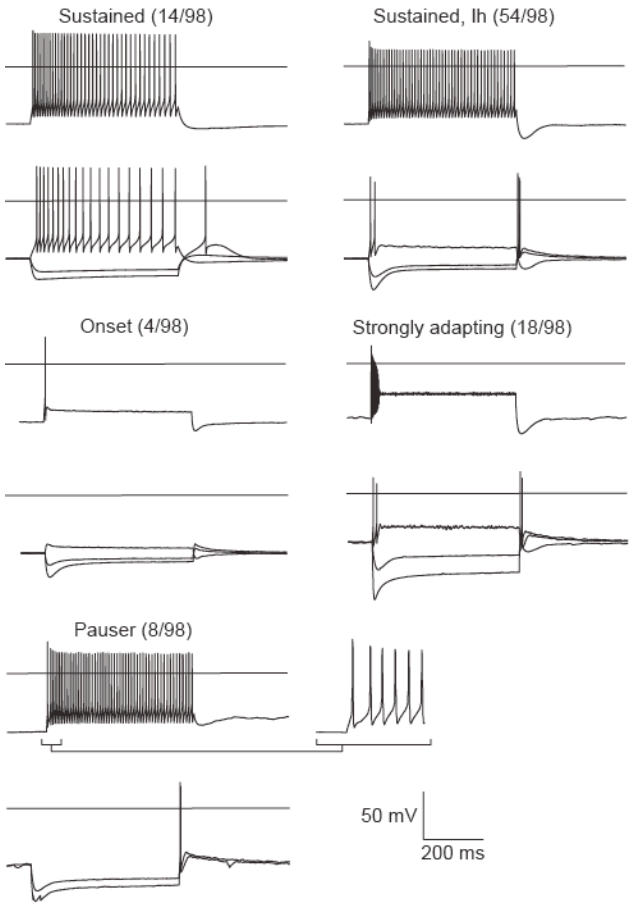

Figure 1.6. Intrinsic properties of neurons in the central nucleus of the IC. Voltage traces displayed for -500, -200, +200, and +500 pA current steps. Firing properties were recorded in a total of 67 neurons, which were categorized into the five subtypes displayed. The *pauser* phenotype is revealed with a pre-hyperpolarizing step (-100 pA). Cells were held at -65 mV. Horizontal axes in traces indicate 0 mV.

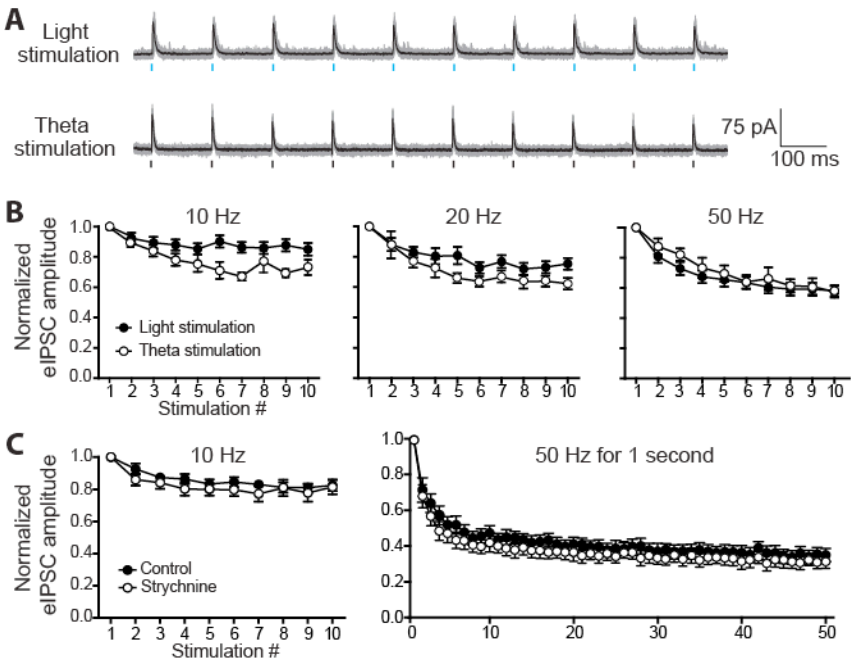

Figure 1.7. Synaptic depression measured from light-evoked IPSCs is comparable to synaptic depression measured from theta electrode-evoked IPSCs up to 50 Hz. **A:** Example traces of light- versus theta electrode-evoked IPSCs (top and bottom traces respectively, stimulus artifacts removed) driven at 10 Hz. Gray indicates individual traces and black is the average. **B:** Summary data of normalized IPSC trains evoked at rates of 10 (left), 20 (middle), and 50 (right) Hz (light $n_{10,20,50\ Hz}$=24, 18, 21 cells; theta $n_{10,20,50\ Hz}$=5, 6, 6 cells; $F_{10,20,\ 50\ Hz}$=2.48, 1.48, 0.25; $df_{10,20,50\ Hz}$=(1,27), (1,22), (1,25); $p_{10,20,50\ Hz}$=0.1267, 0.2375, 0.6208, two-way ANOVAs with repeated measures; 10Hz data showed a significant interaction (p=0.0083), but *post hoc* comparisons were NS). **C:** Normalized amplitudes of light-evoked IPSCs stimulated ten times at 10 Hz (left) and at 50 Hz for 1 second (right) in control conditions and in the presence of strychnine to block the glycinergic component. Neither stimulation frequency revealed a difference in short-term synaptic depression with the addition of strychnine ($n_{10,50Hz}$=9, 10 cells,

$F(1,8)_{10Hz}$=0.68, $F(1,9)_{50Hz}$=3.5, $p_{10,\ 50Hz}$=0.4328, 0.0942, two-way ANOVA with repeated measures on both factors).

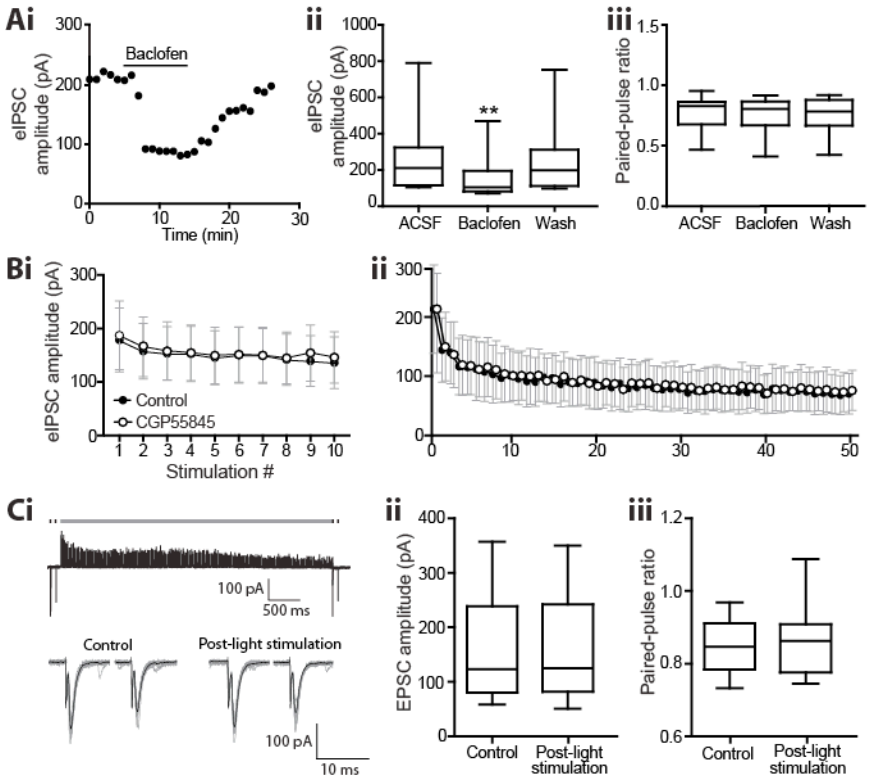

Figure 1.8. Co-released GABA does not act on presynaptic $GABA_B$ receptors of glycinergic or glutamatergic fibers. **A:** Application of $GABA_B$ receptor agonist baclofen depresses release of glycine/GABA from glycinergic terminals. **Ai:** Light-evoked IPSC amplitude over time from an example cell following bath application of baclofen (10 μM). **Aii:** Light-evoked IPSC amplitude is significantly decreased in the presence of baclofen compared to ACSF and wash (n=10 cells, F=11.14, p=0.0012, Friedman test; *post hoc* ACSF *vs.* baclofen p=0.004, baclofen *vs.* wash p=0.005). **Aiii:** Paired-pulse depression of light-evoked IPSCs is unaffected by baclofen (n=10 cells, F(2,9)=1.23, p=0.3157, repeated-measures one-way ANOVA). **B:** Amplitudes of light-evoked IPSCs stimulated ten times at 10 Hz (**Bi**) and at 50 Hz for 5 seconds (**Bii**) in control conditions and CGP55845 (2 μM) to block $GABA_B$Rs. Neither stimulation frequency revealed a

difference in short-term synaptic depression with the addition of CGP55845 (n=5 cells, $F(1,4)_{10,50\ Hz}$=0.007, 2.147, $p_{10,\ 50Hz}$=0.94, 0.22, two-way ANOVA with repeated measures on both factors). **C:** Intense photostimulation of glycinergic fibers does not modify the release probability of glutamatergic terminals. **Ci:** The top trace shows an example where glutamatergic fibers are stimulated with a theta electrode 2 times with 100 ms inter-stimulus interval (black marks) before and after 50 Hz 1 ms light pulses delivered for 1 second (blue marks). The bottom traces show the theta electrode-evoked EPSCs expanded (with individual sweeps shown in gray and the average of the sweeps shown in black; stimulus artifacts truncated for clarity). Intense photostimulation did not affect EPSC amplitude (**Cii**; n=10 cells, t(9)=0.59, p=0.57, paired t-test) or paired-pulse ratio (**Ciii**; n=10 cells, t(9)=1.12, p=0.29, paired t-test).

**p<0.01.

SUBTHRESHOLD OSCILLATIONS AND ELECTRICAL COUPLING IN PRINCIPAL CELLS OF MOUSE DORSAL COCHLEAR NUCLEUS

Moore LA[1,2], Apostolides PF[3], Trussell LO[2]

[1]Neuroscience Graduate Program and [2]Oregon Hearing Research Center and Vollum Institute, Oregon Health & Science University, Portland, Oregon 97239

[3]Kresge Hearing Research Institute & Department of Otolaryngology, University of Michigan, Ann Arbor, Michigan 48109

ABSTRACT

We observed 1-2 Hz oscillations in the membrane potential of fusiform cells, the output neurons of the dorsal cochlear nucleus, in mice of both sexes. Fusiform cells were also resonant at 1-2 Hz and maintained oscillations in the presence of synaptic blockers and in a gap junction KO animal, indicating that oscillations are intrinsically generated. Pharmacology showed that these oscillations were generated by hyperpolarization-activated cyclic nucleotide-gated and persistent Na^+ conductances interacting with passive membrane properties. Oscillations were highly sensitive to external Ca^{2+} concentration and disappeared in concentrations greater than 1.7 mM. We examined the impact of external Ca^{2+} concentration on NaP and HCN conductances and concluded that Ca^{2+} acts specifically on the NaP activation curve to occlude oscillations at higher concentrations. Electrical coupling between fusiform cells allowed oscillations to synchronize. Together, these observations suggest that slow oscillations in DCN may play an important computational role at one of the first stages of auditory processing.

INTRODUCTION

Oscillatory neural activity is found throughout the mammalian brain and is generally proposed to facilitate synchrony and coherent population activity, enable neurons to respond optimally to inputs of a certain frequency, and facilitate synaptic plasticity (Huerta and Lisman, 1995; Hutcheon and Yarom, 2000; Buzsáki and Draguhn, 2004; Lee et al., 2018). EEG recordings reveal that different oscillation frequencies are associated with different states of sensory perception, arousal, and sleep (Buzsáki 2006). These oscillations are observed at the level of local field potentials and individual neuronal membrane potentials (Lagier et al., 2004; Okun et al., 2010). Oscillations are present *in vitro* (Neske, 2016) and, in cortex and thalamus, slow oscillations in particular are associated with deep sleep, quiet wakefulness, and stimulus familiarity (Crochet and Petersen, 2006; Poulet and Petersen, 2008; Gentet et al., 2010; Neske, 2016; Kissinger et al., 2018). Slow oscillations occur in a variety of subcortical regions as well, where they have been proposed to coordinate spike output amongst nonsynchronous synaptic inputs and gate the timing of neural output (Schoppa and Westbrook, 2001; Lefler et al., 2013). However, oscillations have received little attention outside of the thalamocortical regions. Here we present evidence that oscillatory activity is not restricted to higher order brain regions, which has major implications for our understanding of how oscillatory activity may function and propagate in the central nervous system.

In auditory cortex, slow oscillations have been proposed to modulate excitability of the circuit (Lakatos et al., 2005) and amplify sensory inputs (Lakatos et al., 2007). More recent studies in humans show that slow oscillations entrain to subthreshold rhythmic sounds to enable faster detection of sound, therefore serving a predictive

function (ten Oever et al., 2017). In contrast to the auditory cortex, few studies report the presence of spontaneous oscillation in auditory brainstem. The dorsal cochlear nucleus (DCN) is one of the few areas where oscillations have been noted. The DCN is one of the first brainstem regions to receive auditory input. Auditory nerve fibers project to the DCN in a tonotopic fashion, forming a gradient of tonotopic domains in the DCN where higher frequencies are encoded dorsally and lower frequencies are encoded ventrally (Muniak et al., 2013). The output neurons, fusiform cells, generate 40-100 Hz oscillations during the slow depolarization that precedes spiking in subtypes that display a pauser or buildup response to current injection (Manis et al., 2003). These oscillations appear to facilitate temporally precise spike generation.

Although DCN neurons are adapted to transmitting rapid auditory signals, we found that fusiform cells produce highly regular, 1-2 Hz membrane potential oscillations in acute brainstem slices. Pharmacology revealed that these oscillations are generated by the interplay of two ionic conductances, the hyperpolarization and cyclic nucleotide gated channels (HCN) and tetrodotoxin-sensitive Na^+ channels. The oscillations were sensitive to external Ca^{2+} concentration over the range used in standard *in vitro* slice studies, and disappear in concentrations greater than 1.7 mM. Finally, due to the weak electrical coupling between fusiform cells, oscillations were synchronized between neurons, and this coupling and synchrony appeared to be confined to fusiform cells within single tonotopic domains.

METHODS

Animals

All animal procedures were approved by Oregon Health & Science University's Institutional Animal Care and Use Committee. Mice of post-natal days 16-25 were used from WT *C57BL/6*, heterozygous GlyT2-EGFP (*FVB.Cg- Tg(Slc6a5-EGFP)13Uze/UzeBsiRbrc*, RRID:IMSR_RBRC04708; Zeilhofer et al. 2005), Thy1-YFP (*B6;CBA-Tg(Thy1-YFP)GJrs/GfngJ*, RRID:IMSR_JAX:014130; Feng et al. 2000), and connexin36 KO (Hormuzdi et al., 2001) of both sexes. Fusiform cells are easily identifiable in slice preparations by their morphology and input resistance, but the latter two genetic lines were used to more efficiently visualize deeper cells and distinguish from other cell types. Specifically, the Thy1-YFP line labeled fusiform cells, while the GlyT2-EGFP line allowed us to avoid the extremely numerous glycinergic interneurons of DCN. No differences were observed in the properties of fusiform cells among these different mouse lines.

Brain-slice preparation

Mice were decapitated under deep isoflurane anesthesia. Coronal slices (300 μm) were cut on a vibratome (Leica VT1200S and Campden Instruments 7000smz-2). Slices containing DCN were cut at a 30° ventral-dorsal angle (to preserve electrical coupling of fusiform cells) in warm (~35°C) ACSF. We were unsuccessful in finding electrically coupled fusiform cell pairs when slices were cut in the sagittal plane (n=11 dual recordings). ACSF contained (in mM) 130 NaCl, 2.1 KCl, 1.2 KH_2PO_4, 1.7 $CaCl_2$, 1 $MgSO_4$, 20 $NaHCO_3$, 3 Na-HEPES, 10-12 glucose, 2 Na-pyruvate, and 10 μM MK-801

and was bubbled with 5% CO_2/95% O_2 (300-310 mOsm). Slices recovered for 30 min at 34°C and were then kept at room temperature until use.

Electrophysiology

Slices containing DCN were held in a chamber perfused with ACSF at a rate of 2-3 ml/min and heated to 30-33°C with an in-line heater. Neurons were visualized with Dodt contrast optics using a 40X objective on an upright microscope (Zeiss Axioskop2). The Multiclamp 700B amplifier was used to obtain whole-cell patch clamp recordings from fusiform cells. Data were filtered at 10 kHz, digitized at 20 kHz with a Digidata 1322A, and acquired with pClamp 10.4 software (Molecular Devices, RRID:SCR_011323). Oscillations were recorded in the presence of synaptic blockers to reduce signal noise and optimize cross-correlation analysis, including 5 μM NBQX, 10 μM MK-801, 1 μM strychnine, and 5 μM SR-95531.

For experiments in which the bath Ca^{2+} concentration was varied, the total concentration of divalents was held constant at 2.7 mM by addition of Mg^{2+} to the ACSF. ACSF of each Ca^{2+} concentration contained (in mM) 130 NaCl, 3 Na-HEPES, 20 $NaHCO_3$, ~7 glucose, 0.05 $NiCl_2$, 0.05 $CdCl_2$, 0.4 ascorbate, and 2 Na-pyruvate. KH_2PO_4 was replaced with KCl to prevent precipitation of calcium (Kim and Trussell, 2007). ACSF of varying Ca^{2+} concentrations were mixed from stock solutions containing either 2.6 mM Mg^{2+} or 2.6 mM Ca^{2+}. The Mg^{2+} stock solution contained, along with the above, 1 $MgSO_4$, 1.6 $MgCl_2$, and 3.3 KCl and the Ca^{2+} stock solution contained 2.6 $CaCl_2$, 1 K_2SO_4, and 1.3 KCl. HCN conductance in varying concentrations of Ca^{2+} was measured in a total divalent concentration of 2.8 mM in order to include 0.2 $BaCl_2$.

The majority of experiments were performed with a K-gluconate internal pipette solution containing, in mM: 113 K-gluconate, 4.5 $MgCl_2$, 0.1 EGTA, 9 HEPES, 14 tris-phosphocreatine, 4 Na_2-ATP, 0.3 tris-GTP, with pH adjusted to 7.25 with KOH and osmolality adjusted to 290 mOsm with sucrose. Holding potentials reported here were adjusted for a junction potential of -13 mV. A Cs-TEA internal was used to measure NaP channel conductance. This internal contained (in mM) 115 TEA-Cl, 4.5 $MgCl_2$, 3.5 CsCl, 10 EGTA, 10 HEPES, 4 Na_2-ATP, 0.5 tris-GTP, 5 CsOH to adjust pH to 7.25, and 15 sucrose to adjust osmolality to 290 mOsm. Results from experiments using this solution were corrected for a junction potential of -3 mV. Recording electrodes of 4-6 MΩ were pulled from borosilicate glass (WPI 1B150F-4) with a vertical puller (Narishige P-10). For voltage-clamp recordings, series resistance (<20 MΩ) was compensated by 60-80% correction and 90% prediction with the Multiclamp (bandwidth 3 kHz). Data were only included for final analysis if the series resistance changed by <20% over the course of the experiment. Reagents were purchased from Sigma-Aldrich.

Frequency-domain analysis

The power spectrum for spontaneous oscillations (binned at 0.1-0.2 Hz) was generated from 20-30 s segments of representative traces using a Hamming window 50% overlap of spectral segments. The resonant frequency of neurons was determined by injecting a 5 pA swept sine wave (ZAP, or impedance (*Z*) amplitude profile) current that varied in frequency from 0 to 10 Hz over 20 sec (Puil et al., 1986). Neurons were injected with negative bias current to prevent spiking during the ZAP current injection and spontaneous oscillation frequency and power were measured at this same holding potential. The amplitude of the ZAP was determined by the minimal amount of current

injection that would result in a detectable voltage deflection without eliciting spikes. Impedance (Z) was calculated from the ratio of the fast Fourier transforms of the injected current (I) and measured voltage response (V):

$$Z = \frac{FFT(I)}{FFT(V)}$$

The resulting impedance measurement, *Z*, is a complex number with real and imaginary components. When these components are plotted as x and y, the distance from the origin to the Z point represents the absolute value of Z. We use this absolute value for impedance measurements (Beatty et al., 2015; Stagkourakis et al., 2018).

For a resonant neuron, the resulting impedance curve displays a peak in impedance at the resonant frequency. The strength of this peak is quantified by the Q value, which is the peak impedance value divided by the impedance value measured at the lowest frequency (Koch, 1984).

Conductance measurements

To measure NaP activation, a ramp was delivered to the neuron from -80 to -50 mV over the course of 5 seconds (Leao et al., 2012). 1-10 nM TTX was included in the bath to help suppress escaping spikes and therefore enable current measurements at more depolarized potentials. The first ~2 seconds of the response was dominated by a linear outward current reflecting the passive membrane response to the voltage ramp. We fit this with a line and subtracted the linear values from the current response to perform leak subtraction. Conductance (*G*) was then calculated according to the

following equation, where *I* is current measured at a given voltage (*V*), and *Vrev* is the reversal potential of Na^+ (which was calculated to be 77.4 mV):

$$G = \frac{I}{(V - Vrev)}$$

HCN activation in different external Ca^{2+} concentrations was measured similar to Tang & Trussell 2015. Cells were held at -60 mV and delivered 5-second steps from -120 mV to -60 mV in 5 mV increments. After each 5 second step, the cell was brought back to -60 mV, resulting in a tail current from which HCN activation could be approximated. Cd^{2+}/Ni^{2+} (50 µM each) were included in the bath to control for changes in Ca^{2+} concentration. Ba^{2+} (200 µM) and 4-aminopyridine (4AP) (1 mM) were also included to reduce contamination in the tail current from leak conductance and low-voltage activated K channels respectively (Johnston et al., 2010; Leao et al., 2012). Both drugs block HCN channels, but were used at concentrations to minimize this effect (Ludwig et al., 1998).

The resulting NaP and HCN activation curves were fit with a Boltzmann equation:

$$y = base + \frac{(max - base)}{1 + exp\left(\frac{v50 - x}{slope}\right)}$$

The *base* value was set to 0. The other resulting values, *max* (maximum conductance), *v50* (half-activation voltage of the curve), and *slope* (a value that describes the steepness of the sigmoid) were compared for each cell between different external Ca^{2+}

concentrations. The population conductance curves for NaP and HCN were generated by normalizing raw conductance values for each cell to the *max* value given by the Boltzmann fit. These average values were then fit with their own Boltzmann equation.

Paired recordings and cross-correlation analysis

The coupling coefficient for electrically coupled fusiform cells was determined by holding both cells in current clamp and alternating injection of a -1 nA square pulse into each cell. Coupling coefficient was calculated by dividing the amplitude of the voltage deflection in the post-junctional cell by the amplitude of the voltage deflection in the pre-junctional cell. Pairs were considered to be coupled if the coupling coefficient was greater than 0.005 (Yaeger and Trussell, 2016).

For cross-correlation analysis for cell pairs, 1-2 min segments of subthreshold traces with a steady baseline were selected. Traces were resampled from 50 to 200 μs inter-sample-interval, bandpass filtered at 0.2-10 Hz, and baseline-subtracted. Cross-correlograms were generated in Igor and normalized by dividing cross-correlation coefficient values (xcorr) by the standard deviation (sd) of each trace multiplied together:

$$\text{normalized xcorr}(t) = \frac{\text{xcorr}(t)}{\text{sd}\big(\text{A}(t')\big) * \text{sd}(\text{B}(t'))}$$

where xcorr(t) is the raw cross-correlation coefficient calculated for a given lag time t, and A(t') and B(t') are the voltage traces with t' representing the time variable for the traces. In this way, if the analysis were an autocorrelation, variance would be the normalization factor and the value at time zero would be 1 (Beierlein et al., 2000).

For spike cross-correlation, spikes were detected using threshold search in pClamp, generating a list of spike times for each cell. Spike times were binned in 1 and 10 ms segments and cross-correlated in Igor. Resulting cross-correlation coefficients (xcorr) were then adjusted and normalized according to the following equation:

$$\text{normalized xcorr}(t) = \frac{\text{xcorr}(t) - \text{scrambled}}{\sqrt{n_A * n_B}}$$

where n_A and n_B are spike counts from traces A and B. The *scrambled* term is the average cross-correlation coefficient value from cross correlating spikes from trace A with scrambled spike times from trace B, generated using the *random.shuffle* function in Python. This is used in place of the theoretically calculated term used by others (Eggermont, 1992; Stefanescu and Shore, 2015). In the text, both oscillation and spike time cross-correlation coefficient values are referred to as *xcorr* for simplicity. Peak *xcorr* values reported are measured at zero lag instead of the real peak.

Experimental design and statistical analysis

Electrophysiological traces were analyzed with pClamp 10.4 software or custom-written procedures in IGOR Pro 6.3 (RRID:SCR_000325) and Python 2.6 (RRID:SCR008394). GraphPad Prism 7 (RRID:SCR002798) was used for statistical analysis and to make figures. Data are represented in the text and figures as mean ± SEM. Parametric analysis was used only after confirming assumptions of equal variances (Bartlett's test) and normality (D'Agostino-Pearson omnibus normality test). The equivalent non-parametric tests were used when data were not normal; the name of the test used is included with all statistics reported in the *Results* section. One-way

ANOVA with repeated measures (RM) was used to compare statistics for single cells across more than two conditions, followed by Tukey's *post hoc* comparisons (p values associated with post hoc tests are only reported when the main effect is significant). The Geisser and Greenhouse correction was applied to RM one-way ANOVAs to correct for possible violations of the assumption of sphericity (of note, this frequently changes associated DF values to non-integers). Assumptions of sphericity and effective matching were also confirmed for one-way ANOVAs.

RESULTS

Fusiform cells oscillate at rest

Approximately 80% of fusiform cells patched displayed 1-2 Hz subthreshold oscillations around the resting membrane potential in the absence of ongoing spike activity (Fig. 2.1A). Power spectrum analysis of the oscillations revealed a clear peak in this range, averaging 1.12 ± 0.03 Hz over the population (n=117 cells; Fig. 2.1B,E). Oscillation power was strongly voltage-dependent, indicating the involvement of voltage-sensitive channels (Fig. 2.1C; n= 10 cells). Oscillations were typically recorded in the presence of blockers of fast synaptic transmission (see Methods), but were also clearly present in the absence of synaptic blockers (Fig. 1D). Synaptic blockers did not affect oscillation frequency (Fig. 2.1E; 1.33 ± 0.12 Hz without blockers, n=15 cells, U=616, p=0.06, Mann-Whitney U). However, oscillation power in the presence of blockers (3.7 ± 0.5 mV/Hz^2) versus without (0.8 ± 0.2 mV/Hz^2) was significantly higher (Fig. 2.1F; U=462, p=0.002, Mann-Whitney U), likely due to increased channel opening that reduces membrane resistance and changes the effect of oscillation conductances on membrane voltage. These results show that rather than having a static resting

membrane potential, the excitability of DCN output neurons dynamically oscillates in a moment-to-moment fashion.

Fusiform cells show slow intrinsic resonance

The resonant frequency of a neuron is the frequency at which a sinusoidal current injection will produce the maximal voltage response. Voltage-gated ionic conductances and passive membrane properties interact to result in this peak response. Resonant frequency is measured by injecting current of constant amplitude that varies in frequency (a "ZAP") and measuring the resulting voltage (Fig. 2.2A, Puil et al. 1986). An impedance value can be calculated for each frequency by dividing the fast Fourier transforms of the current and voltage measurements (Hutcheon et al., 1996). The resonant frequency is revealed as a peak in the resulting impedance curve (Fig. 2.2A). The presence of a resonant peak is quantified by the Q value, which is the impedance measurement at the resonant frequency divided by the impedance measured at the lowest recorded frequency (Koch, 1984). A non-resonant neuron will have a Q value equal to or less than 1. All fusiform cells measured had a Q value greater than 1, with an average value of 3.8 ± 0.4 (n=21 cells; Fig. 2.2B).

Fusiform cells displayed resonance near their resting potentials. All cells displayed resonance of similar frequency even though only a portion of them displayed spontaneous oscillations. Spontaneous oscillators and non-oscillators were resonant at 1.0 ± 0.1 Hz (n=14 cells) and 1.1 ± 0.1 Hz, respectively (n=7 cells, $t(19)=0.9$, $p=0.399$, two-tailed t-test; Fig. 2.2C). There was no difference in the membrane potential at which impedance measurements were made between these groups (-75.7 ± 0.7 mV oscillators, -76.8 ± 1.6 mV non-oscillators, $t(19)=0.757$, $p=0.459$, two-tailed t-test). The

resonant frequency of oscillating cells was similar to the frequency of their spontaneous oscillations (Fig. 2.2D; 1.0 ± 0.1 Hz, n=14 cells, t(13)=0.679, p=0.509, paired two-tailed t-test). These results suggest that the oscillatory frequency of fusiform cells is likely dictated by their intrinsic and ionic properties rather than being set by circuit-level mechanisms as is generally accepted from the cortical literature.

NaP and HCN conductances are required for oscillations

Previous studies show that oscillations can be generated by interactions between voltage- or Ca^{2+}-sensitive conductances and passive properties of the membrane. For example, in the thalamus oscillations are famously generated by T-type Ca^{2+} conductance (Steriade et al., 1993; Hughes et al., 2002). Surprisingly, we found that oscillations in fusiform cells persisted in the presence of Ca^{2+} channel blockers: addition of broad-spectrum Ca^{2+} channel blockers 100 µM Cd^{2+} and 50 µM Ni^{2+} resulted in a slight but non-significant increase in oscillation power (Fig. 2.3D; control 3.9 ± 1.5 mV/Hz^2, Cd^{2+}/Ni^{2+} 7.2 ± 2.6 mV/Hz^2, wash 4.6 ± 1.6 mV/Hz^2; n=6 cells, F(1.6,7.9)=4.64, p=0.052, RM one-way ANOVA). Ni^{2+} also blocks NMDA receptors and therefore rules out the involvement of this conductance as well (Mayer and Westbrook, 1985). These results show that oscillations in fusiform cells are surprisingly generated by mechanisms distinct from those classically seen in other intrinsically resonant neurons.

By contrast, addition of 500 nM TTX fully blocked oscillations, indicating a critical role for Na^+ channels in mediating this phenomenon (Fig. 2.3A; control 6.1 ± 4.3 mV/Hz^2, TTX undetectable, wash 4.6 ± 3.4 mV/Hz^2; n=7 cells, W=11.14, p=0.0012, Friedman test). Bath application of the HCN channel blocker Cs^+ (1-2 mM) similarly attenuated oscillation power (Fig. 2.3B; control 5.7 ± 1.8 mV/Hz^2, Cs^+ 0.2 ± 0.1 mV/Hz^2,

wash 4.6 ± 1.4 mV/Hz^2; n=10 cells, F(1.2, 10.8)=8.7, p=0.01, RM one-way ANOVA). In a separate set of experiments, ZD7288 (10 mM) was applied to confirm the role of HCN channels in oscillations. ZD7288 had matching effects to Cs^+ (control 8.0 ± 3.9 mV/Hz^2, ZD 0.4 ± 0.03 mV/Hz^2; n=6 cells, W=-21, p=0.03, Friedman test).

We also tested for the involvement of K^+ channels. The non-specific K^+ channel blocker TEA (10 mM) significantly increased oscillation power from 2.5 ± 1.9 to 13.7 ± 9.8 mV/Hz^2 (Fig. 2.3C; wash 2.0 ± 1.5 Hz/mV^2; n=7 cells, F=12.29, p=0.0003, Friedman test). This is likely due to increased input resistance. Altogether these results put forth a model whereby oscillations are generated by the interplay between NaP and HCN channels, whereas K^+ channels negatively regulate the power of the oscillations.

External Ca^{2+} concentration determines the strength of oscillations

The presence of oscillations was surprising given that they had not been reported despite decades of studies of fusiform cells *in vitro* (Gardner et al., 2001; Fujino and Oertel, 2003; Manis et al., 2003; Tzounopoulos et al., 2004). However, most previous studies of fusiform cells used an external Ca^{2+} concentration of 2.4-2.5 mM (Gardner et al., 2001; Fujino and Oertel, 2003; Manis et al., 2003; Tzounopoulos et al., 2004). Our experiments thus far used 1.7 mM Ca^{2+}, which is much closer to the external Ca^{2+} concentration of CSF *in vivo* (Somjen 2004; Borst, 2010). Might differences in external Ca^{2+} explain why other studies did not report oscillations in fusiform cells? We tested this by systematically determining the relation between oscillation power and Ca^{2+}. Oscillation strength showed a remarkably steep dose-dependence on Ca^{2+} concentration, decreasing to undetectable levels above 2 mM Ca^{2+}, with a half-maximal power at 1 mM (Fig. 2.4A-B, n=8 cells). Though 1.7 and 2.5 mM are on the tail-end of

the dose-response curve, there is a four-fold difference between power measurements in these two concentrations.

The experiments described above highlighted the critical role of Na^+ and HCN channels in the genesis of the oscillations. Since TEA, Ni^{2+}, or Cd^{2+} did not inhibit oscillations, it was unlikely that Ca^{2+} currents or Ca^{2+}-dependent K^+ currents contributed to the effects of changes in bath Ca^{2+} levels that we observed. However, certain studies show that external Ca^{2+} concentration regulates the voltage sensitivity of Na^+ channels, with lower concentrations causing a negative shift in the half-activation voltage (Frankenhaeuser and Hodgkin, 1957; Campbell and Hille, 1976). If high Ca^{2+} concentration has a similar effect on Na^+ channels in fusiform cells, the lower Na^+ conductance could presumably inhibit the cells from oscillating.

We therefore tested whether changes in Ca^{2+} concentration over the range that modulates oscillation strength would also affect Na^+ current. NaP conductance was measured in voltage clamp by gradually ramping membrane potential from -80 to -50 mV over the course of 5 seconds (Fig. 2.4C; Leao et al. 2012). Voltage control was maintained by limiting Na^+ current amplitude with TTX, blocking background currents, and using a narrow range of voltages (see *Methods*). Half-maximal activation voltage (*v50*) displayed a significant positive shift in higher Ca^{2+} concentrations (Fig. 2.4E center panel; n=9 cells, $F(1.7, 13.3) = 31.07$, $p<0.0001$, RM one-way ANOVA): *v50* increased from -61.2 ± 1.0 mV in 0.5 mM to -56.5 ± 1.0 mV in 1.7 mM ($p<0.0001$) and -56.9 ± 1.3 mV in 2.5 mM ($p=0.001$). However, *v50* was not measurably different between 1.7 and 2.5 mM conditions ($p=0.851$). Maximum conductance, as predicted by the Boltzmann fits, was not different between conditions, averaging 3.1 ± 0.7, 3.6 ± 0.8,

and 2.7 ± 0.7 nS from low to high concentration (Fig. 2.4E left panel; n=9 cells, F(1.2, 9.9)=1.6, p=0.239, RM one-way ANOVA). Slope was also unchanged between all conditions, averaging 3.0 ± 0.2, 3.2 ± 0.2, and 3.0 ± 0.2 nS/mV in 0.5, 1.7, and 2.5 mM Ca^{2+} (Fig. 2.4E right panel; n=9 cells, F(1.1, 9.0)=0.514, p=0.514, RM one-way ANOVA). Higher external Ca^{2+} concentration may therefore effectively decrease NaP conductance to inhibit oscillations by positively shifting the half-maximal activation voltage of the channels.

We also tested for possible effects of Ca^{2+} concentration on HCN conductance (Fig. 2.5A,B). Ca^{2+} concentration did not affect the maximum HCN tail current (Fig. 2.5C; average(0.5, 1.7, 2.5 mM Ca^{2+})=245.0 ± 21.5, 254.1 ± 23.8, 265.7 ± 19.7 pA, n=11 cells, F(1.9,19.5)=1.61, p=0.225, RM one-way ANOVA), or the parameters of the Boltzmann equation, including *v50* (Fig. 2.5C; average(0.5, 1.7, 2.5 mM Ca^{2+})=-92.8 ± 1.4, -92.8 ± 1.2, -92.2 ± 1.4 mV, n=11 cells, F(1.6, 15.9)=0.18, p=0.791, RM one-way ANOVA) and slope (Fig. 2.5C; average(0.5, 1.7, 2.5 mM Ca^{2+})=-7.6 ± 0.3, -7.5 ± 0.4, -7.5 ± 0.7 pA/mV, n=11 cells, F(1.4, 14.3)=0.03, p=0.929, RM one-way ANOVA). These results indicate that external Ca^{2+} likely acts specifically on NaP, and explains why other labs didn't see this phenomenon.

Electrical coupling and oscillation synchrony

Fusiform cells are electrically coupled via gap junctions. Although the probability of proximal fusiform cells being electrically coupled is high (around 70% reported from 20/28 pairs), the strength of coupling is low (0.01; Apostolides & Trussell 2013). Interestingly, paired recordings from fusiform cells revealed strong oscillation synchrony between neurons despite this apparent weak coupling. Cross-correlograms obtained

from correlating the two voltage signals of electrically coupled pairs displayed a peak close to zero lag (Fig. 2.6A). To determine whether the oscillation synchrony was indeed due to electrical coupling, we made dual recordings from Cx36 KO animals in which electrical coupling in DCN is abolished (Apostolides and Trussell, 2013b; Yaeger and Trussell, 2016). Interestingly, though fusiform cells from Cx36 KO tissue still display oscillations, there was no longer synchrony between closely apposed fusiform cells (Fig. 2.6B). Population statistics are displayed in Figure 6C. The average *xcorr* for coupled pairs was 0.5 ± 0.05 (n=26 pairs). This was significantly larger than *xcorr* values for uncoupled pairs in WT and Cx36 KO tissue, both of which exhibited *xcorr* values close to zero (Fig. 2.6C left; 0.01 ± 0.01 (n=13 pairs) for uncoupled WT and -0.01 ± 0.02 (n=10 pairs) for KO; $F(2,46)=49.6$, $p<0.0001$, one-way ANOVA; post hoc WT *vs.* WT uncoupled $p<0.0001$, WT *vs.* Cx36 KO $p<0.0001$). Coupled pairs in WT tissue displayed peaks in their crosscorrelograms close to zero lag, averaging 10.5 ± 1.8 ms (Fig 2.6C right). These results indicate that fusiform cell oscillations are generated by cell intrinsic conductances whereas the presence of electrical synapses allows synchrony across the neuronal population.

The oscillations observed in Cx36 KO mice had significantly lower power than oscillations recorded from WT (Fig. 2.6D; averages WT 3.7 ± 0.5 mV/Hz^2 (n=117 cells), KO 0.9 ± 0.3 mV/Hz^2 (n=19 cells); U=405, $p<0.0001$, Mann-Whitney U). Frequency, however, was unchanged (Fig. 2.6D; averages WT 1.12 ± 0.03 Hz (n=117 cells), KO 1.32 ± 0.12 Hz (n=19 cells); U=846, $p=0.096$, Mann-Whitney U). This indicates that electrical coupling contributes to oscillation power.

Electrical coupling and spike synchrony

The presence of synchrony in subthreshold voltage oscillations might lead to spike synchrony between fusiform cells (Stefanescu and Shore, 2015, 2017). To test this, spike times were binned at both 1 and 10 ms and used to generate cross-correlograms of spike times. Electrically coupled neurons typically show robust spike synchrony, with synchronized spikes occurring within 5 ms of one another (Dugué et al., 2009; Trenholm et al., 2014). In contrast, fusiform pairs showed no evidence of such fine-scale synchrony (Fig. 2.7A inset), perhaps due to their relatively weak coupling. However, in pairs where both neurons were bursting (Fig. 2.7A) or oscillating (Fig. 2.7B), the resulting cross-correlograms displayed 1-2 Hz oscillations similar to those seen in the voltage cross-correlograms. The average *xcorr* for bursting pairs was 0.22 ± 0.06 (Fig. 2.7C; n=6 pairs). The oscillations in the cross-correlograms of oscillating pairs were much weaker, resulting in *xcorr* values close to zero (Fig. 2.7C; oscillating 0.02 ± 0.01, n=6 pairs). The lag time of the peak of these xcorr oscillations was similar to lag times measured when correlating oscillating membrane potential, averaging 57.3 ± 12.4 ms (n=11 pairs). Cross-correlation waveforms for both bursting and oscillating pairs showed an average cycle width of 1012 ± 65 ms (n=11 pairs), matching the subthreshold voltage oscillations of the cells. For each bursting pair, we measured the spike frequency for each cell and averaged them to get the pair spike frequency. We saw a strong positive linear correlation between spike *xcorr* and spike frequency (Fig. 2.7D; n=12 pairs, R^2=0.86, p<0.0001, linear regression). Increased spike frequency in bursting pairs may therefore increase broad-scale spike synchrony.

Electrical coupling, synchrony, and distance

The distance between somas was approximated for a subset of dual recordings. With the exception of one pair with a distance of 120 μm between cells, all electrically coupled pairs fell within 80 μm of one another (n=9 pairs). There was no significant linear relationship between distance and coupling coefficient (n=20 pairs, R^2=0.15, p=0.097, linear regression) or oscillation synchrony (n=17 pairs, R^2=0.19, p=0.119, linear regression). Considering the highly detailed mapping of mouse DCN tonotopy (Muniak et al., 2013) and the relatively conserved region in which pairs were made, it is likely that only fusiform cells within the same or similar tonotopic domains were connected.

DISCUSSION

Oscillations & resonance properties

Our results show that fusiform cells of the DCN display slow 1-2 Hz oscillations when at rest. Given that the oscillations are still present in the absence of synaptic blockers and that the intrinsic resonance frequency is also 1-2 Hz, the oscillation frequency is likely set by the intrinsic resonance of these cells (Fransén et al., 2004). Resonance is created by active and passive properties that filter low- and high-frequency voltage fluctuations, resulting in a bandpass peak in the impedance curve (Hutcheon and Yarom, 2000). The passive membrane properties of neurons filter out high-frequency voltage fluctuations while slow-activating conductances damp low-frequency voltage fluctuations. It therefore appears that the intrinsic resonance sets the frequency of oscillations in the DCN, similar to what has been shown in the neocortex and hippocampus (Chen et al., 2016).

Fusiform cells require both HCN and NaP to produce steady oscillations. These conductances are known to underlie oscillations in other brain regions, including stellate cells of the entorhinal cortex, neuroendocrine tuberoinfundibular dopamine neurons, principal cells of the inferior olive, thalamic relay neurons, CA1 hippocampal pyramidal neurons, and strial cholinergic neurons, among others (Mccormick and Pape, 1990; Fransén et al., 2004; Wilson, 2005; Hu et al., 2009; Boehlen et al., 2013; Matsumoto-Makidono et al., 2016; Stagkourakis et al., 2018). Electrical connections also boosted the power of oscillations (Fig. 6B). This may be because electrically connected neurons effectively inherit some portion of the NaP and HCN conductances of connected cells (Apostolides and Trussell, 2014). Modeling studies in other regions show that NaP conductance increases during the depolarizing phase of the oscillations while HCN conductance increases during the hyperpolarizing phase (Dickson et al., 2000; Fransén et al., 2004). This likely describes the dynamic interplay of voltage-dependent activation and deactivation occurring in fusiform cells as well.

Other blockers had variable effects on oscillations. Ca^{2+} channels are required for spontaneous oscillations in inferior olive (Llinás and Yarom, 1981; Matsumoto-Makidono et al., 2016), but did not appear to contribute to slow fusiform oscillations. TEA caused an increase in oscillation power, perhaps by enhancing cell input resistance or depolarizing and increasing oscillation amplitude in the dendrites that couldn't be effectively clamped. 10 mM TEA blocks low- and high-threshold K^+ channels as well as KCNQ channels that underlie M-type K^+ current (Johnston et al., 2010). These K^+ channels therefore do not appear to be involved in generating oscillations.

Effect of external Ca^{2+}

Ca^{2+} concentration had a large effect on oscillation power: low Ca^{2+} (0.5 mM) caused oscillations to become much larger in amplitude compared to control (1.7 mM) whereas high Ca^{2+} (2.5-5 mM) blocked oscillations. This may explain why previous studies in DCN that used a standard 2.5 mM Ca^{2+} concentration (and total divalent concentrations of ~3.7 mM) have not noted the presence of oscillations (Gardner et al., 2001; Fujino and Oertel, 2003; Manis et al., 2003; Tzounopoulos et al., 2004). Olsen et al. (2018) used 2 mM external Ca^{2+} and also did not note oscillations. Lowering external divalent concentrations has been shown to reveal oscillations in other brain regions as well. For example, Sanchez-Vives & McCormick (2000) observed the emergence of slow oscillations *in vitro* matching those observed *in vivo* when they lowered external divalent concentrations in slice to concentrations closer to those reported *in vivo* (specifically from 2 to 1 mM Mg^{2+} and from 2 to 1.2 mM Ca^{2+}). Divalent ions have a charge screening effect on neuronal membranes such that higher divalent concentrations make it harder for voltage-gated channels to "sense" a change in voltage. This results in a positive shift in the activation curves of voltage-sensitive conductances and may explain why previous in vitro studies see oscillations in lower external divalent concentrations (Frankenhaeuser and Hodgkin, 1957; McLaughlin et al., 1971; Campbell and Hille, 1976).

We attribute the effect of external Ca^{2+} concentration on oscillation power to specific action of Ca^{2+} on Na^{+} channels (Campbell and Hille, 1976). High external Ca^{2+} induced a significant positive shift in the voltage range of activation for NaP. Because we held total divalent concentration constant, this observation cannot be purely

explained by general divalent charge screening, unless of course Ca^{2+} is more effective at screening Na^{+} channels than Mg^{2+} is (Horn, 1999). It is perhaps unsurprising that we did not see a difference in *v50* between 1.7 and 2.5 mM Ca^{2+} as the relationship between Ca^{2+} and *v50* is highly non-linear (Campbell, 1976). It may be that our experimental setup was not sensitive enough to detect relatively smaller effects of Ca^{2+} concentration on Na^{+} channels that still effectively move the cell further towards the tail-end of the dose-response curve. Ultimately, our results suggest that that the impact of external Ca^{2+} concentration on NaP conductance may move the neuron outside of a parameter space in which spontaneous oscillations can occur (Hutcheon and Yarom, 2000).

Synchrony

All electrically coupled cells displayed oscillation synchrony. Given the weak coupling strength, it is perhaps unsurprising that we did not observe evidence for millisecond-precision spike synchrony that is observed in other electrically coupled networks (Dugué et al., 2009; Trenholm et al., 2014). Furthermore, fusiform cells are likely coupled in their dendrites, which are very far and thus electrically isolated from the axon initial segment where spikes are generated (reviewed by Connors 2017). However, spike synchrony between fusiform cells of similar best frequencies is observed *in vivo* (Voigt and Young, 1988; Gochin et al., 1989; Stefanescu and Shore, 2015, 2017). Based on our results, spike synchrony *in vivo* is likely driven by shared synaptic input.

Physiological relevance

Further study will be needed to explore the presence of oscillations in the DCN *in vivo*. Modeling studies of oscillations driven by HCN and NaP show that synaptic noise enhances the likelihood of resonance and oscillations (Fransén et al., 2004; Prescott et al., 2008b). Slow oscillations do not appear to guide simple spontaneous spike rate as fusiform cells are known to spike at 20-30 Hz *in vivo* (Davis and Young, 2000; Ma and Brenowitz, 2012). Fusiform cells phase-lock to amplitude-modulated tones and have best envelope frequencies, but these modulation frequencies are much faster than 1-2 Hz (Kim et al., 1990; Rhode and Greenberg, 1994; Gdowski and Voigt, 1998). The best evidence for slow oscillations *in vivo* is from spontaneous bursting, which in guinea pig occurs at 0-0.2 Hz (Wu et al., 2016). HCN/NaP oscillations could underlie these burst rates, particularly if more intact electrical coupling *in vivo* imposes a slower network frequency (Stagkourakis et al., 2018).

It is possible that the oscillations are an epiphenomenon resulting from biophysical mechanisms that establish resonance in fusiform cells. Active dendritic conductances maintain robust oscillations and synchrony in networks with distal dendritic coupling (Saraga et al., 2006). Resonance is functionally important as it shapes the electrical response to synaptic input both from auditory input to the basal dendrites and multisensory input to apical dendrites. The distal dendrites are likely where fusiform electrical coupling occurs given that this is the site where they are coupled with molecular-layer interneurons known as superficial stellate cells (Apostolides and Trussell, 2013b). Oscillations or resonance may therefore perform some unique function in dendritic computations of the molecular layer where

multisensory inputs are received. NaP/HCN interactions may also endow fusiform cells with a resonant response to auditory input in the basal dendrites, functioning to shape the well-documented afterhyperpolarization that follows acoustic stimuli (Hancock and Voigt, 2002).

We found that fusiform cells typically show electrical coupling in slice when somas are within 80 μm of one another. According to three-dimensional reconstructions of frequency mapping in mouse DCN, it is likely that only fusiform cells within the same frequency domain are coupled (Muniak et al., 2013). Chemical synapses that are located close to electrical connections can enable synaptic input onto one cell to spread electrically to the other (Trenholm et al., 2014). NaP and HCN activation by parallel fiber input also leads to reshaping of the synaptic input, significantly increasing the amplitude and width of the EPSP (Apostolides and Trussell, 2014). Because gap junctions act as low pass filters, the slower EPSPs are kinetically ideal for transmission through gap junctions (Bennett and Zukin, 2004). Furthermore, active dendritic conductances such as NaP are known to amplify synaptically-induced conductances (Schwindt and Crill, 1995). Oscillations would therefore amplify synaptic-electrical input in a synchronized fashion between cells. It is therefore possible that fusiform coupling allows for distribution of synaptic input amongst fusiform cells that are within the same frequency domain. Shared variability resulting from synchronized oscillations may work to coordinate the output from a given frequency domain and therefore strengthen the perception of that frequency.

Acknowledgements

This work was supported by National Institutes of Health Grants DC004450 to L.O.T. and DC015187-03 to L.A.M. We thank members of the L.O.T. laboratory for helpful discussions and Jennifer Goldsmith, Ruby Larisch, and Michael Bateschell for assistance with mouse colony management.

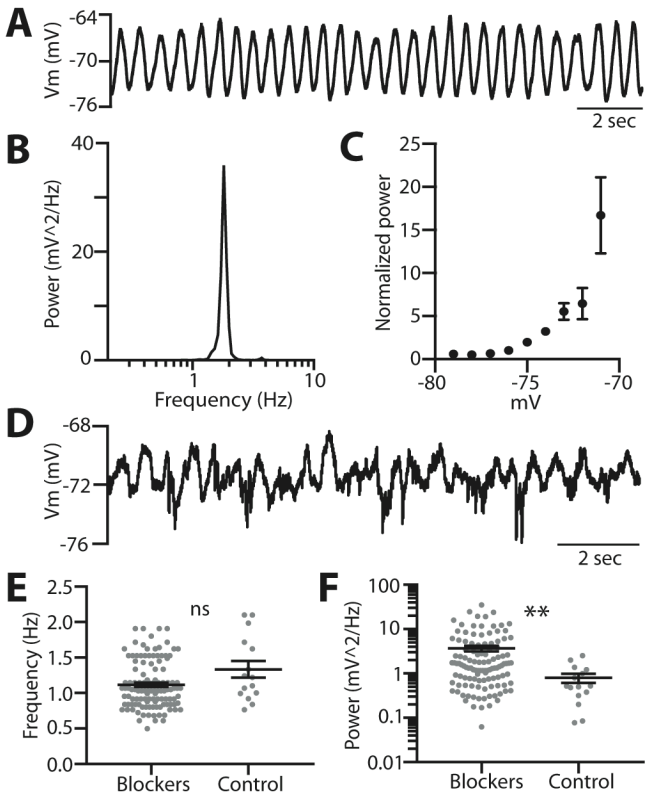

Figure 2.1. Fusiform cells display 1-2 Hz oscillations in resting membrane potential. **A,** Example raw voltage trace from an oscillating fusiform cell in the presence of blockers of fast synaptic transmission (see *Methods*). **B**, Power spectrum for example cell shown in *A*, with a large peak apparent between 1 and 2 Hz. **C**, Plot displaying the voltage dependence of subthreshold oscillations (n=10 cells, power is normalized to the power measured at -76 mV). **D,** Raw voltage trace showing oscillations in the absence of synaptic blockers. **E**, The frequency of oscillations was not affected by the presence of synaptic blockers (U=616, p=0.06, Mann-Whitney U). **F,** However, oscillation power was significantly greater in the presence of synaptic blockers (U=462, p=0.002, Mann-Whitney U). **p<0.01.

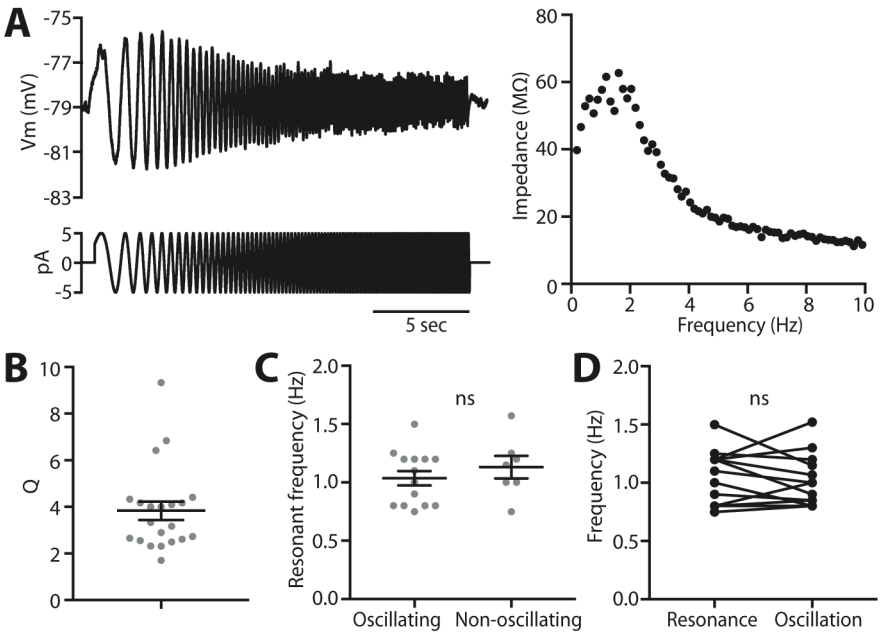

Figure 2.2. Fusiform cells display intrinsic resonant frequencies of 1-2 Hz. **A**, Average voltage response of a fusiform cell injected with a ZAP current, resulting in the impedance curve displayed to the right. The impedance curve for this cell shows a resonant peak at 1.6 Hz. **B**, All fusiform cells produced impedance curves with a *Q* value greater than 1, indicating the presence of a resonant peak. **C**, Both spontaneously oscillating and non-oscillating fusiform cells displayed resonant peaks in their impedance profiles, with no population difference in resonant frequencies ($t(19)=0.9$, $p=0.399$, two-tailed t-test). **D**, The resonant frequency of oscillating cells matched the frequency of their spontaneous oscillations ($t(13)=0.679$, $p=0.509$, paired two-tailed t-test).

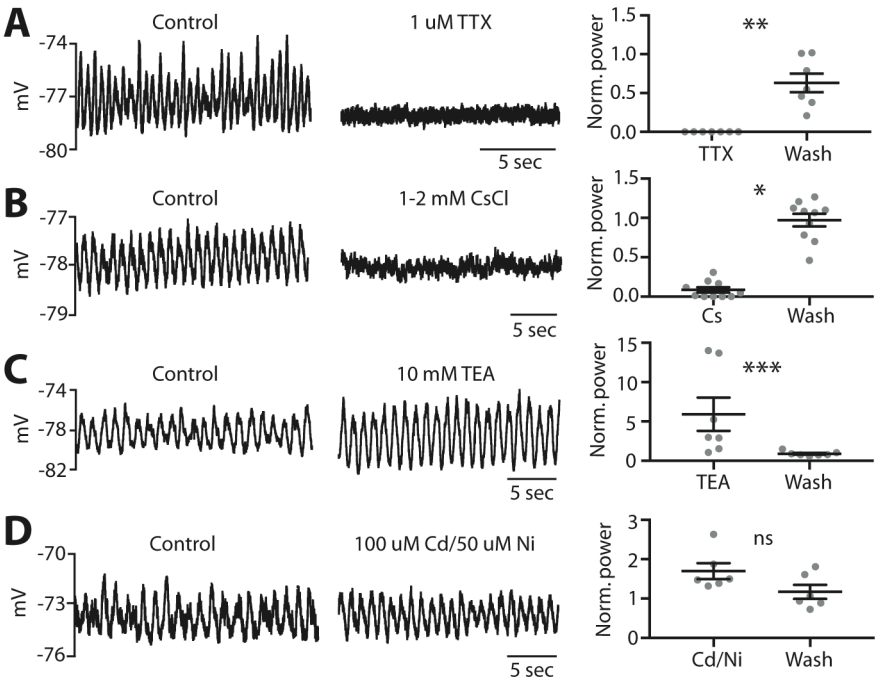

Figure 2.3. Subthreshold oscillations require persistent Na^+ and HCN conductances. Oscillations were blocked by bath application of 1 mM TTX (**A**; W=11.14, p=0.0012, Friedman test) and 1-2 mM CsCl (**B**; F(1.2, 10.8)=8.7, p=0.01, RM one-way ANOVA). Conversely, 10 mM TEA (**C**) increased oscillation power (F=12.29, p=0.0003, Friedman test). Broad-spectrum Ca^{2+} channel blockers (**D**) also appeared to increase oscillations, but the enhancement was not significant (F(1.6,7.9)=4.64, p=0.052, RM one-way ANOVA). Bias current was applied to correct for membrane potential changes with drug application before power measurements were made. Population graphs are normalized to control. *p<0.05, **p<0.01, ***p<0.001.

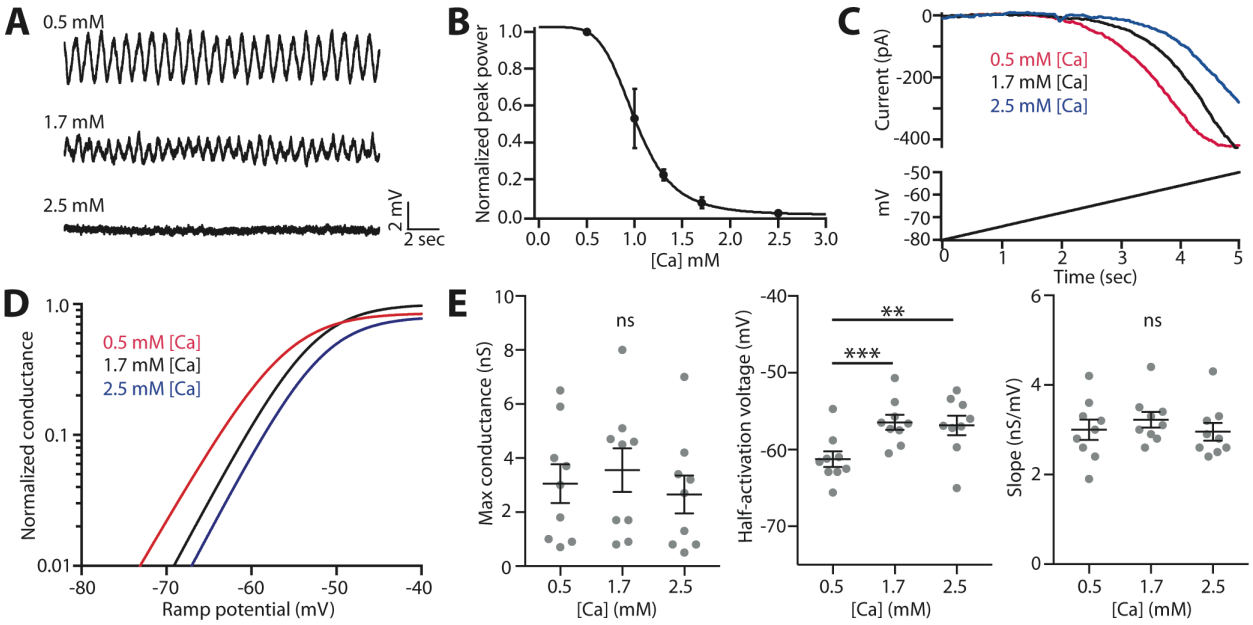

Figure 2.4. Effect of Ca^{2+} concentration on the Na^{+} channel activation curve. **A**, Raw voltage traces illustrate how the amplitude of oscillations is larger in lower external Ca^{2+} concentrations. **B**, Dose-response curve displaying oscillation power measured in fusiform cells across varying external Ca^{2+} concentrations (n=8 cells). **C**, Na^{+} conductance curves were measured in varying external Ca^{2+} concentrations by applying a 5-second ramp holding from -80 to -50 mV. Raw current traces in response to the voltage ramp are displayed for one cell. **D**, Normalized conductance curves for example cell shown in **C**. Conductance curves were normalized to the maximum conductance values measured from fitting the data with a Boltzmann sigmoid. **E**, Population data comparing maximum conductance, half-activation voltage, and slope measured from Boltzmann fits across Ca^{2+} concentrations. Maximum conductance was unchanged between conditions ($F(1.2, 9.9)=1.6$, $p=0.239$, RM one-way ANOVA). Half-activation voltage was positively shifted in Ca^{2+} concentrations greater than 0.5 ($F(1.7, 13.3)=31.07$, $p<0.0001$, RM one-way ANOVA). There was no significant difference in

slope between different external Ca^{2+} concentrations ($F(1.1, 9.0)=0.514$, $p=0.514$, RM one-way ANOVA). *$p<0.05$, **$p<0.01$, ***$p<0.001$.

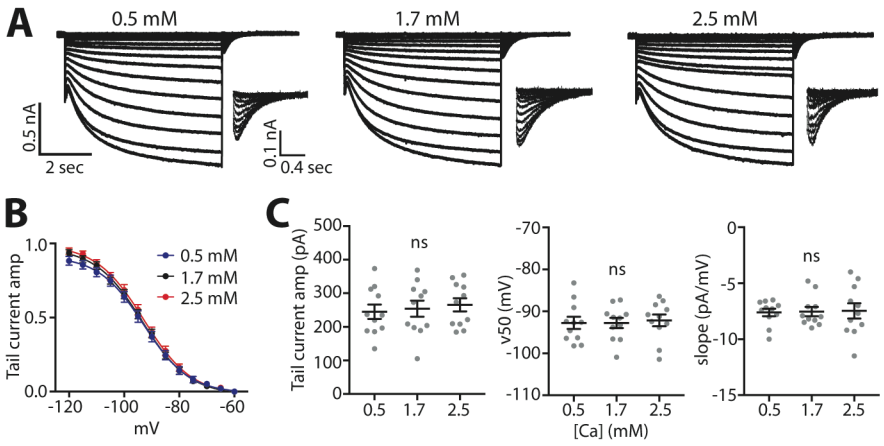

Figure 2.5. Effect of Ca^{2+} concentration on the HCN channel activation curve. **A**, Example HCN tail currents (magnified in insets) measured in varying concentrations of Ca^{2+}: cells were held at -60 mV, injected with current steps from -120 to -60 mV in 5 mV increments for 5 seconds, and stepped back to -60 mV to induce a tail current. **B**, The HCN activation curve was generated by measuring the amplitude of the resulting tail current associated with each voltage step (n=11 cells). Population data are fit with Boltzmann sigmoid equations. **C**, The maximum tail current amplitude, half-activation voltage, and slope did not vary significantly between Ca^{2+} concentrations.

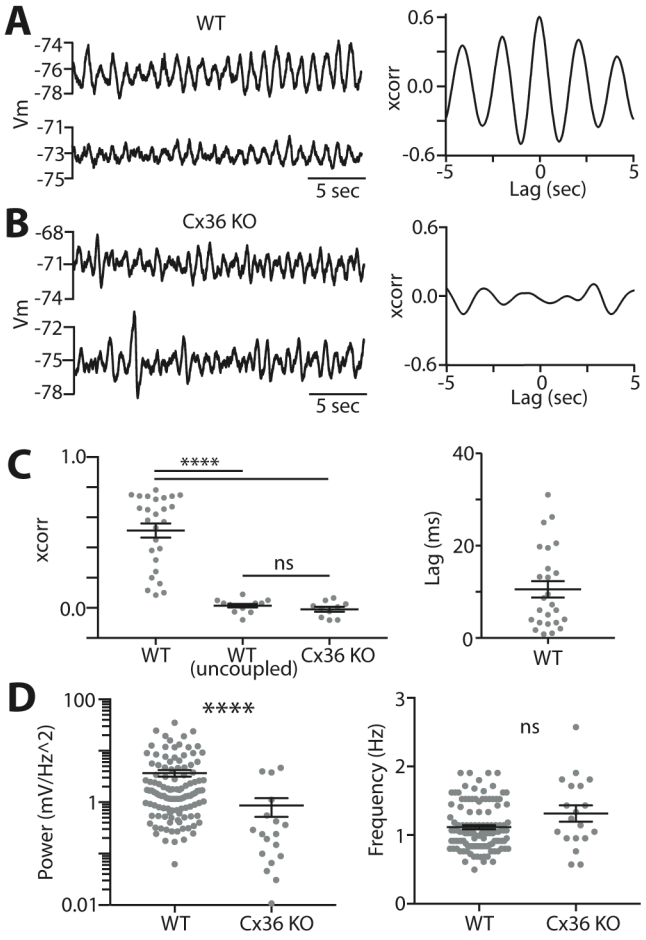

Figure 2.6. Oscillation synchrony in electrically coupled fusiform cells. **A**, Paired recordings from electrically coupled fusiform cells in WT tissue. The resulting crosscorrelogram for this pair, shown to the right, displays a peak around zero lag. **B**, Dual recordings from two fusiform cells in Cx36 KO tissue. The resulting crosscorrelogram to the right shows no central peak around zero lag. **C**, *Left*: Electrically coupled cells in WT tissue have significantly larger *xcorr* values (measured at lag zero) than uncoupled pairs in WT and Cx36 KO tissue ($F(2,46)=49.6$, $p<0.0001$, one-way ANOVA). *Right*: Lag times measured for the peak in oscillation crosscorrelograms for coupled pairs in WT tissue. **D**, Population statistics comparing

basic features of oscillations recorded from WT *vs.* Cx36 KO animals. *Left*: Oscillation power was significantly lower in fusiform cells measured from Cx36 KO tissue (U=405, p<0.0001, Mann-Whitney U). *Right*: There was no significant difference in oscillation frequency between WT and KO (U=846, p=0.096, Mann-Whitney U). ****p<0.0001.

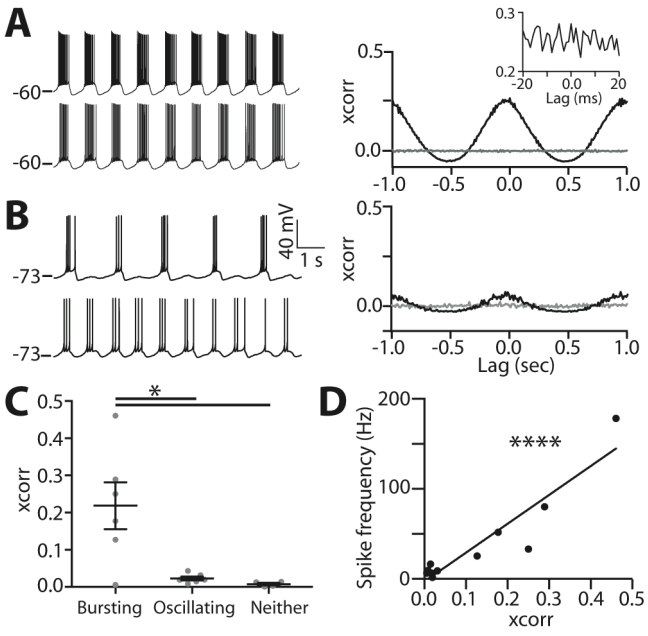

Figure 2.7. Broad-scale spike synchrony displayed by electrically coupled fusiform cells. **A,** Paired recordings from electrically coupled fusiform cells that are both *bursting* (left) and the resulting spike crosscorrelogram for this example pair (right). The inset displays a lack of a peak around zero ms lag between ±20 ms: this indicates a lack of fine-scale spike synchrony. Indeed, no pair displayed the fine-scale spike synchrony that is commonly seen in strongly electrically coupled neurons of other brain regions. However, the crosscorrelogram on a wider time scale shows a slow oscillation matching the oscillation frequency of the neuron, indicating broad-scale spike synchrony. **B,** Paired recordings from electrically coupled fusiform cells that are both *oscillating* (left) and the resulting spike crosscorrelogram for this example pair (right). Pairs either consisted of cells that were bursting (>10 spikes per oscillation cycle), oscillating (<5 spikes per oscillation cycle), or not oscillating. Oscillating pairs showed crosscorrelogram oscillations similar to bursting pairs, but much weaker. **C,** *xcorr* measured at zero lag for spike crosscorrelograms across the population of fusiform

pairs. *xcorr* values measured from bursting pairs were significantly larger than *xcorr* values measured from oscillating and non-oscillating pairs, which both displayed *xcorr* values around 0 (W=8, p=0.01, Kruskal-Wallis). D, There was a strong linear correlation between spike *xcorr* and spike frequency in bursting pairs (R^2=0.86, p<0.0001, linear regression). Spike frequency was averaged between cells to get one value for the pair. *p<0.05, ****p<0.0001.

SUMMARY AND CONCLUSIONS

1. Co-release of inhibitory neurotransmitters in the inferior colliculus

In Chapter 1 I established the presence of GABA/glycine co-release from ascending fibers terminating in the ICC. Prior to this study, co-release was a well-established phenomenon in auditory brainstem regions, but had not been observed or studied in the auditory midbrain. I tested many of the main hypotheses for differential impacts of co-released glycine *vs.* GABA that underlie the foundation for possible functional impacts of co-release. However, the GABA- and glycinergic components were surprisingly similar, which perhaps suggest they play a redundant role in ICC signaling. Our study was unique for its technological capabilities, which allowed us to stimulate co-releasing fibers and fibers from specific ascending regions in a specific manner.

What is the function of GABA/glycine co-release in the auditory midbrain?

The apparent redundancy of released transmitters could be essential for the IC to operate in its unique role as the interface for the lower auditory brainstem regions and the thalamus/cortex where glycinergic and GABAergic transmission dominate, respectively. For example, this glycinergic input is important for the startle response, so individuals with a compromised glycinergic system have an exaggerated startle response. Currently the most effective treatment is GABA receptor agonists, which fits nicely with our findings (Zhou et al., 2002).

There are other possible impacts of GABA/glycine co-release in the ICC that could be explored in the future. Though our study was focused on the adult auditory brainstem, the co-release observed in adulthood may be a byproduct of its presence

and possible functional role during development. For example, both $GABA_A$ and $GABA_B$ receptors have a neurotrophic role in development, so GABA may be uniquely required for proper development of co-releasing synapses (Represa and Ben-ari, 2005; Gaiarsa and Porcher, 2013). GABA may also be uniquely required for proper receptor clustering during development. Gephyrin is thought to be critical for postsynaptic clustering of glycine receptors, but GABA receptors that contain certain subunits (including α1 subunits that are present at high density in the IC) are able to cluster independent of gephyrin (Milbrandt et al., 1997; Feng et al., 1998; Kneussel et al., 2001). GABA receptor clusters also induce gephyrin clustering, which would hypothetically enable subsequent glycine receptor clustering in the development of glycinergic or GABA/glycingeric synapses (Lévi et al., 2004).

In Chapter 1, we probed for possible spillover effects of GABA and were unable to detect any activation of $GABA_B$ receptors. It would be interesting in the future to also investigate the possible impact of glycine spillover on NMDA receptors. Glycine is a co-agonist of NMDARs and spillover in the superficial dorsal horn of the spinal cord has shown to potentiate the NMDA response (Ahmadi et al., 2003). In the IC, NMDARs mediate spike output in response to sound *in vivo* (Feldman et al., 1996; Sanchez et al., 2007). Studies in slice show NMDAR-mediated currents in response to lemniscal stimulation when cells are at resting potentials as well as NMDAR-dependent long-term potentiation following a classic tetanic stimulation induction protocol (Zhang and Wu, 2000; Ma et al., 2002a). Glycine spillover could therefore modulate auditory processing and plasticity in the IC via NMDARs. One caveat is that our optogenetic stimulation causes release from both mixed and purely glycinergic terminals, so this experiment

cannot distinguish if glycine from specifically co-releasing terminals is required for NMDAR potentiation.

Did the use of optogenetics affect our results?

Optogenetics has some inherent limitations. Some researchers have expressed concern that wide-field stimulation is not optimal because direct stimulation of boutons may change the shape of the presynaptic waveform or directly depolarize the terminal to allow in Ca^{2+} (Jackman et al., 2014). The solution to this is to use high-intensity light focused specifically over fiber tracts away from the terminals. However, I was not able to use distant stimulation as my microscope was not set up for this type of focused stimulation. Nonetheless, we believe direct terminal depolarization did not affect our results as we were able to achieve rates of short-term synaptic depression with light similar to electrical stimulation. However, it cannot be ruled out entirely.

Are there presynaptic glycine receptors on co-releasing terminals?

One avenue that we did not explored in Chapter 1 was the presence of presynaptic glycine receptors. Glycine receptors are normally localized to postsynaptic terminals as a result of the high binding affinity of the beta subunit with gephyrin, an anchoring protein (Tyagarajan and Fritschy, 2014). However, homomeric GlyRs that contain only alpha subunits are expressed presynaptically (Turecek and Trussell, 2001; Jeong et al., 2003; Xiong et al., 2014). In rat, glycinergic boutons terminating on spinal dorsal commissural neurons express GlyRs, and the high internal Cl^- concentration allows for glycine-mediated autofacilitation at that synapse (Jeong et al., 2003). It would therefore be interesting to use a drug that specifically agonizes or antagonizes homomeric receptors to explore whether glycine might uniquely modulate co-releasing

terminals in ICC. Dehydroxylcannabidiol (DH-CND), which has been shown to block homomeric GlyRs with high specificity (Xiong et al., 2011, 2012), might serve this purpose. It would also be interesting to test the effect of blocking GlyRs on excitatory synaptic input, as co-released glycine could also act on nearby glutamergic terminals. However, these experiments may give the same results as the effect of CGP in Chapter 1.

2. Electrical resonance and slow oscillations in cochlear nucleus

In Chapter 2, I examined resonance and slow neural oscillations in the principal cell of DCN. Fusiform cells display a 1-2 Hz subthreshold oscillation in their resting membrane potential. These oscillations are driven by activation of subthreshold HCN and persistent Na^+ channel conductances, which presumably activate and inactivate in an alternating voltage-dependent manner to drive the regular voltage fluctuations. The oscillations could not be observed in external Ca^{2+} concentrations greater than 1.7 mM, which likely accounts for the fact that previous studies, which typically used external concentrations of 2 mM, did not observe these oscillations. Finally, the electrical coupling of fusiform cells enabled oscillations to synchronize, suggesting that oscillations may have computational impact on the fusiform cell network.

Do conductances other than NaP and HCN modulate oscillations?

The investigation of which conductances underlie the generation of subthreshold oscillations was relatively straightforward, but it would be interesting to further study whether other conductances might play a secondary part by impacting the speed or amplitude of oscillations. It would also be especially interesting to more closely explore a possible role for M-type K^+ conductance (mediated by KCNQ channels) in shaping

fusiform cell oscillations. M currents are frequently involved in other regions where HCN and NaP underlie the oscillations and play a more modulatory role. In these regions, activating M channels increases the frequency of oscillations, resulting in theta frequencies (Prescott et al., 2008b; Boehlen et al., 2013). This issue is especially interesting for fusiform cells because noise-traumatized animals that develop tinnitus show increased M-type conductance, leading to more bursting and synchrony as well as general excitation levels (Li et al., 2013; Wu et al., 2016). Modified oscillation dynamics could explain the increase in bursting and synchrony that are thought to perhaps underlie the tinnitus percept (Wu et al., 2016).

Does Ca^{2+} regulate oscillation strength via Na^{+} channels?

An important result from our work was that oscillations disappeared in the presence of external Ca^{2+} concentrations greater than 1.7 mM. We hypothesized that this was due to the effect of Ca^{2+} concentration on the Na^{+} channel activation curve. Indeed, higher Ca^{2+} concentrations caused a positive shift in the half-maximal activation voltage of fusiform persistent Na^{+} channel conductance. Conversely, there was no effect of Ca^{2+} concentration on the HCN conductance. Though it is likely that the impact of Ca^{2+} on Na+ channels is the mechanism by which Ca^{2+} concentration modulates oscillation strength, it would be useful in future studies to assess this possibility with a biophysical model (see e.g. Golomb et al., 2006).

Several biophysical models of fusiform cells already exist (Kanold and Manis 2001, Leao et al. 2012, and Ceballos et al. 2016). There are also several biophysical models that describe oscillations generated from HCN and NaP conductances (Dickson et al. 2000, Fransén et al. 2004, and Boehlen et al. 2013). One would first need to

describe the theoretical requirements for slow oscillations to appear in fusiform cells and compare the model parameters to measured values. When there are two conductances involved in generating spontaneous oscillations, different conductance level combinations will result in different oscillatory outputs in response to current input. For example, current input may result in a brief oscillation that quickly collapses to steady membrane potential or, alternatively, the generation of spontaneous oscillations. These varying conductance combinations and system outputs can be explored using phase-plane plots from dynamical systems analysis (Hutcheon and Yarom, 2000). Phase-plane plot data can then be used to construct a stability diagram that shows what range of combined conductances are the best fit to result in spontaneous oscillations. Along with testing the relationship between external Ca^{2+} concentration, NaP activation, and oscillation strength, modeling and stability diagrams could also be used to probe general questions of how "robust" the oscillations are under different conditions. This would allow predictions, for example, about oscillations *in vivo* and in response to different types of synaptic input (Prescott et al., 2008a).

Is oscillation synchrony confined to isotopic frequency domains?

Our results indicate that electrical coupling between fusiform cells, though very weak, enables synchronization of slow oscillations between cells. We further observed that fusiform cells were typically only connected when they were located within 80 μm of each other. Muniak et al. (2013) made a highly detailed three-dimensional model of the DCN that maps tonotopy and 80 μm is well within range of a single tonotopic domain. We therefore suggest that only fusiform cells within the same tonotopic domain are electrically connected and therefore display oscillation synchrony. If true, this could

have massive implications for the function of oscillations in frequency coding. However, it will be important to confirm this hypothesis with further experiments such as *in vivo* recordings from multiple fusiform cells within the same tonotopic domain. Alternatively, one could use transgenic tools such as the *Fos*-Cre-ER mouse, a genetic line that enables Cre expression in *Fos*-expressing neurons (Guenthner et al., 2013). *Fos* is an immediate early gene that has been established as a marker for recently activated neurons (Bullitt, 1990). This mouse can therefore be crossed with a Cre-dependent reporter line to enable fluorescent protein expression in recently activated neurons. The mice could be exposed to a pure tone and fluorescing fusiform cells could be patched *in vitro* to confirm that electrically coupled fusiforms cells are confined to the same tonotopic domain with DCN.

REFERENCES

Adams JC (1997) Projections from octopus cells of the posteroventral cochlear nucleus to the ventral nucleus of the lateral lemniscus in cat and human. Audit Neurosci 3:335–350.

Ahmadi S, Muth-Selbach U, Lauterbach A, Lipfert P, Neuhuber WL, Zeilhofer HU (2003) Facilitation of spinal NMDA receptor currents by spillover of synaptically released glycine. Science 300:2094–2098.

Aitkin LM, Dickhaus H, Schult W, Zimmermann M (1978) External nucleus of inferior colliculus: auditory and spinal somatosensory afferents and their interactions. J Neurophysiol 41:837–847.

Apostolides PF, Trussell LO (2013a) Rapid, activity-independent turnover of vesicular transmitter content at a mixed glycine/GABA synapse. J Neurosci 33:4768–4781.

Apostolides PF, Trussell LO (2013b) Regulation of interneuron excitability by gap junction coupling with principal cells. Nat Neurosci 16:1764–1772.

Apostolides PF, Trussell LO (2014) Control of interneuron firing by subthreshold synaptic potentials in principal cells of the dorsal cochlear nucleus. Neuron 83:324–330.

Atasoy D, Aponte Y, Su HH, Sternson SM (2008) A FLEX switch targets channelrhodopsin-2 to multiple cell types for imaging and long-range circuit mapping. 28:7025–7030.

Auerbach BD, Rodrigues P V, Salvi RJ (2014) Central gain control in tinnitus and hyperacusis. Front Neurol 5:206.

Awatramani GB, Turecek R, Trussell LO (2005) Staggered development of GABAergic and glycinergic transmission in the MNTB. J Neurophysiol 93:819–828.

Bahmer A, Gupta DS (2018) Role of oscillations in auditory temporal processing: a general model for temporal processing of sensory information in the brain? Front Neurosci 12:1–12.

Bal R, Green GGR, Rees A, Sanders DJ (2002) Firing patterns of inferior colliculus neurons–histology and mechanism to change firing patterns in rat brain slices. Neurosci Lett 317:42–46.

Bara M, Guiet-Bara A, Durlach J (1993) Regulation of sodium and potassium pathways by magnesium in cell membranes. Magnes Res 6: 167-177.

Beatty JA, Song SC, Wilson CJ (2015) Cell-type-specific resonances shape the responses of striatal neurons to synaptic input. J Neurophysiol 113:688–700.

Beierlein M, Gibson JR, Connors BW (2000) A network of electrically coupled interneurons drives synchronized inhibition in neocortex. Nat Neurosci 3:904–910.

Belelli D, Lambert JL (2005) Neurosteroids: endogenous regulators of the $GABA_A$ receptor. Nature Reviews Neuroscience 6: 565-575.

Bennett MVL, Zukin RS (2004) Electrical coupling and neuronal synchronization in the mammalian brain. Neuron 41:495–511.

Bettus G, Wendling F, Guye M, Valton L, Régis J, Chauvel P, Bartolomei F (2008) Enhanced EEG functional connectivity in mesial temporal lobe epilepsy. Epilepsy Res 81:58–68.

Boehlen A, Henneberger C, Heinemann U, Erchova I (2013) Contribution of near-threshold currents to intrinsic oscillatory activity in rat medial entorhinal cortex layer II stellate cells. J Neurophysiol 109:445–463.

Borst JGG (2010) The low synaptic release probability in vivo. Trends Neurosci 33:259–266.

Bullitt E (1990) Expression of C-fos-like protein as a marker for neuronal activity following noxious stimulation in the rat. J Comp Neurol 296:517–530.

Buzsáki G (2006) Rhythms of the brain. Oxford, UK: Oxford UP.

Buzsáki G, Draguhn A (2004) Neuronal oscillations in cortical networks. Science (80-) 304:1926–1930.

Campbell DT (1976) Kinetic and pharmacological properties of the sodium channel of frog skeletal muscle. J Gen Physiol 67:309–323.

Campbell DT, Hille B (1976) Kinetic and pharmacological properties of the sodium channel of frog skeletal muscle. J Gen Physiol 67:309–323.

Cant NB (2005) Projections from the cochlear nuclear complex to the inferior colliculus. In: The Inferior Colliculus (Winer JA, Schreiner CE, eds), pp 115-131. New York: Springer.

Cant NB, Benson CG (2006) Organization of the inferior colliculus of the gerbil

(Meriones unguiculatus): Differences in distribution of projections from the cochlear nuclei and the superior olivary complex. J Comp Neurol 495:511–528.

Caspari F, Baumann VJ, Garcia-Pino E, Koch U (2015) Heterogeneity of intrinsic and synaptic properties of neurons in the ventral and dorsal parts of the ventral nucleus of the lateral lemniscus. Front Neural Circuits 9:1–15.

Caspary DM, Ling L, Turner JG, Hughes LF (2008) Review: Inhibitory neurotransmission, plasticity and aging in the mammalian central auditory system. J Exp Biol 211:1781–1791.

Ceballos CC, Li S, Roque AC, Tzounopoulos T, Leão RM (2016) Ih Equalizes Membrane Input Resistance in a Heterogeneous Population of Fusiform Neurons in the Dorsal Cochlear Nucleus. Front Cell Neurosci 10:1–15.

Chen Y, Li X, Rotstein HG, Nadim F (2016) Membrane potential resonance frequency directly influences network frequency through electrical coupling. J Neurophysiol.

Chéry N, De Koninck Y (1999a) Junctional versus extrajunctional glycine and GABA(A) receptor-mediated IPSCs in identified lamina I neurons of the adult rat spinal cord. J Neurosci 19:7342–7355.

Chéry N, De Koninck Y (1999b) Junctional versus extrajunctional glycine and GABA(A) receptor-mediated IPSCs in identified lamina I neurons of the adult rat spinal cord. J Neurosci 19:7342–7355.

Clements JD, Bekkers JM (1997) Detection of spontaneous synaptic events with an optimally scaled template. Biophys J 73:220–229.

Connors BW (2017) Synchrony and so much more: diverse roles for electrical synapses in neural circuits. Dev Neurobiol 77:610–624.

Covey E, Casseday J (1991) The monaural nuclei of the lateral lemniscus in an echolocating bat: parallel pathways for analyzing temporal features of sound. J Neurosci 11:3456–3470.

Crochet S, Petersen CCH (2006) Correlating whisker behavior with membrane potential in barrel cortex of awake mice. Nat Neurosci 9:608–610.

Davis KA, Young ED (2000) Pharmacological evidence of inhibitory and disinhibitory neuronal circuits in dorsal cochlear nucleus. Am Physiol Soc 83:926–940.

del Castillo J, Katz B (1954) Quantal components of the end-plate potential. J Physiol

124:560–573.

Dickson CT, Magistretti J, Shalinsky MH, Fransén E, Hasselmo ME, Alonso A (2000) Properties and role of Ih in the pacing of subthreshold oscillations in entorhinal cortex layer II neurons. Am J Physiol 83:2562–2579.

Dixon C, Sah P, Lynch JW, Keramidas A (2014) GABAA receptor α and γ subunits shape synaptic currents via different mechanisms. J Biol Chem 289:5399–5411.

Dong S, Mulders WHAM, Rodger J, Woo S, Robertson D (2010a) Acoustic trauma evokes hyperactivity and changes in gene expression in guinea-pig auditory brainstem. Eur J Neurosci 31:1616–1628.

Dong S, Rodger J, Mulders WHAM, Robertson D (2010b) Tonotopic changes in GABA receptor expression in guinea pig inferior colliculus after partial unilateral hearing loss. Brain Res 1342:24–32.

Draguhn A, Traub RD, Schmitz D, Jefferys JGR (1998) Electrical coupling underlies high-frequency oscillations in the hippocampus in vitro. Nature 394:189–192.

Druga R, Syka J, Rajkowska G (1997) Projections of auditory cortex onto the inferior colliculus in the rat. Physiol Res 46:215–222.

Dugladze T, Vida I, Tort AB, Gross A, Otahal J, Heinemann U, Kopell NJ, Gloveli T (2007) Impaired hippocampal rhythmogenesis in a mouse model of mesial temporal lobe epilepsy. Proc Natl Acad Sci 104:17530–17535.

Dugué GP, Brunel N, Hakim V, Schwartz E, Chat M, Lévesque M, Courtemanche R, Léna C, Dieudonné S (2009) Electrical Coupling Mediates Tunable Low-Frequency Oscillations and Resonance in the Cerebellar Golgi Cell Network. Neuron 61:126–139.

Dugue GP, Dumoulin A, Triller A, Dieudonné S (2005) Target-dependent use of coreleased inhibitory transmitters at central synapses. J Neurosci 25:6490–6498.

Dumoulin A, Triller A, Dieudonné S (2001) IPSC kinetics at identified GABAergic and mixed GABAergic and glycinergic synapses onto cerebellar Golgi cells. J Neurosci 21:6045–6057.

Eggermont JJ (1992) Neural interaction in cat primary auditory cortex. Dependence on recording depth, electrode separation, and age. J Neurophysiol 68:1216–1228.

Faingold CL, Gehlbach G, Caspary DM (1989) On the role of GABA as an inhibitory

neurotransmitter in inferior colliculus neurons: iontophoretic studies. Brain Res 500:302–312.

Fatt BYP, Katz B (1952) Spontaneous subthreshold activity at motor nerve endings. JPhysiol 117:109–128.

Feldman DE, Brainard MS, Knudsen EI (1996) Newly learned auditory responses mediated by NMDA receptors in the owl inferior colliculus. Science (80-) 271:525–528.

Feng G, Mellor RH, Bernstein M, Keller-Peck C, Nguyen QT, Wallace M, Nerbonne JM, Lichtman JW, Sanes JR (2000) Imaging neuronal sets in transgenic mice expressing multiple spectral variants of GFP. Neuron 28:41–51.

Feng G, Tintrup H, Kirsch J, Nichol MC, Kuhse J, Betz H, Sanes JR (1998) Dual requirement for gephyrin in glycine receptor clustering and molybdoenzyme activity. Science (80-) 282:1321–1325.

Fettiplace R, Fuchs PA (1999) Mechanisms of hair cell tuning. Annu Rev Physiol 61:809–834.

Fischl MJ, Weimann SR, Kearse MG, Burger RM (2014) Slowly emerging glycinergic transmission enhances inhibition in the sound localization pathway of the avian auditory system. J Neurophysiol 111:565–572.

Frankenhaeuser B, Hodgkin A (1957) The action of calcium on the electrical properties of squid axon. J Physiol 137:218–244.

Fransén E, Alonso AA, Dickson CT, Magistretti J, Hasselmo ME (2004) Ionic mechanisms in the generation of subthreshold oscillations and action potential clustering in entorhinal layer II stellate neurons. Hippocampus 14:368–384.

Frisch C, Souza-Silva MA De, Söhl G, Güldenagel M, Willecke K, Huston JP, Dere E (2005) Stimulus complexity dependent memory impairment and changes in motor performance after deletion of the neuronal gap junction protein connexin36 in mice. Behav Brain Res 157:177–185.

Fujino K, Oertel D (2003) Bidirectional synaptic plasticity in the cerebellum-like mammalian dorsal cochlear nucleus. Proc Natl Acad Sci U S A 100:265–270.

Gaiarsa J, Porcher C (2013) Emerging neurotrophic role of GABAB receptors in neuronal circuit development. Front Cell Neurosci 7:1–11.

Gardner SM, Trussell LO, Oertel D (2001) Correlation of AMPA receptor subunit composition with synaptic input in the mammalian cochlear nuclei. J Neurosci 21:7428–7437.

Gdowski GT, Voigt HF (1998) Intrinsic oscillations and discharge regularity of units in the dorsal cochlear nucleus (DCN) of the barbiturate anesthetized gerbil. Ann Biomed Eng 26:473–487.

Gentet LJ, Avermann M, Matyas F, Staiger JF, Petersen CCH (2010) Membrane potential dynamics of GABAergic neurons in the barrel cortex of behaving mice. Neuron 65:422–435.

Gibson JR, Belerlein M, Connors BW (1999) Two networks of electrically coupled inhibitory neurons in neocortex. Nature 402:75–79.

Glendenning KK, Baker BN, Hutson KA, Masterton RB (1992) Acoustic chiasm V: Inhibition and excitation in the ipsilateral and contralateral projections of LSO. J Comp Neurol 319:100–122.

Glendenning KK, Masterton RB, Baker BN, Wenthold RJ (1991) Acoustic Chiasm III: Nature, distribution, and sources of afferents to the lateral superior olive in the cat. J Comp Neurol 310:377–400.

Gochin PM, Kaltenbach JA, Gerstein GL (1989) Coordinated activity of neuron pairs in anesthetized rat dorsal cochlear nucleus. Brain Res 497:1–11.

Golomb D, Yue C, Yaari Y (2006) Contribution of persistent Na+ current and M-type K+ current to somatic bursting in CA1 pyramidal cells: combined experimental and modeling study. J Neurophysiol 96:1912–1926.

Gonzalez-Burgos G, Cho RY, Lewis DA (2015) Alterations in cortical network oscillations and parvalbumin neurons in schizophrenia. Biol Psychiatry 77:1031–1040.

González-Hernández T, Mantolán-Sarmiento B, González-González B, Pérez-González H (1996) Sources of GABAergic input to the inferior colliculus of the rat. J Comp Neurol 372:309–326.

Gröticke I, Hoffmann K, Löscher W (2008) Behavioral alterations in a mouse model of temporal lobe epilepsy induced by intrahippocampal injection of kainate. Exp Neurol 213:71–83.

Guenthner CJ, Miyamichi K, Yang HH, Heller HC, Luo L (2013) Permanent genetic access to transiently active neurons via TRAP: Targeted Recombination in Active Populations. Neuron 78:773–784.

Hancock KE, Voigt HF (2002) Intracellularly labeled fusiform cells in dorsal cochlear nucleus of the gerbil. I. Physiological response properties. J Neurophysiol 87:2520–2530.

Haplea S, Covey E, Casseday JH (1994) Frequency tuning and response latencies at three levels in the brainstem of the echolocating bat, Eptesicus fuscus. J Comp Physiol A 174:671–683.

Helfert RH, Juiz JM, Bledsoe SC, Bonneau JM, Wenthold RJ, Altschuler RA (1992) Patterns of glutamate, glycine, and GABA immunolabeling in four synaptic terminal classes in the lateral superior olive of the guinea pig. J Comp Neurol 323:305–325.

Holmstrom L a, Eeuwes LBM, Roberts PD, Portfors C V (2010) Efficient encoding of vocalizations in the auditory midbrain. J Neurosci 30:802–819.

Hormuzdi SG, Pais I, LeBeau FEN, Towers SK, Rozov A, Buhl EH, Whittington MA, Monyer H (2001) Impaired electrical signaling disrupts gamma frequency oscillations in connexin 36-deficient mice. Neuron 31:487–495.

Horn R (1999) The dual role of calcium: pore blocker and modulator of gating. Proc Natl Acad Sci U S A 96:3331–3332.

Hosie AM, Dunne EL, Harvey RJ, Smart TG (2003) Zinc-mediated inhibition of GABAAreceptors: Discrete binding sites underlie subtype specificity. Nat Neurosci 6:362–369.

Hu H, Vervaeke K, Graham LJ, Storm JF (2009) Complementary theta resonance filtering by two spatially segregated mechanisms in CA1 hippocampal pyramidal neurons. J Neurosci 29:14472–14483.

Huerta PT, Lisman JE (1995) Bidirectional synaptic plasticity induced by a single burst during cholinergic theta oscillation in CA1 in vitro. Neuron 15:1053–1063.

Hughes SW, Cope DW, Blethyn KL, Crunelli V (2002) Cellular mechanisms of the slow (<1 Hz) oscillation in thalamocortical neurons in vitro. Neuron 33:947–958.

Hutcheon B, Miura RM, Puil E (1996) Subthreshold membrane resonance in neocortical neurons. J Neurophysiol 76:683–697.

Hutcheon B, Yarom Y (2000) Resonance, oscillation and the intrinsic frequency preferences of neurons. Trends Neurosci 23:216–222.

Ishibashi H, Yamaguchi J, Nakahata Y, Nabekura J (2013) Dynamic regulation of glycine-GABA co-transmission at spinal inhibitory synapses by neuronal glutamate transporter. J Physiol 591:3821–3832.

Ishihara N, Armsen W, Papadopoulos T, Betz H, Eulenburg V (2010) Generation of a mouse line expressing cre recombinase in glycinergic interneurons. Genesis 48:437–445.

Ito T, Oliver DL (2012) The basic circuit of the IC: tectothalamic neurons with different patterns of synaptic organization send different messages to the thalamus. Front Neural Circuits 6:48.

Jackman SL, Beneduce BM, Drew IR, Regehr WG (2014) Achieving high-frequency optical control of synaptic transmission. J Neurosci 34:7704–7714.

Jeong HJ, Jang IS, Moorhouse AJ, Akaike N (2003) Activation of presynaptic glycine receptors facilitates glycine release from presynaptic terminals synapsing onto rat spinal sacral dorsal commissural nucleus neurons. J Physiol 550:373–383.

Johnston J, Forsythe ID, Kopp-Scheinpflug C (2010) Going native: voltage-gated potassium channels controlling neuronal excitability. J Physiol 588:3187–3200.

Jonas P, Bischofberger J, Sandkuhler J (1998) Corelease of two fast neurotransmitters at a central synapse. Science (80-) 281:419–424.

Joris PX, Schreiner CE, Rees a (2004) Neural processing of amplitude-modulated sounds. Physiol Rev 84:541–577.

Kanold PO, Manis PB (2001) A physiologically based model of discharge pattern regulation by transient K+ currents in cochlear nucleus pyramidal cells. Am Physiol Soc 85:523–538.

Kelly JB, Caspary DM (2005) Pharmacology of the inferior colliculus. In: The Inferior Colliculus (Winer JA, Schreiner CE, eds), pp 248-281. New York: Springer.

Kim DO, Sirianni JG, Chang SO (1990) Responses of DCN-PVCN neurons and auditory nerve fibers in unanesthetized decerebrate cats to AM and pure tones: Analysis with autocorrelation/power-spectrum. Hear Res 45:95–113.

Kim JK, Fiorillo CD (2017) Theory of optimal balance predicts and explains the

amplitude and decay time of synaptic inhibition. Nat Commun 8:1–13.

Kim Y, Trussell LO (2007) Ion channels generating complex spikes in cartwheel cells of the dorsal cochlear nucleus. J Neurophysiol 97:1705–1725.

Kissinger ST, Pak A, Tang Y, Masmanidis SC, Chubykin AA (2018) Oscillatory encoding of visual stimulus familiarity. J Neurosci 38:6223–6240.

Klug a, Park TJ, Pollak GD (1995) Glycine and GABA influence binaural processing in the inferior colliculus of the mustache bat. J Neurophysiol 74:1701–1713.

Kneussel M, Brandstatter JH, Gasnier B, Feng G, Sanes JR, Betz H (2001) Gephyrin-independent clustering of postsynaptic GABAA receptor subtypes. Mol Cell Neurosci 17:973–982.

Koch C (1984) Cable theory in neurons with active, linearized membranes. Biol Cybern 50:15–33.

Koch U, Grothe B (2003) Hyperpolarization-activated current (Ih) in the inferior colliculus: distribution and contribution to temporal processing. J Neurophysiol 90:3679–3687.

Kotak VC, Korada S, Schwartz IR, Sanes DH (1998) A developmental shift from GABAergic to glycinergic transmission in the central auditory system. J Neurosci 18:4646–4655.

Kuo SP, Bradley L a, Trussell LO (2009) Heterogeneous kinetics and pharmacology of synaptic inhibition in the chick auditory brainstem. J Neurosci 29:9625–9634.

Lagier S, Carleton A, Lledo P-M (2004) Interplay between local GABAergic interneurons and relay neurons generates oscillations in the rat olfactory bulb. J Neurosci 24:4382–4392.

Lakatos P, Chen CM, O'Connell MN, Mills A, Schroeder CE (2007) Neuronal oscillations and multisensory interaction in primary auditory cortex. Neuron 53:279–292.

Lakatos P, Shah AS, Knuth KH, Ulbert I, Karmos G, Schroeder CE (2005) An oscillatory hierarchy controlling neuronal excitability and stimulus processing in the auditory cortex an oscillatory hierarchy controlling neuronal excitability and stimulus processing in the auditory cortex. J Neurophysiol 94:1904–1911.

Leao RM, Li S, Doiron B, Tzounopoulos T (2012) Diverse levels of an inwardly rectifying

potassium conductance generate heterogeneous neuronal behavior in a population of dorsal cochlear nucleus pyramidal neurons. J Neurophysiol 107:3008–3019.

LeBeau FE, Malmierca MS, Rees a (2001) Iontophoresis in vivo demonstrates a key role for GABA(A) and glycinergic inhibition in shaping frequency response areas in the inferior colliculus of guinea pig. J Neurosci 21:7303–7312.

Lee S-H, Urbano FJ, Garcia-Rill E (2018) The critical role of intrinsic membrane oscillations. Neurosignals 26:66–76.

Lee S, Kim K, Zhou ZJ (2010) Role of ACh-GABA cotransmission in detecting image motion and motion direction. Neuron 68:1159–1172.

Lefler Y, Torben-Nielsen B, Yarom Y (2013) Oscillatory activity, phase differences, and phase resetting in the inferior olivary nucleus. Front Syst Neurosci 7:1–9.

Lega B, Dionisio S, Bingaman W, Najm I, Gonzalez-Martinez J (2015) The gamma band effect for episodic memory encoding is absent in epileptogenic hippocampi. Clin Neurophysiol 126:866–872.

Lévi S, Logan SM, Tovar KR, Craig AM (2004) Gephyrin is critical for glycine receptor clustering but not for the formation of functional GABAergic synapses in hippocampal neurons. J Neurosci 24:207–217.

Li S, Choi V, Tzounopoulos T (2013) Pathogenic plasticity of Kv7. 2/3 channel activity is essential for the induction of tinnitus. Proc Natl … 110:9980–9985.

Lim R, Alvarez FJ, Walmsley B (2000) GABA mediates presynaptic inhibition at glycinergic synapses in a rat auditory brainstem nucleus. J Physiol 525.2:447–459.

Lin F, Conti F, Moran O (1991) Competitive blockage of the sodium channel by intracellular magnesium ions in central mammalian neurones. Eur Biophys J 19: 109-118.

Liu H-H, Huang C-F, Wang X (2014) Acoustic signal characteristic detection by neurons in ventral nucleus of the lateral lemniscus in mice. Zool Res 35:500–509.

Llinás R, Yarom Y (1981) Electrophysiology of mammalian inferior olivary neurones in vitro. Different types of voltage-dependent ionic conductances. J Physiol 315:549–567.

Llinás R, Yarom Y (1986) Oscillatory properties of guinea-pig inferior olivary neurones and their pharmacological modulation: an in vitro study. J Physiol 376:163–182.

Loftus WC, Bishop DC, Oliver DL (2010a) Differential Patterns of Inputs Create Functional Zones in Central Nucleus of Inferior Colliculus. J Neurosci 30:13396–13408.

Loftus WC, Bishop DC, Oliver DL (2010b) Differential patterns of inputs create functional zones in central nucleus of inferior colliculus. J Neurosci 30:13396–13408.

Lu H-W, Trussell LO (2016) Spontaneous Activity Defines Effective Convergence Ratios in an Inhibitory Circuit. J Neurosci 36:3268–3280.

Lu T, Rubio ME, Trussell LO (2008) Glycinergic transmission shaped by the corelease of GABA in a mammalian auditory synapse. Neuron 57:524–535.

Ludwig A, Zong X, Jeglitsch M, Hofmann F, Biel M (1998) A family of hyperpolarization-activated mammalian cation channels. Nature 393:587–591.

Ma CL, Kelly JB, Wu SH (2002a) AMPA and NMDA receptors mediate synaptic excitation in the rat's inferior colliculus. Hear Res 168:25–34.

Ma CL, Kelly JB, Wu SHÃ (2002b) Presynaptic modulation of GABAergic inhibition by GABAB receptors in the rat's inferior colliculus. Science (80-) 114:207–215.

Ma W-LD, Brenowitz SD (2012) Single-neuron recordings from unanesthetized mouse dorsal cochlear nucleus. J Neurophysiol 107:824–835.

Malmierca MS, Merchán MA, Henkel CK, Oliver DL (2002) Direct projections from cochlear nuclear complex to auditory thalamus in the rat. J Neurosci 22:10891–10897.

Manis PB, Molitor SC, Wu H (2003) Subthreshold oscillations generated by TTX-sensitive sodium currents in dorsal cochlear nucleus pyramidal cells. Exp Brain Res 153:443–451.

Mathalon DH, Sohal VS (2015) Neural oscillations and synchrony in brain dysfunction and neuropsychiatric disorders it's about time. JAMA Psychiatry 72:840–844.

Matsumoto-Makidono Y, Nakayama H, Yamasaki M, Miyazaki T, Kobayashi K, Watanabe M, Kano M, Sakimura K, Hashimoto K (2016) Ionic basis for membrane potential resonance in neurons of the inferior olive. Cell Rep 16:994–1004.

May BJ (2000) Role of the dorsal cochlear nucleus in the sound localization behavior of cats. Hear Res 148:74–87.

Mayer ML, Westbrook GL (1985) The action of N-methyl-d-aspartic acid on mouse spinal neurones in culture. J Physiol 361:65–90.

Mccormick DA, Pape H (1990) Properties of a hyperpolarization-activated cation current and its role in rhythmic oscillation in thalamic relay neurones. J Physiol 431:291–318.

McLaughlin SG, Szabo G, Eisenman G (1971) Divalent ions and the surface potential of charged phospholipid membranes. J Gen Physiol 58:667–687.

Melloni L, Molina C, Pena M, Torres D, Singer W, Rodriguez E (2007) Synchronization of neural activity across cortical areas correlates with conscious perception. J Neurosci 27:2858–2865.

Milbrandt JC, Hunter C, Caspary DM (1997) Alterations of GABA A receptor subunit mRNA levels in the aging Fischer 344 rat inferior colliculus. J Comp Neurol 379:455–465.

Muller E, Le Corronc H, Triller A, Legendre P (2006) Developmental dissociation of presynaptic inhibitory neurotransmitter and postsynaptic receptor clustering in the hypoglossal nucleus. Mol Cell Neurosci 32:254–273.

Muniak MA, Rivas A, Montey KL, May BJ, Francis HW, Ryugo DK (2013) 3D model of frequency representation in the cochlear nucleus of the CBA/J mouse. J Comp Neurol 521:1510–1532.

Nabekura J, Katsurabayashi S, Kakazu Y, Shibata S, Matsubara A, Jinno S, Mizoguchi Y, Sasaki A, Ishibashi H (2004) Developmental switch from GABA to glycine release in single central synaptic terminals. Nat Neurosci 7:17–23.

Nayagam DAX, Clarey JC, Paolini AG (2005) Powerful, onset inhibition in the ventral nucleus of the lateral lemniscus. J Neurophysiol 94:1651–1654.

Nerlich J, Kuenzel T, Keine C, Korenic A, Rübsamen R, Milenkovic I (2014) Dynamic fidelity control to the central auditory system: synergistic glycine/GABAergic inhibition in the cochlear nucleus. J Neurosci 34:11604–11620.

Neske GT (2016) The slow oscillation in cortical and thalamic networks: mechanisms and functions. Front Neural Circuits 9:1–25.

Oertel D, Wickesberg RE (2002) Ascending pathways through ventral nuclei of the lateral lemniscus and their possible role in pattern recognition in natural sounds.

In: Integrative Functions in the Mammalian Auditory Pathway (Oertel D, Fay RR, Popper AN, eds), pp 207-237. New York: Springer.

Oertel D, Young ED (2004) What's a cerebellar circuit doing in the auditory system? Trends Neurosci 27:104–110.

O'Keefe,J., Nadel, L., 1978. The Hippocampus as a Cognitive Map. Oxford University Press, Oxford.

Okun M, Naim A, Lampl I (2010) The Subthreshold Relation between Cortical Local Field Potential and Neuronal Firing Unveiled by Intracellular Recordings in Awake Rats. 30:4440–4448.

Oliver DL (2005) Neuronal organization in the inferior colliculus. In: The Inferior Colliculus (Winer JA, Schreiner CE, eds), pp 69-114. New York: Springer.

Olsen T, Capurro A, Pilati N, Large CH, Hamann M (2018) Kv3 K+ currents contribute to spike-timing in dorsal cochlear nucleus principal cells. Neuropharmacology 133:319–333.

Ostapoff EM, Benson CG, Saint Marie RL (1997) GABA- and glycine-immunoreactive projections from the superior olivary complex to the cochlear nucleus in guinea pig. J Comp Neurol 381:500–512.

Padmanabhan K, Urban NN (2010) Intrinsic biophysical diversity decorrelates neuronal firing while increasing information content. Nat Neurosci 13:1276–1282.

Peruzzi D, Sivaramakrishnan S, Oliver D. (2000) Identification of cell types in brain slices of the inferior colliculus. Neuroscience 101:403–416.

Pollak GD, Xie R, Gittelman JX, Andoni S, Li N (2011) The dominance of inhibition in the inferior colliculus. Hear Res 274:27–39.

Portfors C V., Wenstrup JJ (2001) Responses to combinations of tones in the nuclei of the lateral lemniscus. JARO 02:104–117.

Poulet JFA, Petersen CCH (2008) Internal brain state regulates membrane potential synchrony in barrel cortex of behaving mice. Nature 454:881–885.

Prescott SA, Ratté S, De Koninck Y, Sejnowski TJ (2008a) Pyramidal neurons switch from integrators in vitro to resonators under in vivo-like conditions. J Neurophysiol 100:3030–3042.

Prescott SA, Ratté S, Koninck Y De, Sejnowski TJ (2008b) Pyramidal Neurons Switch

from Integrators In Vitro to Resonators Under In Vivo-Like Conditions. J Neurophysiol 100:3030–3042.

Puil E, Gimbarzevsky B, Miura RM (1986) Quantification of membrane properties of trigeminal root ganglion neurons in guinea pigs. J Neurophysiol 55:995–1016.

Pusch M (1990) Open-channel block of Na^+ channels by intracellular Mg^{2+}. Eur Biophys J 18: 317-326.

Recio-Spinoso A, Joris PX (2014) Temporal properties of responses to sound in the ventral nucleus of the lateral lemniscus. J Neurophysiol 111:817–835.

Reetz G, Ehret G (1999) Inputs from three brainstem sources to identified neurons of the mouse inferior colliculus slice. Brain Res 816:527–543.

Represa A, Ben-ari Y (2005) Trophic actions of GABA on neuronal development. Trends Neurosci 28:278–283.

Rhode WS, Greenberg S (1994) Encoding of amplitude modulation in the cochlear nucleus of the cat. J Neurophysiol 71:1797–1825.

Riquelme R, Saldaña E, Osen KK, Ottersen OP, Merchán MA (2001) Colocalization of GABA and glycine in the ventral nucleus of the lateral lemniscus in rat: An in situ hybridization and semiquantitative immunocytochemical study. J Comp Neurol 432:409–424.

Roberts MT, Bender KJ, Trussell LO (2008) Fidelity of complex spike-mediated synaptic transmission between inhibitory interneurons. J Neurosci 28:9440–9450.

Robertson D, Mulders W (2012) The inferior colliculus: involvement in hyperactivity and tinnitus. In: Tinnitus (Eggermont JJ, Zeng FG, Popper AN, Fay RR, eds), pp 121-135. New York: Springer.

Robertson D, Mulders W (2012) Tinnitus. 44:121–135.

Ropp TJF, Tiedemann KL, Young ED, May BJ (2014) Effects of unilateral acoustic trauma on tinnitus-related spontaneous activity in the inferior colliculus. JARO 15:1007–1022.

Rubio ME (2004) Differential distribution of synaptic endings containing glutamate, glycine, and GABA in the rat dorsal cochlear nucleus. J Comp Neurol 477:253–272.

Russier M, Kopysova IL, Ankri N, Ferrand N, Debanne D (2002) GABA and glycine co-release optimizes functional inhibition in rat brainstem motoneurons in vitro. J

Physiol 541:123–137.

Saint Marie RL, Baker RA (1990) Neurotransmitter-specific uptake and retrograde transport of [3H]glycine from the inferior colliculus by ipsilateral projections of the superior olivary complex and nuclei of the lateral lemniscus. Brain Res 524:244–253.

Saint Marie RL, Ostapoff EM, Morest DK, Wenthold RJ (1989a) Glycine-immunoreactive projection of the cat lateral superior olive: possible role in midbrain ear dominance. J Comp Neurol 279:382–396.

Saint Marie RL, Ostapoff EM, Morest DK, Wenthold RJ (1989b) Glycine-immunoreactive projection of the cat lateral superior olive: possible role in midbrain ear dominance. J Comp Neurol 279:382–396.

Saint Marie RL, Shneiderman a, Stanforth D a (1997a) Patterns of gamma-aminobutyric acid and glycine immunoreactivities reflect structural and functional differences of the cat lateral lemniscal nuclei. J Comp Neurol 389:264–276.

Saint Marie RL, Stanforth DA, Jubelier EM (1997b) Substrate for rapid feedforward inhibition of the auditory forebrain. Brain Res 765:173–176.

Sanchez-Vives M V., McCormick DA (2000) Cellular and network mechanisms of rhythmic recurrent activity in neocortex. Nat Neurosci 3:1027–1034.

Sanchez JT, Gans D, Wenstrup JJ (2007) Contribution of NMDA and AMPA Receptors to Temporal Patterning of Auditory Responses in the Inferior Colliculus. 27:1954–1963.

Saraga F, Ng L, Skinner FK (2006) Distal gap junctions and active dendrites can tune network dynamics. J Neurophysiol 95:1669–1682.

Schofield BR, Cant NB (1997) Ventral nucleus of the lateral lemniscus in guinea pigs: Cytoarchitecture and inputs from the cochlear nucleus. J Comp Neurol 379:363–385.

Schoppa NE, Westbrook GL (2001) Glomerulus-specific synchronization of mitral cells in the olfactory bulb. Neuron 31:639–651.

Schwindt PC, Crill WE (1995) Amplification of synaptic current by persistent sodium conductance in apical dendrite of neocortical neurons. J Neurophysiol 74:2220–2224.

Shamir M, Sompolinsky H (2006) Implications of neuronal diversity on population coding. Neural Comput 18:1951–1986.

Shore SE (2005) Multisensory integration in the dorsal cochlear nucleus: unit responses to acoustic and trigeminal ganglion stimulation. Eur J Neurosci 21:3334–3348.

Shuman T, Amendolara B, Golshani P (2017) Theta rhythmopathy in TLE cognitive disability. Epilepsy Curr 2:107–111.

Singer JH, Berger a J (1999) Contribution of single-channel properties to the time course and amplitude variance of quantal glycine currents recorded in rat motoneurons. J Neurophysiol 81:1608–1616.

Singla S, Dempsey C, Warren R, Enikolopov AG, Sawtell NB (2017) A cerebellum-like circuit in the auditory system cancels responses to self-generated sounds. Nat Neurosci 20:943–950.

Sivaramakrishnan S, Oliver DL (2001) Distinct K currents result in physiologically distinct cell types in the inferior colliculus of the rat. J Neurosci 21:2861–2877.

Somjen GG (2004) Ions in the Brain: Normal Function, Seizures and Stroke. Oxford: Oxford UP.

Stagkourakis S, Pérez CT, Hellysaz A, Ammari R, Broberger C (2018) Network oscillation rules imposed by species-specific electrical coupling. Elife 7:e33144.

Stefanescu RA, Shore SE (2015) NMDA receptors mediate stimulus-timing-dependent plasticity and neural synchrony in the dorsal cochlear nucleus. Front Neural Circuits 9:1–14.

Stefanescu RA, Shore SE (2017) Muscarinic acetylcholine receptors control baseline activity and hebbian stimulus timing-dependent plasticity in fusiform cells of the dorsal cochlear nucleus. J Neurophysiol 117:1229–1238.

Stensrud MJ, Puchades M, Gundersen V (2014) GABA is localized in dopaminergic synaptic vesicles in the rodent striatum. Brain Struct Funct 6: 1901-12.

Steriade M, Contreras D, Curró Dossi R, Nuñez A (1993) The slow (< 1 Hz) oscillation in reticular thalamic and thalamocortical neurons: scenario of sleep rhythm generation in interacting thalamic and neocortical networks. J Neurosci 13:3284–3299.

Stiebler I, Ehret G (1985) Inferior colliculus of the house mouse. I. A quantitative study

of tonotopic organization, frequency representation, and tone-threshold distribution. J Comp Neurol 238:65–76.

Sun H, Ma CL, Kelly JB, Wu SH (2006) GABAB receptor-mediated presynaptic inhibition of glutamatergic transmission in the inferior colliculus. Neurosci Lett 399:151–156.

Sun H, Wu SH (2009) The physiological role of pre- and postsynaptic GABAB receptors in membrane excitability and synaptic transmission of neurons in the rat's dorsal cortex of the inferior colliculus. Neuroscience 160:198–211.

Suneja SK, Potashner SJ, Benson CG (1998) Plastic changes in glycine and GABA release and uptake in adult brain stem auditory nuclei after unilateral middle ear ossicle removal and cochlear ablation. Exp Neurol 151:273–288.

Takazawa T, Choudhury P, Tong C-K, Conway CM, Scherrer G, Flood PD, Mukai J, MacDermott AB (2017) Inhibition mediated by glycinergic and GABAergic receptors on excitatory neurons in mouse superficial dorsal horn Is location-specific but modified by inflammation. J Neurosci 37:2336–2348.

Tanaka I, Ezure K (2004) Overall distribution of GLYT2 mRNA-containing versus GAD67 mRNA-containing neurons and colocalization of both mRNAs in midbrain, pons, and cerebellum in rats. Neurosci Res 49:165–178.

Tang Z-Q, Trussell LO (2015) Serotonergic regulation of excitability of principal cells of the Dorsal cochlear nucleus. J Neurosci 35:4540–4551.

ten Oever S, Schroeder CE, Poeppel D, van Atteveldt N, Mehta AD, Mégevand P, Groppe DM, Zion-Golumbic E (2017) Low-frequency cortical oscillations entrain to subthreshold rhythmic auditory stimuli. J Neurosci 37:4903–4912.

Trenholm S, McLaughlin AJ, Schwab DJ, Turner MH, Smith RG, Rieke F, Awatramani GB (2014) Nonlinear dendritic integration of electrical and chemical synaptic inputs drives fine-scale correlations. Nat Neurosci 17:1759–1766.

Tritsch NX, Granger AJ, Sabatini BL (2016) Mechanisms and functions of GABA co-release. Nat Rev Neurosci 17:139–145.

Trombley PQ, Blakemore LJ, Hill BJ (2011) Zinc modulation of glycine receptors. Neuroscience 186:32–38.

Turecek R, Trussell LO (2001) Presynaptic glycine receptors enhance transmitter

release at a mammalian central synapse. Nature 411:587–590.
Tyagarajan SK, Fritschy J-M (2014) Gephyrin: a master regulator of neuronal function? Nat Rev Neurosci 15:141–156.
Tzounopoulos T, Kim Y, Oertel D, Trussell LO (2004) Cell-specific, spike timing-dependent plasticities in the dorsal cochlear nucleus. Nat Neurosci 7:719–725.
Vaaga CE, Borisovska M, Westbrook GL (2014) Dual-transmitter neurons: Functional implications of co-release and co-transmission. Curr Opin Neurobiol 29:25–32.
Vater M, Habbicht H, Kössl M, Grothe B (1992) The functional role of GABA and glycine in monaural and binaural processing in the inferior colliculus of horseshoe bats. J Comp Physiol A 171:541–553.
Vaughn MD, Pozza MF, Lingenhöhl K (1997) Excitatory acoustic responses in the inferior colliculus of the rat are increased by GABAB receptor blockade. Neuropharmacology 35:1761–1767.
Voigt HF, Young ED (1988) Neural correlations in the dorsal cochlear nucleus: pairs of units with similar response properties. J Neurophysiol 59:1014–1032.
Wallace MN, Shackleton TM, Palmer AR (2012) Morphological and physiological characteristics of laminar cells in the central nucleus of the inferior colliculus. Front Neural Circuits 6:55.
Wang X-J (2010) Neurophysiological and computational principles of cortical rhythms in cognition. Physiol Rev 90:1195–1268.
Wässle H, Heinze L, Ivanova E, Majumdar S, Weiss J, Harvey RJ, Haverkamp S (2009) Glycinergic transmission in the mammalian retina. Front Mol Neurosci 2:1–12.
Watanabe T, Simada Z (1973) Pharmacological properties of cat's collicular auditory neurons. Jap J Physiol 23:291–308.
Wenstrup JJ, Nataraj K, Sanchez JT (2012) Mechanisms of spectral and temporal integration in the mustached bat inferior colliculus. Front Neural Circuits 6:1–21.
Whittington MA, Traub RD (2003) Interneuron diversity series: Inhibitory interneurons and network oscillations in vitro. Trends Neurosci 26:676–682.
Wilson CJ (2005) The mechanism of intrinsic amplification of hyperpolarizations and spontaneous bursting in striatal cholinergic interneurons. Neuron 45:575–585.
Winer JA, Larue DT, Diehl JJ, Hefti BJ (1998) Auditory cortical projections to the cat

inferior colliculus. J Comp Neurol 400:147–74.

Wojcik SM, Katsurabayashi S, Guillemin I, Friauf E, Rosenmund C, Brose N, Rhee JS (2006) A shared vesicular carrier allows synaptic corelease of GABA and glycine. Neuron 50:575–587.

Wu C, Martel DT, Shore SE (2016) Increased synchrony and bursting of dorsal cochlear nucleus fusiform cells correlate with tinnitus. J Neurosci 36:2068–2073.

Xie R, Gittelman JX, Pollak GD (2007) Rethinking tuning: in vivo whole-cell recordings of the inferior colliculus in awake bats. J Neurosci 27:9469–9481.

Xie R, Manis PB (2013) Target-specific IPSC kinetics promote temporal processing in auditory parallel pathways. J Neurosci 33:1598–1614.

Xie R, Meitzen J, Pollak GD (2005) Differing roles of inhibition in hierarchical processing of species-specific calls in auditory brainstem nuclei. J Neurophysiol 94:4019–4037.

Xiong B, Manohar S, Chen G, Yu N, Zhao X, Salvi R, Sun W (2017) Hyperexcitability of inferior colliculus and acoustic startle reflex with age-related hearing loss. Hear Res 350:32–42.

Xiong W, Chen S-R, He L, Cheng K, Zhao Y-L, Chen H, Li D-P, Homanics GE, Peever J, Rice KC, Wu L-G, Pan H-L, Zhang L (2014) Presynaptic glycine receptors as a potential therapeutic target for hyperekplexia disease. Nat Neurosci 17:232–239

Xiong W, Cheng K, Cui T, Godlewski G, Rice KC, Xu Y, Zhang L (2011) Cannabinoid potentiation of glycine receptors contributes to cannabis-induced analgesia. Nat Chem Biol 7:296–303.

Xiong W, Cui T, Cheng K, Yang F, Chen S-R, Willenbring D, Guan Y, Pan H-L, Ren K, Xu Y, Zhang L (2012) Cannabinoids suppress inflammatory and neuropathic pain by targeting alpha3 glycine receptors. J Exp Med 209:1121–1134.

Xiong XR, Liang F, Zingg B, Ji X, Ibrahim LA, Tao HW, Zhang LI (2015) Auditory cortex controls sound-driven innate defense behaviour through corticofugal projections to inferior colliculus. Nat Commun 6:7224.

Yaeger DB, Trussell LO (2016) Auditory Golgi cells are interconnected predominantly by electrical synapses. J Neurophysiol 116:540–551.

Yan L, Suneja SK, Potashner SJ (2007) Protein kinases regulate glycine receptor

binding in brain stem auditory nuclei after unilateral cochlear ablation. Brain Res 5:102–106.

Yu J, Ferster D (2010) Membrane potential synchrony in primary visual cortex during sensory stimulation. Neuron 68:1187–1201.

Zeilhofer HU, Studler B, Arabadzisz D, Schweizer C, Ahmadi S, Layh B, Bösl MR, Fritschy JM (2005) Glycinergic neurons expressing enhanced green fluorescent protein in bacterial artificial chromosome transgenic mice. J Comp Neurol 482:123–141.

Zhang DX, Li L, Kelly JB, Wu SH (1998) GABAergic projections from the lateral lemniscus to the inferior colliculus of the rat. Hear Res 117:1–12.

Zhang H, Kelly JB (2006) Responses of neurons in the rat's ventral nucleus of the lateral lemniscus to monaural and binaural tone bursts responses of neurons in the rat's ventral nucleus of the lateral lemniscus to monaural and binaural tone bursts. J Neurophysiol 95:2501–2512.

Zhang L, Chen L, Xue Y, Yung W (2008) Modulation of synaptic GABA A receptor function by zolpidem in substantia nigra pars reticulata. Acta Pharmacol Sin 29:161–168.

Zhang Y, Wu SH (2000) Long-term potentiation in the inferior colliculus studied in rat brain slice. Hear Res 147:92–103.

Zhou L, Chillag KL, Nigro MA (2002) Hyperekplexia: A treatable neurogenetic disease. Brain Dev 24:669–674.

Zijlmans M, Jacobs J, Zelmann R, Dubeau F, Gotman J (2009) High-frequency oscillations mirror disease activity in patients with epilepsy. Neurology 72:979–986.